SINGLE-SHOT MEASUREMENTS OF COMPLEX PULSES USING FREQUENCY-RESOLVED OPTICAL GATING

A Thesis
Presented to
The Academic Faculty

by

Tsz Chun Wong

In Partial Fulfillment
of the Requirements for the Degree
Doctor of Philosophy in the
School of Physics

Georgia Institute of Technology
December 2013

SINGLE-SHOT MEASUREMENTS OF COMPLEX PULSES USING FREQUENCY-RESOLVED OPTICAL GATING

Approved by:

Professor Rick Trebino, Advisor
School of Physics
Georgia Institute of Technology

Professor Jennifer Curtis
School of Physics
Georgia Institute of Technology

Professor Zhigang Jiang
School of Physics
Georgia Institute of Technology

Professor Ali Adibi
School of Electrical and Computer Engineering
Georgia Institute of Technology

Professor John Buck
School of Electrical and Computer Engineering
Georgia Institute of Technology

Date Approved: 1 November 2013

To my mother, Yuk Ping Cheung, and father, Hung Wah Wong

ACKNOWLEDGEMENTS

I would like to thank my advisor, Rick Trebino, for giving me this exciting and challenging project. I am thankful for his encouragement, advice and great insight on how to be an experimental physicist. It was a great pleasure to work with other members in our group including Pamela Bowlan, Dongjoo Lee, Jacob Cohen, Vikrant Chauhan, Peter Vaughan, Patrick Gartland, Justin Ratner, and Michelle Rhodes. Thank you for the experimental tips, insightful discussions, guidances and helps over time. I am especially thankful to Pamela, Jacob, Vikrant and Peter for guiding me through the detail of different experimental setups when I was new to the lab. I am also thankful to Dongjoo, Justin, and Michelle for the extended discussions of experimental related problems and editing my writings. I am also grateful to Linda Trebino and everyone in the School of Physics for helping me to resolve administrative issues.

I would like to thank my friends and families from Hong Kong for encouraging me to purchase my Ph.D. in Georgia Tech. I also want to express my thanks to all the friends and people I have met during my study here. Your company make my graduate student life much more enjoyable. Last, but not lease, I would like to thank my parents and brother for their endless love and support.

TABLE OF CONTENTS

LIST OF FIGURES

SUMMARY

Frequency-resolved optical gating (FROG) is the standard for measuring femtosecond laser pulses. It measures relatively simple pulses on a single-shot and complex pulses using multi-shot scanning and averaging. However, experience from intensity autocorrelation suggests that multi-shot measurements may suffer from a coherent artifact caused by instability in the laser source. This motivates the development of single-shot techniques to measure complex pulses that are traditionally measured on multi-shot.

In this thesis, the coherent artifacts present in modern pulse measurement techniques are examined and single-shot techniques for measuring complex pulse(s) are proposed and demonstrated. The study of the coherent artifact in this work shows that modern pulse measurement techniques also suffer from coherent artifacts and therefore single-shot measurements should be performed when possible. Here, two single-shot experimental setups are developed for different scenarios. First, an extension of FROG is developed to measure two unknown pulses simultaneously on a single-shot. This setup can measure pulses that have very different center wavelengths, spectral bandwidths, and complexities. Second, pulse-front tilt is incorporated to extend the temporal range of single-shot FROG to tens of picoseconds which traditionally can only be attained by multi-shot scanning. Finally, the pulse-front tilt setup is modified to perform a single-shot measurement of supercontinuum generated

from fibers, one of the most difficult pulses to measure due to its long temporal range, broad spectral bandwidth, and low pulse energy.

CHAPTER I

INTRODUCTION

Ultrashort (or ultrafast) laser pulses are short bursts of light range from a few femtoseconds (1 fs = 10^{-15} s) to tens of picoseconds (1 ps = 10^{-12} s). Ultrashort laser pulses, due to their short duration in the temporal domain, have a large bandwidth in the spectral domain. This can be seen easily from the Fourier transform relation between the time and frequency. The short duration in time gives these ultrashort laser pulses a very high peak intensity for a relatively low average powers.

The short temporal duration, large spectral bandwidth and high peak intensity make ultrashort laser pulse the ideal light source for various applications. The ultrashort temporal duration enables researchers to perform ultrafast experiments to observe electron dynamics inside chemical reactions as it happens, also known as the ultrafast chemistry. Common techniques for these experiments such as ultrafast pump-probe and time-resolved photoelectron imaging [1–3]. The resolution of these experiments depends heavily on how short the pulses are, and, more importantly, how accurate the pulse duration could be characterized. Micromachining is another application of ultrashort pulses. Material could be ablated using ultrashort pulses with minimal amount of pulse energy dissipated as heat. It is shown that shorter pulses give better surface finish which makes high precision surface micromaching possible [4, 5]. Three-dimensional microfabrication can be achieved in transparent materials by altering the refractive index [6]. The high peak intensity allows the use of ultrashort pulses in multi-photon microscopy to drastically increase the resolution of the microscopy compared with normal fluorescence microscopy [7–9]. Multi-photon microscopy detects second, third or higher harmonic signal generated inside the target tissue from the pulses centered at a longer wavelength which resides below the absorption energy to avoid fluorescence and to achieve better signal-to-noise ratio. The harmonic generation happens only near the focus of the pulse because a high peak intensity is needed for nonlinear optical process to occur. Other innovations such as laser in situ keratomileusis (LASIK) [10], supercontinuum generation [11–16], and attosecond-pulse generations [17, 18] all rely on ultrashort pulses as well. The generation of ultrashort laser pulse is not only an important science itself, but is also an excellent tool for other fields of science and engineering. However, it is difficult to advance ultrashort pulses related sciences and technologies without a complete characterization of them. Therefore, the study and development of pulse measurement techniques are very important.

1.1 Ultrashort laser pulses generation

Laser sources can be classified into two main categories by their operation mode: continuous wave laser (CW) and pulsed laser (generally less than ns in duration). There are different choices for the laser gain media, such gas (CO_2, HeNe and Argon), dye (Rhodamine 6G and Coumarin 102), solid (Ruby, Nd:YAG and Ti:sapphire) and semiconductor (GaN and InGaAs). Typically, CW lasers have a narrow spectrum compared with pulsed lasers. Nanosecond (ns) laser pulses can be achieved by adding a fast shutter to CW laser system which opens and closes in a short period of time that alter the losses of the system to generate short laser pulses. One such fast shutters is the Pockels cell, which acts as a quarter-wave plate when an appropriate voltage is applied across it to control the polarization of the light inside the laser cavity. This method is known as Q-switching. As an active device is switching on-and-off to generate the short pulses, the pulse duration depends on the switching time of applied voltage. The shortest pulses from active Q-switching lasers are usually 10-100 ns [19, 20].

In order to generate shorter laser pulses, a saturable absorber is used inside the laser cavity for passive Q-switching. The saturable absorber is a material that is transparent to high intensity incident light but becomes absorbing when incident intensity falls below a threshold. So, if a pulse with Gaussian shape temporal profile propagates inside the laser cavity, the saturable absorber will absorb its leading and trailing edge where its intensity is lower and let the high intensity center region of the pulse pass without being absorbed [21]. In modern femtosecond pulses generation technology, ultrashort pulses as short as 5 fs can be generated using Ti:sapphire as the gain medium [22]. The fs pulse generation is achieved by Kerr-lensing mode-locking [23]. Kerr-lensing, also known as self-focusing, is a nonlinear optical effect that happens when intense light spatially modulates the nonlinear media's refractive index causing the light to focus. The strength of Kerr-lensing depends on the intensity of the light; therefore, the shorter the pulse, the more self-focusing it experiences. The cavity is designed and aligned to selectively collimate only the self-focused light but not the other portion. The non-collimated part of the pulse diverges in the cavity quickly leaves the collimated part amplified and become shorter and more intense. Another key component of a Ti:sapphire laser is dispersion compensation. The laser pulse experiences positive group delay dispersion (GDD) after passing through the Ti:sapphire crystal. This can be compensated by prism-pair compressor or chirp mirrors inside the cavity. A typical Ti:sapphire laser produces pulses with duration ranged from 20 fs to 200 fs and has a repetition rate of ~100 MHz with pulse energy of 1 nJ to 10 nJ. It is common to amplify the low energy pulses by a regenerative amplifier to achieve an energy level of a few mJ at repetition rate of kHz. In this work, amplified pulses with energy of ~2.1 mJ from a regenerative amplifier with repetition rate of 1 kHz (Legend Elite, Coherent) are used.

1.2 Ultrashort laser pulses measurement

Ultrashort pulses have short temporal duration and large bandwidth which make them difficult to measure. In general, a shorter event is used to measure a longer event, but the shortest event for ultrashort pulses is the pulse itself. That means there is only one option: use the ultrashort pulse to measure itself. In the past, researchers relied on spectral measurements of the laser source which works well for CW and ns-pulse lasers, because they have very narrow spectral bandwidths. Therefore, measuring only the spectrum is usually enough to know it well, because GDD and other high-order phase effects will not be prominent to a very narrow-band light source. In contrast, ultrashort laser pulses have much more bandwidth, in which measuring only the spectrum is not very helpful as the phase information plays an important role to temporal profile of the pulse. For example, in Figure 1.1, three pulses with

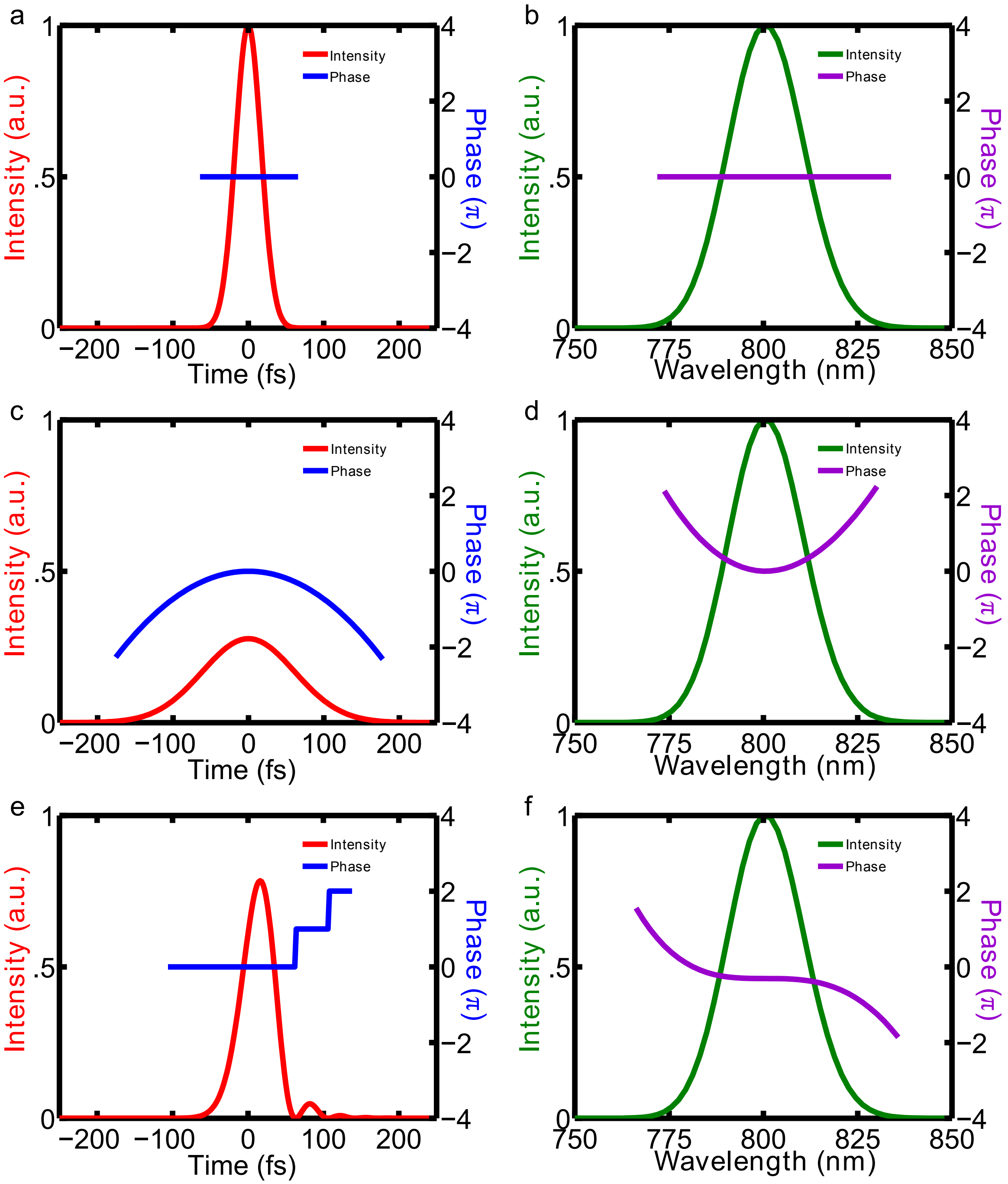

Figure 1.1: Example of pulses with the same spectra but different spectral phases. All three pulses have the same spectrum. Top row: Flat-spectral-phase with Gaussian spectrum leads to shortest temporal duration supported by its bandwidth. Middle row: Quadratic spectral phase leads to significant temporal broadening. Bottom row: Third-order spectral phase leads to satellite pulses following the main pulse with slight temporal broadening.

the same spectrum but with different spectral phase are shown. The top row, (a) and (b), shows the intensity and phase of a flat-phase Gaussian in temporal and spectral domain respectively. The specification is taken from a typical Ti:sapphire laser with center wavelength of the spectrum is located at 800 nm with full-width half maximum (FWHM) of ∼24 nm. A flat-phase Gaussian corresponds to the temporally shortest pulse supported by its spectral bandwidth. The flat-phase Gaussian pulse has a temporal FWHM of 40 fs. When a flat-phase Gaussian pulse passes through a dispersive medium, such as glass, a quadratic phase will be introduced to spectral phase. A quadratic phase is equivalent to GDD which means different spectral components do not travel at the same speed making the pulse spreads in time. This is shown in the middle row, (c) and (d), which a quadratic spectral phase leads to a significant pulse broadening. The temporal FHWM is ∼144 fs, much longer than 40 fs. As the temporal duration increases, the peak intensity falls as indicated in Figure 1.1c. The bottom row, (e) and (f), shows the profile with third-order phase in the spectral domain. It creates satellite pulses following the main pulse in the temporal domain, this is the result of beating between different wavelength components of the pulse. The temporal FWHM is ∼50 fs, slightly longer than the flat-phase case. From Figure 1.1, we can see how the spectral phase of the pulse changes its temporal profile. Since dispersion is inevitable in any optical system, extreme care should be use when working with ultrashort pulses, especially fs-long pulses. Thus, it is important to measure not only the intensity, but also the phase of ultrashort pulses.

1.2.1 Autocorrelation

Intensity autocorrelation (AC) was one of the most commonly used methods from the 1970's to 1990's to estimate the temporal intensity profile of ultrashort pulses [24–26]. The AC measurement relies on second harmonic generation (SHG) and the assumption of the pulse's temporal profile, usually a Gaussian or a squared hyperbolic secant (sech^2). SHG is a nonlinear optical process that happens when two short pulses overlap inside a SHG medium both spatially and temporally. As the pulses are short in time, delaying the arrival time of one of the pulses with respect to another one controls the intensity of the output SHG signal. The highest SHG signal is achieved when the two pulses arrive at the same time. Zero SHG signal is generated when the two pulses are temporally separated too far away from each other. Typical AC measurement steps are: 1) generate a replica of the pulse by using a beam splitter, 2) focus and overlap the pulse and its replica at a SHG medium, 3) vary the delay and measure the output SHG intensity at each time delay to generate the AC of the pulse, 4) measure the FWHM of the AC and divide by a constant (depending on the temporal profile assumption) to estimate the FWHM of the temporal intensity. However, it is shown that AC has non-trivial ambiguities, meaning that multiple pulses could generate indistinguishable AC signal [27]. An example of this ambiguity is shown in Figure 1.2. The different two pulses shown in (a) and (b) are used to generate AC. The resultant ACs shown in (c) are indistinguishable.

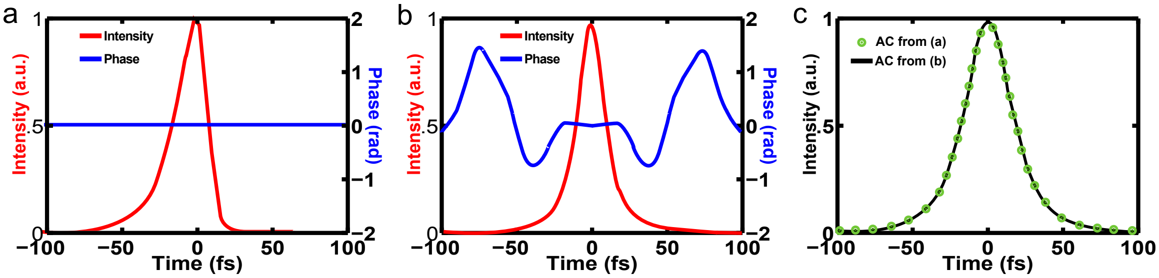

Figure 1.2: Ambiguity in intensity autocorrelation. Indistinguishable autocorrelation signals (c) generated by two different ultrashort pulses shown in (a) and (b).

1.2.2 Frequency-Resolved Optical Gating (FROG)

Frequency-resolved optical gating (FROG) is the most common and reliable technique to measure ultrashort pulses. The most commonly used FROG technique is SHG FROG is depicted in Figure 1.3. The first half of the setup is the same as the AC (generate a SHG signal by replicating the unknown pulse), but, instead of measuring the intensity of the SHG signal, the spectrum of the SHG signal at each time delay is recorded to generate a spectrogram or FROG trace. Once the FROG trace is measured, an iterative generalized-projection phase retrieval algorithm (usually denoted as the FROG retrieval algorithm) is used to determine the intensity and phase of the pulse [28]. The convergence of the retrieval is measured by the root-mean-square (rms) difference between the measured and retrieved FROG traces, or the G-error [28].

1.2.3 Polarization-gate FROG

Polarization-gate is another commonly used gating geometry for FROG. Even though a pair of high quality polarizers is required for this geometry, its unlimited phase-matching bandwidth makes it versatile in many cases. The experimental schematic

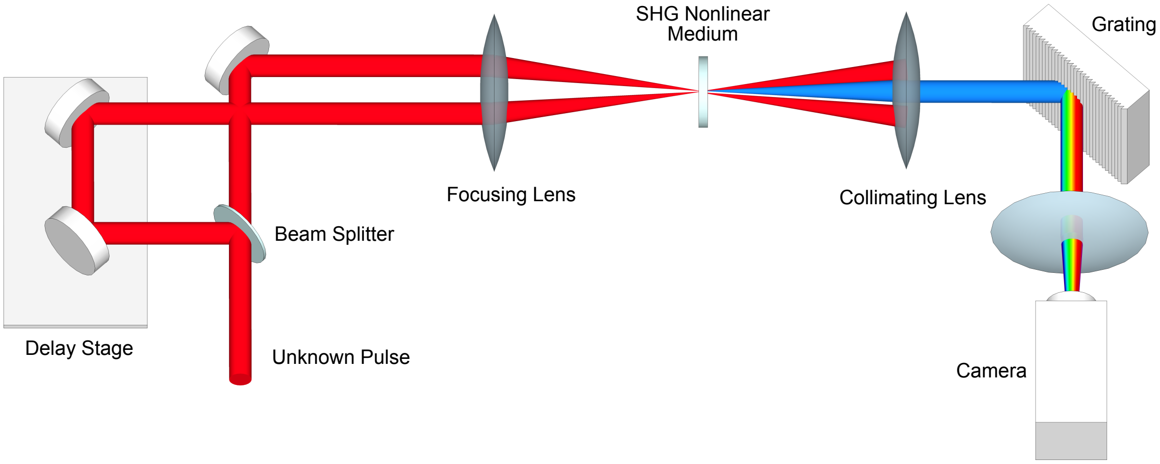

Figure 1.3: Experimental schematic of multi-shot SHG FROG. A replica of the unknown pulse (red) is generated and passes through a delay stage before focusing into the nonlinear medium for SHG. The spectrum, instead of intensity in the case of autocorrelation, of the SHG signal (blue) is measured at each time delay point. Combining the spectra of all the time delays, a FROG trace is generated.

of a PG FROG is shown in Figure 1.4. A replica is first generated by a beam splitter. One of the replicas goes through a 0° polarizer, another one through a waveplate to rotate its polarization to 45° and then a 45° polarizer to increase the polarization purity. The two replicas are then focused into a PG medium, any material with non-zero third-order nonlinear susceptibility, $\chi^{(3)}$, to generate the signal. The gating mechanism of PG FROG is optically induced polarization rotation, a well known third-order nonlinear optical effect, which happens when two pulses have polarizations 45° relative to each other interact inside a $\chi^{(3)}$ medium. The signal is then analyzed by 90° cross-polarizer where the rotated polarization of the pulse passes through and the unrotated part is rejected. The nonlinear polarization governing the interaction, P^{NL}, is proportional to the signal field,

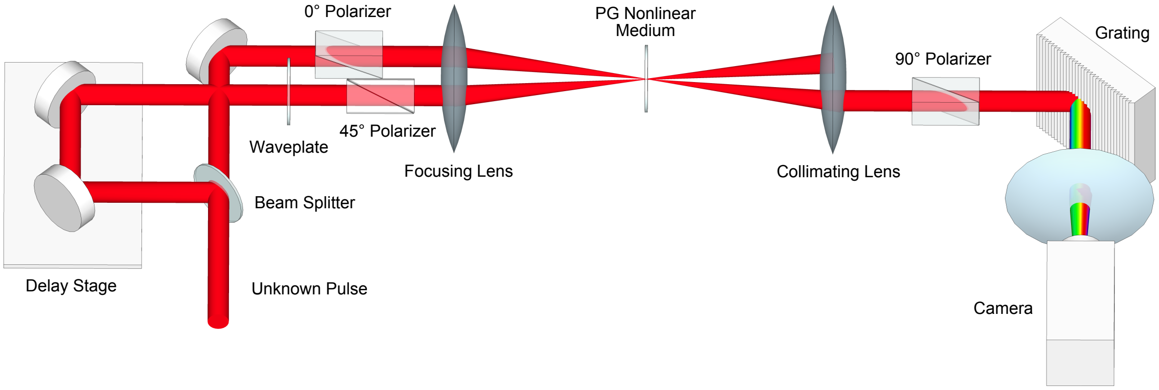

Figure 1.4: Experimental schematic of multi-shot PG FROG. A replica of the unknown pulse is split out by a beam splitter and passes through a delay stage. One of the replica goes through a 0° polarizer. Another replica first goes through a waveplate to rotate its polarization to 45° before passing the 45° to increase it polarization purity. The signal is generated inside the nonlinear medium by optically induced polarization rotation. The rotated portion of the unknown pulse is filtered by a 90° polarizer to separate it from the unrotated portion.

$$
\begin{aligned}
P^{NL} &\propto \chi^{(3)} E_{unk} E_{ref} E_{ref}^{*} && (1.1)\\
&= \chi^{(3)} E_{unk} |E_{ref}|^{2} && (1.2)
\end{aligned}
$$

where $\chi^{(3)}$ is the third-order nonlinear susceptibility of the medium, E is the electric field, subscript ref and unk represent reference and unknown pulse respectively, and * denotes the complex conjugate. The phase-mismatch of this nonlinear optical process, Δk, is

$$
\begin{aligned}
\Delta k &= k_{unk} - (k_{unk} + E_{ref} - E_{ref}) \\
&= 0 && (1.3)
\end{aligned}
$$

It is clear from equation 1.3 that the phase-mismatch is identically zero for any reference pulses. The reference pulse can be a replica of the unknown (setup of a normal

PG FROG) or a independently characterized known pulse (setup of a PG cross-correlation FROG). As the phase-mismatch is always zero, this nonlinear process has a unlimited phase-matching bandwidth. This special property makes PG geometry extremely versatile as phase-matching bandwidth is a limiting factor in other geometry such as SHG. This property also allows for an arbitrarily large crossing angle in the single shot FROG device, which is essential for measurements presented in Chapter 5. However, PG geometry has reduced sensitivity, because a third-order nonlinear optical process is typically orders of magnitude weaker than a second-order one. Detailed discussions on PG geometry are given in Chapters 3 and 4.

1.2.4 Single-shot FROG

FROG devices achieve single-shot operation by crossing two beams at an angle as shown in Figure 1.5. The top part of pulse 1 (red ellipse) arrives at the nonlinear medium (light blue rectangle) earlier than pulse 2 (orange ellipse). Conversely, the situation reverses at the bottom where pulse 1 arrives later than pulse 2. Both of the pulses arrive the center of the nonlinear medium at the same time. This maps relative time delay between the two pulses onto the transverse spatial position of the nonlinear medium. The total temporal range ΔT resulted by this geometry can be calculated by,

$$\Delta T = \frac{d}{c} \tan\theta \tag{1.4}$$

where c is the speed of light, d is the beam diameter, θ is the internal crossing angle.

The schematic of PG FROG implemented in single-shot geometry is shown in Figure 1.6. Note that the spherical lenses used in multi-shot FROG are replaced by

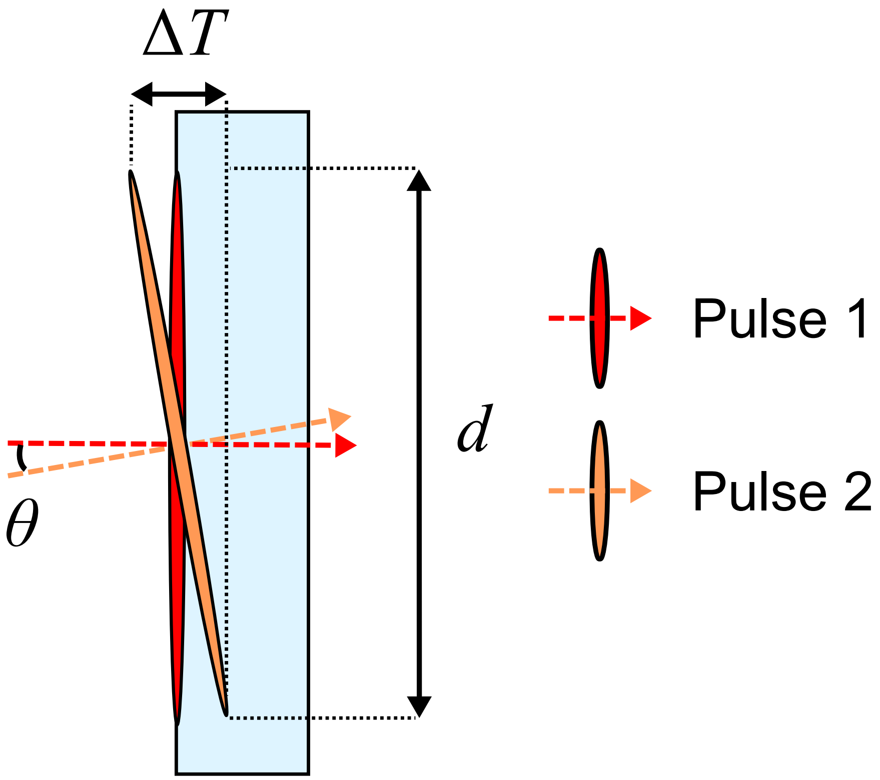

Figure 1.5: Illustration of single-shot geometry in FROG devices. Two pulses cross inside the nonlinear medium (light blue rectangle) at an angle θ to generate the required time delay for single-shot operation. Pulse 1 (red) arrives at the nonlinear medium earlier than Pulse 2 (orange) at the top part of the medium. Pulse 1 arrives at the bottom part of the medium later than Pulse 2. Both pulses arrive at the center part of the medium at the same time.

cylindrical lenses to create line foci instead of point foci. Also, the original delay stage is now used to find the zero-delay between the two pulses. Once the zero-delay point is found, the delay stage remains stationary during the measurement. A cylindrical lens is used to image the nonlinear medium onto the camera (only the dimension of the crossing beams), which maps time delay to spatial position of the camera. The other dimension of the camera is used by the grating-lens spectrometer to generate the spectrum at each delay point. Unlike multi-shot FROG which uses a scanning stage to generate the time delay in discrete steps, single-shot FROG concurrently

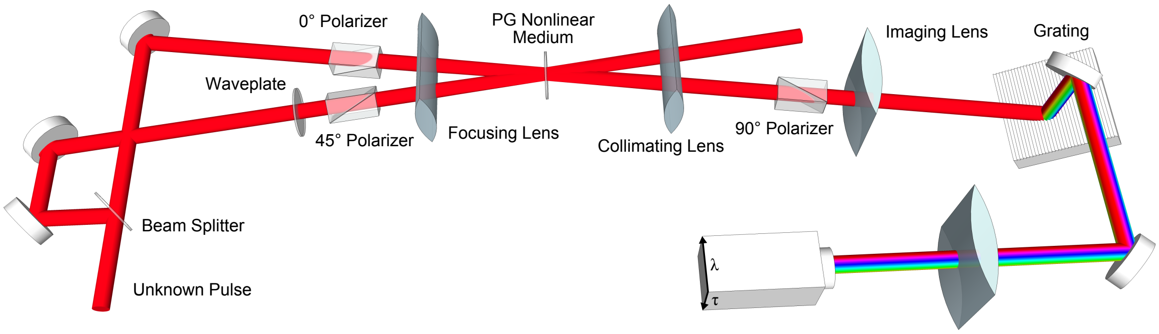

Figure 1.6: Experimental schematic of single-shot PG FROG. It is very similar to its multi-shot version with the spherical lenses replacing by cylindrical lenses and an extra cylindrical lens imaging the beams-crossing dimension of the nonlinear medium onto the camera.

generates the FROG trace with no scanning. However, the temporal resolution of the device is limited by the finite size of the camera pixel. In addition, single-shot FROG requires calibration in both temporal and spectral domains. A detailed discussion on calibration is presented in Chapter 3.3.

In addition to standard single-shot FROG, GRENOUILLE (a simplifed version of single-shot SHG FROG) was developed to measure relatively simple pulses such as the output of the Ti:sapphire laser on a single-shot. It simplifies the SHG FROG setup by replacing the delay stage and the beam splitter with a Fresnel biprism which crosses the split replicas in the SHG medium at an angle. The SHG medium is imaged onto the camera mapping delay to horizontal axis of the camera for single-shot operation. The spectrometer is eliminated by using a thick SHG crystal which phase-matches different wavelengths at different incident angles due to its narrow phase-matching bandwidth [28–30]. In this work, GRENOUILLE is used to measure the reference pulses used in cross-correlation FROG (XFROG, see Chapter 1.3 for details) and to confirm our experimental results in simple cases.

1.3 Cross-correlation FROG

When a known reference pulse is available, it can be used to measure a more complex unknown pulse. This technique is called cross-correlation FROG (XFROG). The operation principle is the same as the self-referencing FROG, but with one of the replicas of pulse replaced by a known reference pulse (Figure 1.7). It is shown in numerical simulations that XFROG is a reliable and robust way to measure complex pulses [31]. Experimentally, XFROG has been used to measure different pulses, such as femto-Joule pulses, XUV pulses, single-cycle pulses, attosecond pulses, and ultra-broadband pulses. [32–39] In this work, all of the experimental studies are related to XFROG-based devices implemented in PG geometry.

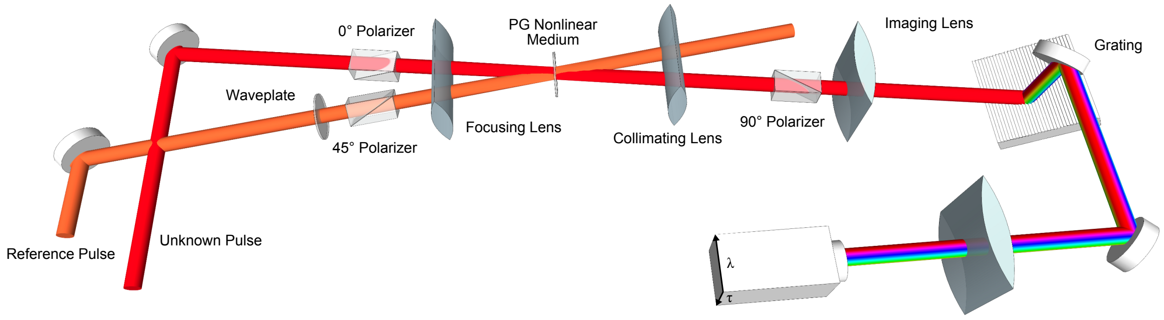

Figure 1.7: Experimental schematic of single-shot PG XFROG. The experimental setup is the same except for one of the replica of the unknown pulse in PG FROG is replaced by a known reference pulse.

1.3.1 Spectral phase interferometry for direct electric-field reconstruction

Spectral phase interferometry for direct electric-field reconstruction (SPIDER) is an ultrashort pulse measurement technique that utilize spectral-shear interferometry [40]. In SPIDER, a replica of the unknown pulse is generated. One of them pass through a Michelson interferometer to create a double pulse while the other one is chirped.

The two replicas are mixed in a nonlinear media to undergo sum-frequency generation (SFG). The spectrum of the SFG signal will experience spectral fringes and the spectral phase could be extracted from these fringes. However, it can be experimentally challenging to implement the technique and errors in calibration can potentially introduce large experimental errors.

1.3.2 Time bandwidth product

The time-bandwidth product (TBP) measures the complexity of a pulse. It is defined as the product between the width of $I(t)$ and that of $S(\omega)$. There are different definitions of these quantities; here the rms versions are used. They are defined as,

$$\begin{aligned}
\tau_{rms} &\equiv \sqrt{\langle t^2\rangle - \langle t\rangle^2} && (1.5)\\
\omega_{rms} &\equiv \sqrt{\langle \omega^2\rangle - \langle \omega\rangle^2} && (1.6)\\
TBP_{rms} &\equiv \tau_{rms}\omega_{rms} && (1.7)
\end{aligned}$$

where,

$$\begin{aligned}
\langle t^n\rangle &\equiv \int_{-\infty}^{\infty} t^n I(t)\,dt && (1.8)\\
\langle \omega^n\rangle &\equiv \int_{-\infty}^{\infty} \omega^n S(\omega)\,dt && (1.9)
\end{aligned}$$

In general, the higher the TBP is, the more complex the pulse is. GRENOUILLE is designed to measure relatively simple pulses, typically with TBP less than 10. In XFROG, pulses with TBP up to ∼1000 are measured [39]. The reference pulse used in XFROG is much simpler, usually with TBP less than 5.

1.4 Thesis outline

This thesis focuses on the development of single-shot FROG techniques measuring the intensity and phase of complex pulses. Chapter 2 discusses the multi-shot coherent artifact effect on FROG and SPIDER measurement. Chapter 3 describes an extension on single-shot FROG that is used to measure two independent, unknown pulses simultaneously at same or different carrier wavelength with TBP of up to 6. Chapter 4 introduces a modification on single-shot XFROG which increases the temporal range by the use of pulse-front tilt (PFT) and thereby measure long complex pulses with tens of ps in duration and TBP of ∼260. Chapter 5 details the challenges of supercontinuum (SC) measurement and how to extend XFROG to characterize SC on a single-shot.

CHAPTER II

COHERENT ARTIFACT

2.1 Motivation

Most of modern ultrashort pulses measurements, including FROG and SPIDER, have single-shot capacities which mean that they can characterize the intensity and phase of an individual pulse on a single-shot. However, multi-shot operation is sometimes used because of various practical reasons. For example, the pulse energy is too low which requires integrating over many pulses to enhance the signal-to-noise ratio. In the case of measuring very long pulses (ps or ns), a scanning delay stage is often used to achieve the required long temporal range on multi-shot.

When a multi-shot measurement is made, it is only valid if all the pulses involved in the measurement are identical. If an unstable pulse train is being measured, an effect called coherent artifact (CA) can result in a wrong interpretation of the pulse. The terminology of CA comes from multi-shot AC measurement which a narrow spike is located at the zero time delay with a broad structureless background (Figure 2.1). The narrow spike corresponds to the non-random, or coherent, component of the pulse train being measured. It is often mistaken as the pulse length in AC measurement. The actual pulse length is, however, almost always indicated by the temporally much broader background. The correct estimation of the pulse duration should take into account of the much longer, random, or incoherent, pulse component. The CA was

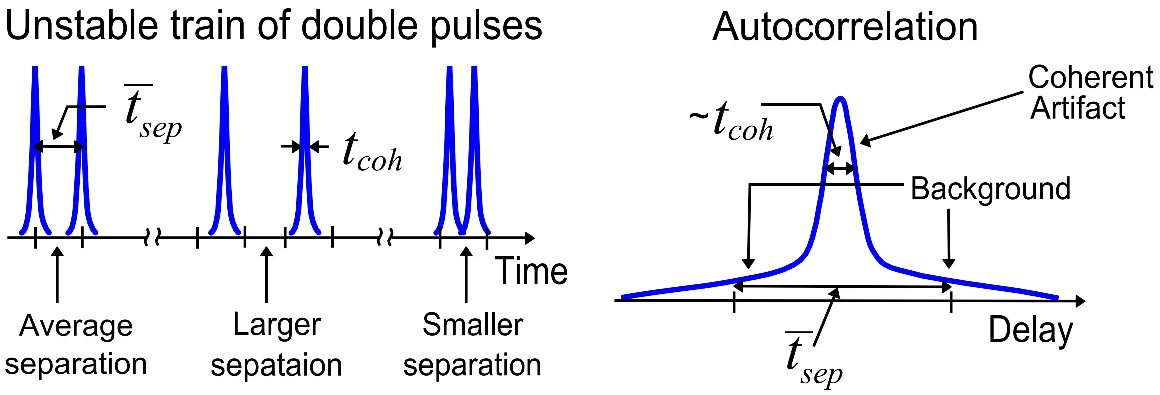

Figure 2.1: Illustration of coherent artifact in autocorrelation. A train of variably spaced double pulses and their multi-shot autocorrelation. The coherent artifact results from the short nonrandom coherent component of the double pulses (a single pulse), while the broader background results from the overall average pulse length (the combination of both pulses). This trace is typical of autocorrelations of nearly all trains of unstable complex pulses.

first shown by Fisher and Fleck [41] and later studied by others [42].

The best solution to avoid the CA is to perform a single-shot measurement in which only one pulse is measured at a time. When multi-shot measurement is inevitable, extreme caution should be used to interpret the result. In fact, when a measurement averages over thousands or even millions of pulses (they are all different) to generate one data set, it is impossible to return a single correct result that represents thousands of different pulses. The natural question to ask is how modern intensity and phase measurement techniques, which do yield the pulse intensity and phase for a stable train of identical pulses, perform under such circumstances. In this chapter, the performance of multi-shot FROG and SPIDER measuring unstable pulse-trains are investigated by numerical simulations [43].

2.2 Analytical calculation

The SPIDER trace is the spectral measurement of the pulse and its frequency-sheared and time-delayed replica. It is relatively easy to write down its analytical formula to see how it responds in simple situations. The equation governing the single-shot SPIDER trace is,

$$\begin{aligned} S_{SPIDER} &\propto |E(\omega) + E(\omega + \Delta\omega)\exp(i\omega T) \\ &+ E_{rand}(\omega) + E_{rand}(\omega + \Delta\omega)\exp(i\omega T)|^2 \end{aligned} \tag{2.1}$$

where T is the time delay between the replica, $\Delta\omega$ is the spectral shear, $E(\omega)$ is the non-random component of the E-field, and $E(\omega + \Delta\omega)\exp(i\omega T)$ is the spectrally sheared and temporally delayed replica. The subscript "rand" indicate the random component of the signal. Expanding equation 2.1 yields,

$$\begin{aligned} S_{SPIDER} &\propto |E(\omega)|^2 + |E(\omega + \Delta\omega)|^2 + |E_{rand}(\omega)|^2 + |E_{rand}(\omega + \Delta\omega)|^2 \\ &+ 2Re\{E^*(\omega)E(\omega + \Delta\omega)\exp(i\omega T) + E^*(\omega)E_{rand}(\omega) \\ &+ E^*(\omega)E_{rand}(\omega + \Delta\omega)\exp(i\omega T) + E^*(\omega + \Delta\omega)\exp(i\omega T)E_{rand}(\omega) \\ &+ E^*(\omega + \Delta\omega)E_{rand}(\omega + \Delta\omega) \\ &+ E^*_{rand}(\omega)E_{rand}(\omega + \Delta\omega)\exp(i\omega T)\}. \end{aligned} \tag{2.2}$$

Note that terms containing only one random field sum to zero when averaging over multi-shot, even if only zeroth-order phase of the random pulse is allowed to vary. Thus, any terms that have only one factor of the random field $E_{rand}(\omega)$ will sum to zero in a multi-shot average, this simplifies the equation to:

$$\begin{aligned} S_{SPIDER} &\propto |E(\omega)|^2 + |E(\omega+\Delta\omega)|^2 + |E_{rand}(\omega)|^2 + |E_{rand}(\omega+\Delta\omega)|^2 \\ &+ 2Re\{E^*(\omega)E(\omega+\Delta\omega)\exp(i\omega T) \\ &+ E^*_{rand}(\omega)E_{rand}(\omega+\Delta\omega)\exp(i\omega T)\} \end{aligned} \tag{2.3}$$

and writing the equation in terms of the spectra, $S(\omega)$ and $S_{rand}(\omega)$, spectral phases, $\varphi(\omega)$ and $\varphi_{rand}(\omega)$ yields:

$$\begin{aligned} S_{SPIDER} &\propto S(\omega) + S(\omega+\Delta\omega) + S_{rand}(\omega) + S_{rand}(\omega+\Delta\omega) \\ &+ 2\sqrt{S(\omega)S(\omega+\Delta\omega)}\cos\left[\varphi(\omega+\Delta\omega) - \varphi(\omega) + \omega T\right] \\ &+ 2\sqrt{S_{rand}(\omega)S_{rand}(\omega+\Delta\omega)}\cos\left[\varphi_{rand}(\omega+\Delta\omega) - \varphi_{rand}(\omega) + \omega T\right]. \end{aligned} \tag{2.4}$$

The cosines terms can be expressed by using the group delay as a function of frequency for each component, $\tau(\omega) = d\varphi/d\omega$ and $\tau_{rand}(\omega) = d\varphi_{rand}/d\omega$, and take the average of multiple pulses:

$$\begin{aligned} S_{SPIDER} &= S(\omega) + S(\omega+\Delta\omega) + \langle S_{rand}(\omega)\rangle + \langle S_{rand}(\omega+\Delta\omega)\rangle \\ &+ 2\sqrt{S(\omega)S(\omega+\Delta\omega)}\cos\left[\tau(\omega)\Delta\omega + \omega T\right] \\ &+ 2\langle\sqrt{S_{rand}(\omega)S_{rand}(\omega+\Delta\omega)}\cos\left[\tau_{rand}(\omega)\Delta\omega + \omega T\right]\rangle \end{aligned} \tag{2.5}$$

where the angle brackets denote the multi-shot average. The first line of equation 2.5 is the sum of the spectra. The second lines is the usual SPIDER fringe term from which the pulse spectral phase is retrieved, but only for the nonrandom component of the pulse. The last line is the SPIDER fringe term for the random component of the pulse. It is obvious that any variations in the spectral phase of the random component, even just the arrival time $\tau_{rand}(\omega_0)$ (the first-order spectral phase), will cause the last term in the equation to wash out. This leaves only the spectral background and the SPIDER term for the coherent, non-random component of the pulse being measured by the spectrometer. Specifically, arrival-time variations over a range of $2\pi/\Delta\omega$ clearly wash this term out completely, making a variable-delay satellite pulse invisible to SPIDER (the case of Figure 2.1), an effect anticipated in reference [44]. As the arrival-time effect is clear from equation 2.5, the random and non-random components of the pulses are centered to remove this effect. The effects of higher-order spectral phase fluctuations are difficult to observe from the expression, thus it will be explored in the numerical simulations.

The general expression for a FROG measurement is:

$$I_{FROG}(\omega,\tau) = \left| \int_{-\infty}^{+\infty} E(t)\, E_g(t-\tau) \exp(-i\omega t)\, dt \right|^2 . \tag{2.6}$$

This is the Fourier transform of the signal field, created by the interaction of the pulse, $E(t)$, its gate, $E_g(t-\tau)$, in the nonlinear medium. The measured trace is a function of frequency ω and delay τ. The gate function depends on the nonlinearity. In our case, SHG FROG, it is the field itself. Expanding equation 2.6 with the sum of random and non-random components finds no obvious cancellations due to the presence of the Fourier transform in the equation. Therefore, no further analytical analysis for FROG measurement will be presented in this work.

2.3 Numerical simulation

For the simulations, the pulses were constructed consisting a non-random and a random component. The non-random component $E(\omega)$ was a flat phase Gaussian with temporal FWHM of $12\delta t$, where δt was the temporal sampling rate. The frequency sampling rate is $\delta\omega = 2\pi/N\delta t$, where N is the array size (4096). An equal-energy random component $E_{rand}(\omega)$ with the same spectrum, but with random spectral phase was added to $E(\omega)$. The resultant pulse was Fourier filtered by different amounts to generate two trains of variably structured pulses with different average complexities and durations [31]. The two random trains, each consisted of 5,000 pulses, had average temporal length of $26\delta t$ and $54\delta t$. The left column of Figure 2.2 shows typical pulses in the two trains. In SPIDER simulations, the frequency shear was chosen to be $30\delta\omega$, and the time delay ws chosen to be $300\delta t$. For both techniques, each individual pulse in the pulse train was used to generate a trace as in the single-shot configuration. These traces were then averaged over all pulses in the train. The generalized projection SHG FROG algorithm [28] and the Takeda SPIDER algorithm [45] were used to retrieve information from these simulated traces.

2.3.1 SPIDER

The middle column of Figure 2.2 shows the results of SPIDER with array size of 4096. The non-random train (top row) generates SPIDER trace with 100% spectral fringe visibility as shown in (a). The retrieved pulse has the correct intensity and phase. This set of data is not very interesting as the pulses in the train are identical, meaning that this is essentially a single-shot measurement.

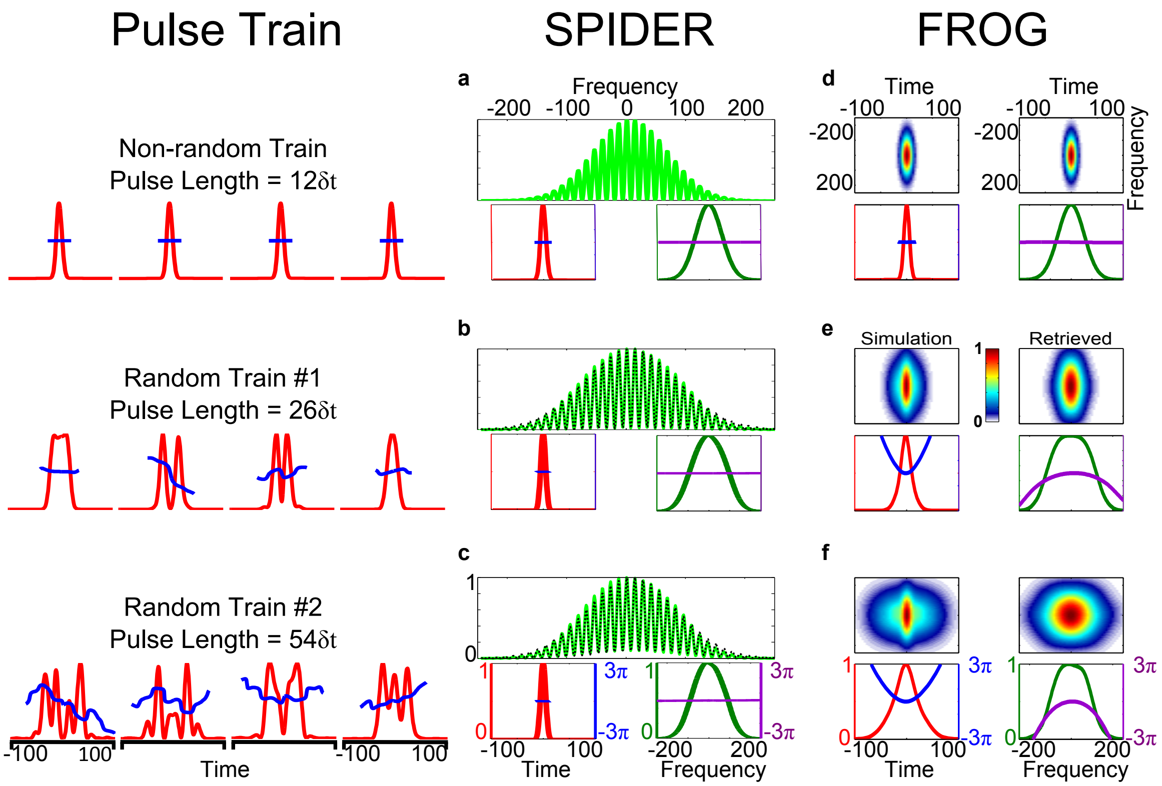

Figure 2.2: Non-random- and random-pulse trains of varying complexity, and simulated multi-shot SPIDER (array size: 4096) and SHG FROG (array size 256×256) measurements of them. The FROG traces created from numerical simulations are labeled as "Simulation" and the ones returned by the retrieval algorithm are labeled "Retrieved". Top row: non-random train of identical Gaussian flat-phase pulses. Middle and bottom rows: random-pulse trains of different average complexity and duration. Red curves are intensity, blue phase, green spectrum, and purple spectral phase. The black dotted SPIDER traces are fits assuming flat-phase Gaussian pulses and benign SPIDER-device misalignment: unequal SPIDER double-pulse energies. The fringe visibilities of the SPIDER trace are, from top to bottom, 100%, 98%, and 90%. The two random trains are retrieved with large G-errors: 0.83% and 1.4%, respectively. In all plots, all temporal units are in δt, and all frequency units are in $2\pi/(N\delta t)$, where N is 4096.

The first random train (middle row) creates SPIDER trace with spectral fringes with 98% visibility as shown in (b). The retrieved pulse has a pulse duration of $12\delta t$ with a flat temporal phase. This returned pulse is the same as in (a) which implies the retrieval result is equivalent to the non-random component of the pulse train. Same retrieval result is found for the second random train (bottom row) as shown in (c), the spectral fringe visibility is 90% in this case.

One has to study the SPIDER retrieval algorithm to gain insights of this result. The detail of the retrieval algorithm is out of the scope of this work, but, in brief, it uses the measured spectral fringes from the SPIDER trace (green solid line in (a), (b), and (c)) to retrieve the spectral phase. The broad background under the spectral fringes is ignored by the retrieval algorithm. The spectral phase is then added to an independently measured spectrum to construct the E-field. Since SPIDER is a spectral-interferometric technique, the random component of the pulse averages out with each other which reduces the fringes visibility to less than 100%. Also like AC, the broad background of the spectrum holds information about the random component of the pulses, however, it is ignored by the algorithm which makes SPIDER to underestimate the temporal pulse duration.

The reduced fringe visibility of the SPIDER trace is the only indication of instability in the measurement, but it is often ignored in experimental measurements because it can also arise from benign misalignment effects. SPIDER traces created by assuming one of the benign effects, unbalanced pulse energies of the SPIDER-device pulse pair, are shown in black dotted lines in Figure 2.2a, b and c. A pair of pulse with the same spectrum but had different pulse energies were used to generated these fits. They are indistinguishable from the SPIDER traces for the unstable pulse trains. Other benign effects are, for example, non-matching spatial profile, poor spatial overlap, and any damage in the optics of the experimental setup. In practice, it is extremely difficult to distinguish between background introduced by these benign, practical effects and more serious instability. Thus, only traces with close to 100% fringe visibility can accurately estimate pulse length in SPIDER measurements.

2.3.2 FROG

The right column of Figure 2.2 shows the results for FROG simulations. The FROG trace is first simulated in a 4096×4096 array (same as the dimension of the SPIDER trace) and then down sampled to a 256×256 array. Again, the non-random train generates FROG trace as it is a single-shot measurement, which gives the correct intensity and phase.

The two random trains generated FROG traces are indicated as "Simulation" (on the left) and the traces returned from the FROG algorithm are labeled as "Retrieved" (on the right). The measured traces show a spike similar to the CA of AC in the center, with a broad, structureless background around it (more prominent with random train 2). The retrieved FROG traces for the random trains show clear differences from the measured traces. The G-errors are 0.83% and 1.4% for train 1 and 2 respectively which are high for theoretical noiseless traces. The algorithm is unable to converge to small G-errors for both unstable trains on multiple attempts. This suggests that convergences are not possible for these traces because there are no single pulses can possibly cause the measured FROG traces. Even though convergences are not reached for both pulse trains, the pulse durations retrieved by FROG, $27\delta t$ and $52\delta t$ for train 1 and 2 respectively, are close to the average durations of the trains ($26\delta t$ and $54\delta t$). Because the FROG algorithm has been demonstrated to be quite robust [31], significant disagreement between measured and retrieved traces should be attributed to instability or measurement error of some types, rather than non-convergence of the retrieval algorithm. In practice, the retrieved FROG trace can serve as a consistency check for the measurement. When non-convergence is found in a multi-shot measurement, cautions should be used to examine the experimental setup and the laser system for instabilities and misalignments.

2.4 Conclusion

In this chapter, the retrieval results from single-shot configuration of FROG and SPIDER operated by averaging over multi-shot of unstable pulse trains are studied. We find that SPIDER retrieves an excellent estimate of the average spectral phase and the non-random component of the pulse train. But it fails to distinguish a train of long, unstable pulses from a train of short, stable pulses. In other words, multi-shot SPIDER measures only the coherent artifact. For FROG measurements, SHG FROG gives a close estimation of the average pulse duration, but fails to reproduce any structure of the pulse train. FROG provides an indication of instabilities via disagreement between the measured and retrieved traces and the corresponding large G-error.

To conclude, neither FROG nor SPIDER is able to capture the complete picture of instabilities in fluctuating pulse trains. Extreme cautions should be used with SPIDER measurements having less than 100% fringe visibility and FROG measurements having significant disagreement between measured and retrieved traces on multiple retrieval attempts. In situations in which instability is confirmed in the pulse train, a single-shot measurement should be employed for the correct measurement of the individual pulse.

CHAPTER III

DOUBLE-BLIND PG FROG

3.1 Motivation

In modern ultrafast optical experiments, there is often a need to simultaneously measure two independent unknown pulses. For example, ultrafast pump-probe spectroscopy in various applications, such as material characterization and coherent control, often uses two pulses of different colors and potentially pulse lengths, bandwidths and complexities. Its operation or temporal-resolution optimization requires measuring both the pump and probe pulses [46–49]. Also, applications involving nonlinear-optical processes, such as harmonic generation and continuum generation in optical fibers [11, 13, 18, 50], which generate output pulses at different wavelengths, require complete information on both the input and output pulses to understand the underlying physics or to verify that the process has occurred properly. In addition, a well-characterized reference pulse is sometimes needed to measure an unknown one. This also results in a two-pulse measuring problem. Therefore, a self-referencing technique that can simultaneously measure two different, independent pulses would be very useful. The technique should have minimal restrictions on wavelengths, bandwidths and complexities. As discussed in Chapter 2, single-shot operation capacity is also important because a multi-shot measurement of an unstable train of pulses that suffers from shot-to-shot fluctuations may lead to incorrect interpretation of the pulse.

While it is always possible to measure two pulses separately using two independent measurement devices, a single device that can measure two pulses simultaneously with minimum cost, space and complexity is desirable. Over the years, different techniques have been proposed to accomplish this two-pulse measurement task in a single device for fs-pulses, such as blind FROG [51–53] and very advanced method for phase and intensity retrieval of e-fields (VAMPIRE) [54, 55]. However, blind FROG suffers from non-trivial ambiguities that requires extra measurements like spectra of both pulses to achieve convergence [56]. VAMPIRE has a complicated experimental setup to introduce precise amounts of temporal and spectral modulations to complete the measurement, limiting itself from measuring complex pulses. Both blind FROG and VAMPIRE have limited use in fs-pulse measurements and the two-pulse measurement problem remains unsolved.

In this chapter, we experimentally demonstrate double-blind FROG (DB FROG) implemented in PG geometry, a technique based on blind FROG that can measure two pulses simultaneously on a single-shot without non-trivial ambiguities. Numerical studies show that the DB FROG retrieval algorithm is capable of retrieving extreme complex pulse pairs with TBP of 40. Unknown pulse pairs with same or different center wavelengths and TBP up to 6 are measured experimentally [57–59].

3.2 Background

Blind FROG is the first attempt to simultaneously measure intensity and phase information of two unknown pulses in a single device. It was proposed and demonstrated by DeLong *et al.* in 1995 [51]. Though blind FROG's non-trivial ambiguities made it not very useful in fs pulse measurements, its idea lead to the development of other techniques such as CRAB-FROG and DB FROG. Here, a brief review of blind FROG is given as background information.

The experimental schematic of blind FROG implemented in PG geometry is modified from a PG XFROG setup (Figure 1.7) by replacing the known reference pulse by another, to be measured, unknown pulse. One single FROG trace is generated as in PG XFROG. The mathematical expression for the recorded blind FROG trace is:

$$I_{BlindFROG}\left(\omega,\tau\right)=\left|\int_{-\infty}^{+\infty}dtE_{sig}\left(t,\tau\right)\exp\left(-i\omega t\right)\right|^{2} \tag{3.1}$$

where $E_{sig}\left(t\right)$ represents the signal field from the nonlinear interaction happening inside the nonlinear medium. The expression of $E_{sig}\left(t,\tau\right)$ varies depending on the gating geometry in the experimental apparatus. For example, $E_{sig}\left(t,\tau\right)$ in PG geometry is represented by:

$$E_{sig}\left(t,\tau\right)=E_{1}\left(t\right)\left|E_{2}\left(t-\tau\right)\right|^{2} \tag{3.2}$$

where $E_1\left(t\right)$ and $E_2\left(t\right)$ are the E-fields of the two unknown pulses to be measured. Once the blind FROG trace is measured, a retrieval algorithm modified from the standard FROG algorithm is used to retrieve the intensity and phase of both unknown pulses. It begins with random guesses of $E_1\left(t\right)$ and $E_2\left(t\right)$ and generates $E_{sig}\left(\omega,\tau\right)$

by Fourier transforming equation 3.2 with respect to t. The magnitude of $E_{sig}(\omega, \tau)$ is replaced by the square root of the measured blind FROG trace with the phase unchanged to generate a modified signal field, $E'_{sig}(\omega, \tau)$. $E'_{sig}(t, \tau)$ is generated by an inverse Fourier transform with respect to ω. The method of generalized projections is used to generate new guesses for the E-fields. An error function, Z, is defined as [51]:

$$Z = \sum_{t,\tau=1}^{N} \left| E'_{sig}(t, \tau) - E_1(t) \left| E_2(t-\tau) \right|^2 \right|^2 . \tag{3.3}$$

On odd iterations, the measured spectrum of pulse 2 is used to replace that of E_2, and a new guess for $E_1(t)$ is generated by minimizing Z with respect to $E_1(t)$. On even iterations, the operations on pulse 1 and 2 are reversed. The algorithm continues until the G-error between the measured and retrieved blind FROG traces is minimized.

It was shown in the original work that blind FROG needed the independently measured spectra of the two unknown pulses to remove potential ambiguities [51]. Later study showed that blind FROG had non-trivial ambiguities meaning that multiple unknown pulse pairs can result in an indistinguishable blind FROG trace [56]. Although blind FROG is not very useful in fs-pulse measurements, it inspires the attosecond pulse community to develop CRAB-FROG (a blind FROG like setup) which is capable of measuring two unknown pulses consisting of one attosecond pulse and one fs pulse [60, 61]. It also leads to the development of DB FROG which solves the two-pulse measurement problem for fs-pulses.

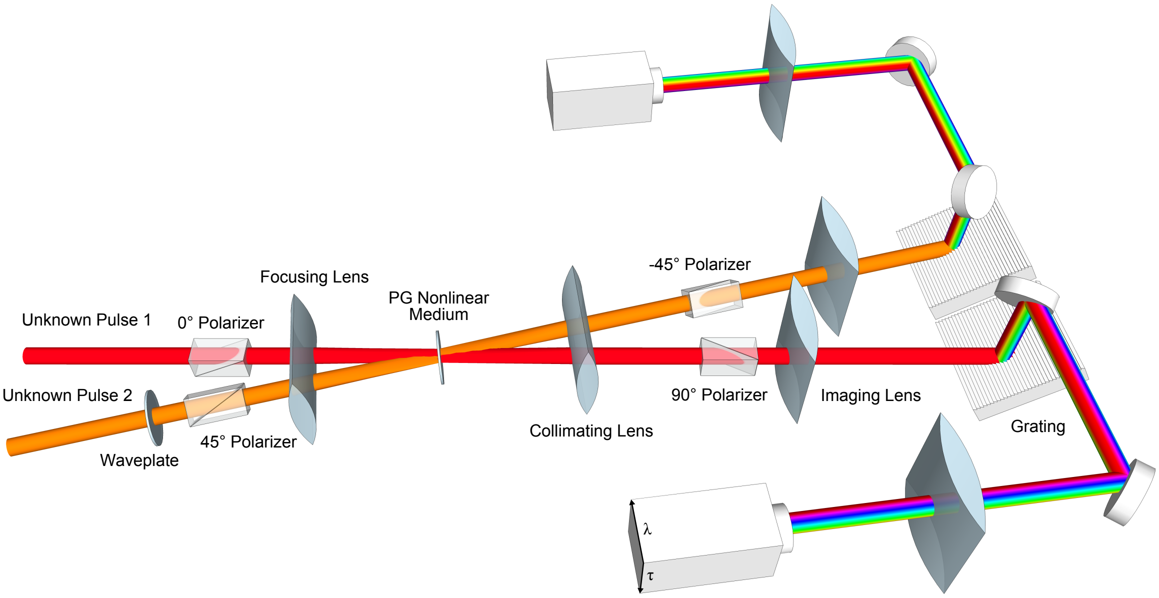

Figure 3.1: Experimental schematic for single-shot DB PG FROG. The experimental setup is modified from a single-shot PG XFROG setup (Figure 1.7) by replacing the known reference pulse with an unknown to be measured pulse. An additional analyzer at -45° and spectrometer are added to the unknown arm to measure an extra trace. Instead of one trace, two traces are measured in a given measurement.

3.3 DB FROG experimental setup

The schematic of single-shot DB FROG implemented in PG geometry (DB PG FROG) is shown in Figure 3.1. Unknown pulse 1 (red) was 0°-polarized and pulse 2 (orange) was 45°-polarized, both with respect to the horizontal plane. They had beam diameter of 5 mm and were crossed at an angle of 6° in a 250 μm thick fused silica (FS) parallel plate which served as the PG nonlinear medium. Both pulses were temporally and spatially overlapped in the FS plate so that they polarization-gated each other. The focusing and collimating lenses had a focal length of 100 mm. Like other single-shot FROG devices, the nonlinear medium was imaged onto the camera by a 300 mm cylindrical lens placed 600 mm away from it which map delay to spatial position of the camera. The experimental setup was similar to a blind PG

FROG setup, except for an additional polarizer, oriented at -45° and an additional spectrometer and camera (top right corner).

Since pulse 1 had a polarization 45° relative to pulse 2, the induced birefringence in the FS plate caused by the presence of pulse 1 was seen by pulse 2. As a result, pulse 1 induced time-gated polarization rotation in pulse 2. As the polarization of pulse 2 was also 45° relative to pulse 1, by the same mechanism, pulse 2 also caused a time-gated polarization rotation in pulse 1. In other words, the first pulse experienced the polarization-gating interaction in which the second pulse acted as the gate, and simultaneously, the second pulse experienced the polarization-gating interaction in which the first pulse was the gate. A grating-lens (600 line/mm grating and 100 mm cylindrical lens) spectrometer was placed in each beam path, so that two spectrograms were produced, one from each interaction.

The setup was calibrated by using a double-pulse generated by Michelson interferometer. This double-pulse was replicated by a beam splitter and used for both pulses. The temporal separation between the double-pulse was controlled by a variable delay arm in the Michelson interferometer. The spectrum of the double-pulse was measured by an independent spectrometer (HR-4000, Ocean Optics). The spectral fringes were recorded and the double-pulse's temporal separation was calculated. The calibration consisted of two steps.

First, using the double-pulse as pulse 1 and 2, two DB PG FROG traces were recorded, one in each arm. The number of pixel (px) separating the double-pulse in each FROG trace was measured. The calculated double-pulse's separation (in fs) was divided by the number of pixel to find the time-axes calibration (fs/px). Second, the analyzer (second polarizer) of the cross-polarizer pair in arm 1 was rotated slightly to allow a small portion of the pulse to pass through. The last part of the setup was a spectrometer which recorded the spectrum of the double-pulse. A straight line was fitted using the least-squares method between the spectra measured from the DB FROG apparatus and from the independent spectrometer. The slope of the linear fit represented the wavelength-axis calibration. This was repeated for arm 2.

Even though the experimental setup was symmetric between arm 1 and 2, it was extremely difficult to perfectly align both arms such that they had the same calibration. Thus, each arm was calibrated independently. The difference between calibrations for both arms was kept under 5%. After the time- and wavelength-axes were calibrated, the total temporal and spectral ranges can be calculated by using the total number of pixels inside the camera (1280×1024). Typical calibrations are: ∼2.5 fs/px and ∼0.065 nm/px for the apparatus presented in this chapter, but they vary according to the crossing angle between the two unknown pulses. In practice, the usable temporal range of the device is less than 100% due to the intensity drop-off away from the beam center. This effect is more pronounced in a third-order gating geometry (any gating mechanism involves a third-order nonlinear optical interaction), in which the signal intensity is proportional to the cube of the input intensity. Therefore, the usable temporal range of a PG XFROG setup is usually about 60-70% of the beam diameter. Under our experimental condition, the usable temporal range is ∼1.5 ps.

3.4 DB FROG retrieval algorithm

Once the two DB PG FROG traces are recorded, a retrieval algorithm modified from standard generalized-projections PG XFROG phase-retrieval algorithm is used to retrieve the two unknown pulses. Mathematically, the two traces in DB PG FROG are given by:

$$I_1(\omega,\tau) = \left| \int E_1(t) \left| E_2(t-\tau) \right|^2 \exp(-i\omega t)\, dt \right|^2 \tag{3.4}$$

$$I_2(\omega,\tau) = \left| \int E_2(t) \left| E_1(t-\tau) \right|^2 \exp(-i\omega t)\, dt \right|^2 \tag{3.5}$$

where $I_1(\omega,\tau)$ represents trace 1, with pulse 1 and pulse 2 acting as the unknown and the known reference pulses, respectively. In trace 2, the roles of pulse 1 and 2 are reversed. Each of the DB PG FROG traces is essentially a PG XFROG trace, but with the known reference pulse replaced by an unknown pulse.

In the standard generalized-projections XFROG phase-retrieval algorithm, the known reference pulse is the gate pulse, and the unknown is retrieved by using this gate pulse. DB FROG has two unknown pulses, instead of one known and one unknown pulses. The DB FROG retrieval problem consists of two linked XFROG retrieval problems: in order to retrieve one pulse correctly, the other pulse must be known, and vice versa. The flow chart of DB FROG retrieval algorithm (PG geometry is used here, but other implementations of other geometries are straight forward) is shown in Figure 3.2. It begins with random initial guesses for both $E_1(t)$ and $E_2(t)$. In the first half of the cycle, the DB FROG retrieval algorithm assumes $E_1(t)$ is the unknown pulse and $E_2(t)$ is the gate pulse. Even though a random guess is not close to the correct gate pulse, it is a sufficient starting point to initialize the retrieval process. The algorithm retrieves pulse 1 from trace 1, $I_1(\omega, \tau)$, as it is a PG XFROG problem. After the first half cycle, the retrieved pulse 1 is not the correct pulse, because pulse 2 is not the correct gate pulse to begin with. The returned $E_1(t)$ is an better estimation to the correct answer that satisfies the $I_1(\omega, \tau)$. In the second half of the cycle, the roles of 1 and 2 are switched. Trace 2, $I_2(\omega, \tau)$, and the improved version of $E_1(1)$ (acting as the gate pulse) are used to retrieve $E_2(t)$. After one complete cycle, both improved versions of $E_1(t)$ and $E_2(1)$ are used as the inputs for the next cycle. This process is repeated until the two DB PG FROG traces generated from $E_1(t)$ and $E_2(t)$ match the experimentally measured traces, that is, the differences between the two measured and retrieved traces are minimized. Standard noise-reduction and background subtraction are performed on the two measured traces before running the retrieval algorithm. The convergence of DB FROG is defined, similarly to other standard FROG techniques by the G-error, one for each DB PG FROG trace.

The DB FROG algorithm was tested with simulated DB PG FROG traces. We found this process to be extremely robust. In simulations, we routinely retrieved pairs of complex pulses TBP of ~40, even with 1% Poisson noise added to simulate experimental conditions. Figure 3.3 shows one of the pulse pairs. The top row contains the two simulated traces generated by using a pulse pair with TBP of ~40. The retrieved traces (array size of 1024×1024) yield 0.1% G-error, which indicate an excellent fit. The retrieved pulses agree very well with the actual pulses (labeled as original) used to generate the traces for testing. No non-trivial ambiguities were found in the numerical work, except for the well-known trivial ambiguities of most pulse-measurement techniques, the zeroth and first-order spectral phase.

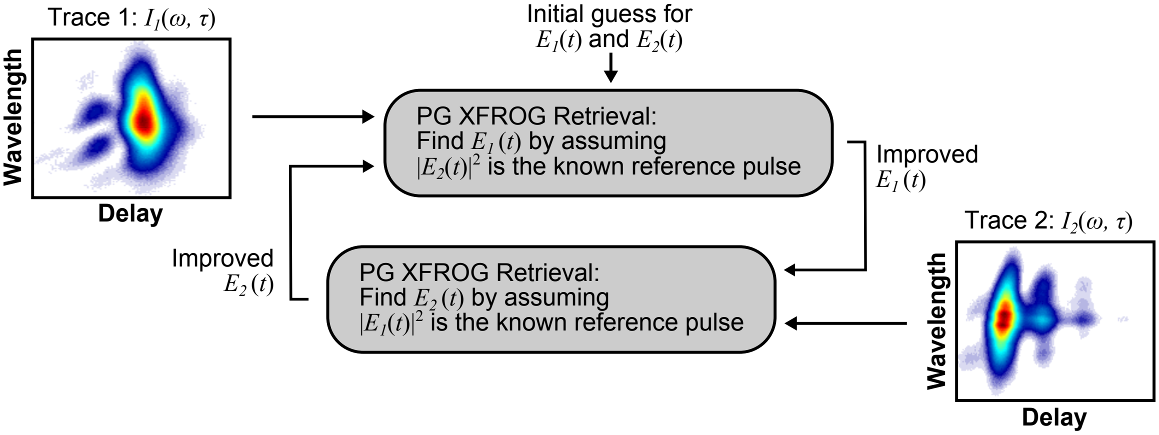

Figure 3.2: Flow chart of DB PG FROG retrieval algorithm with two sample DB PG FROG traces. The retrieval algorithm starts with initial guess for both $E_1(t)$ and $E_2(t)$. The first half cycle assumes $E_1(t)$ is the unknown pulse to be retrieved and $E_2(t)$ is the known reference pulse. An improved $E_1(t)$ is returned by using standard PG XFROG phase-retrieval algorithm using $I_1(\omega, \tau)$ as the input. In the second half cycle, the roles between $E_1(t)$ and $E_2(t)$ reverse and an improved $E_2(t)$ is returned by the algorithm. After each outer-loop, the algorithm returns improved version of $E_1(t)$ and $E_2(t)$. The convergence is defined by G-error, one for each DB FROG traces.

3.5 Results: Same center wavelength

A series of pulse pairs were measured to demonstrate that DB PG FROG can handle pulse pairs with different durations and complexities. The energy required for DB PG FROG to achieve a good signal-to-noise ratio were ~50 μJ for simple pulses pairs, and more energy was needed for more complex pulses pairs. We first measured DB PG FROG traces for a pair of simple pulses to test the experimental setup. The two resulting DB PG FROG (512×512 array) measurements are shown in figures 3.4 and 3.5. The DB PG FROG algorithm converged quickly for these traces, and the G-errors were 0.3% and 0.2%. We compared the measured simple pulses with independent measurements using a commercial GRENOUILLE device (Model 8-50USB, Swamp

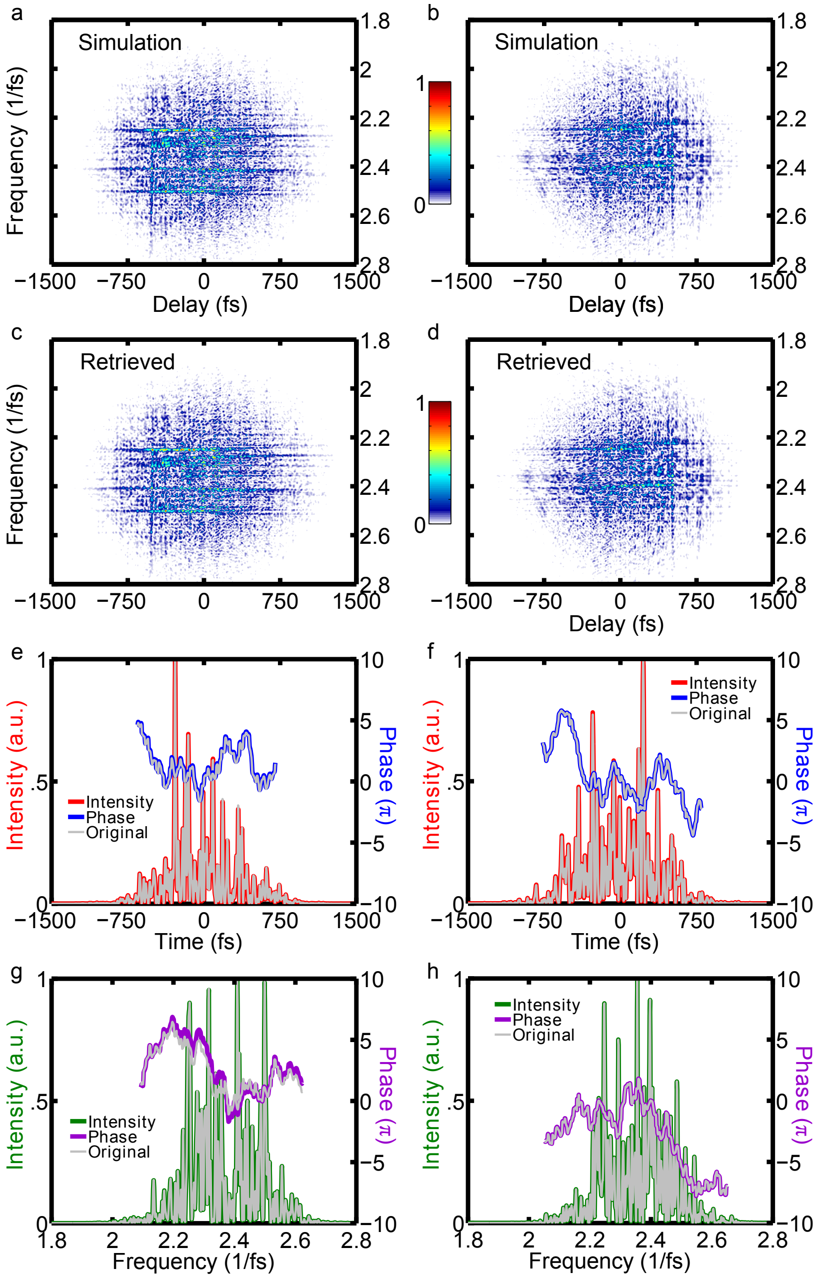

Figure 3.3: Simulation of DB PG FROG for two complex pulses with TBP of ∼40. The left column is for trace 1 and the right column is for trace 2. The two traces (a) and (b), created by numerical simulation are labeled as ”Simulation”, and their retrieved traces (c) and (d) are shown to their bottom. The retrieved intensities and phases are shown in (e) to (h) by the solid-color lines. The actual intensity and phase of the input pulses used to generate the ”Simulation” traces are shown as solid gray lines. The retrieved intensities and phases show excellent agreements with the input pulses except for the π phase jumps in (g). Both of the simulated pulses have time-bandwidth products of about ∼40, and 1% additive Poisson noise was added to the simulated traces to simulate noisy measurements.

Optics) for confirmation. Pulses 1 and 2 were measured by DB PG FROG to be 73 fs and 65 fs long respectively, in good agreement with the GRENOUILLE measurements of these pulse widths of 68 fs and 66 fs.

In the second data set, we generated two pulses having different amounts of chirp introduced into them by passing through different lengths of glass. Pulse 2 passed through an additional 2 cm of SF11 glass block, which increased its pulse width further. DB PG FROGs measured pulse width for pulse 1 was 74 fs, which is very close to the GRENOUILLE-measured pulse width of 71fs (Figure 3.6). DB PG FROG measured pulse 2 to be 148 fs long, in close agreement to the GRENOUILLE measurement of 147fs (see Figure 3.6). In addition to the pulse broadening, DB PG FROG and GRENOUILLE also agreed well on the phases of the two pulses.

We also measured a pair of pulses consisting of a simple pulse and a pulse train, which we generated by placing an etalon in one of the beams before the DB PG FROG. The measurements are shown in figures 3.8 and 3.9. The two traces yielded errors of 0.3% and 0.2%. The simple pulse was measured by DB PG FROG to be 64 fs long, in good agreement with the GRENOUILLE measurement of 65 fs (Figure 3.8). The etalon-generated temporal peak locations of the pulse train measured by DB PG FROG were 152 fs and 319 fs, which agreed well with the measurement made by GRENOUILLE indicating peak locations of 150 fs and 317 fs.

We modified the simple pulse and pulse train setup by chirping the simple pulse with a 2 cm SF11 glass block. The two G-errors were 0.4% and 0.2%. The pulse width of the chirped pulse measured by DB PG FROG was 133 fs, in good agreement with 136 fs measured by GRENOUILLE (Figure 3.10). The temporal peak locations

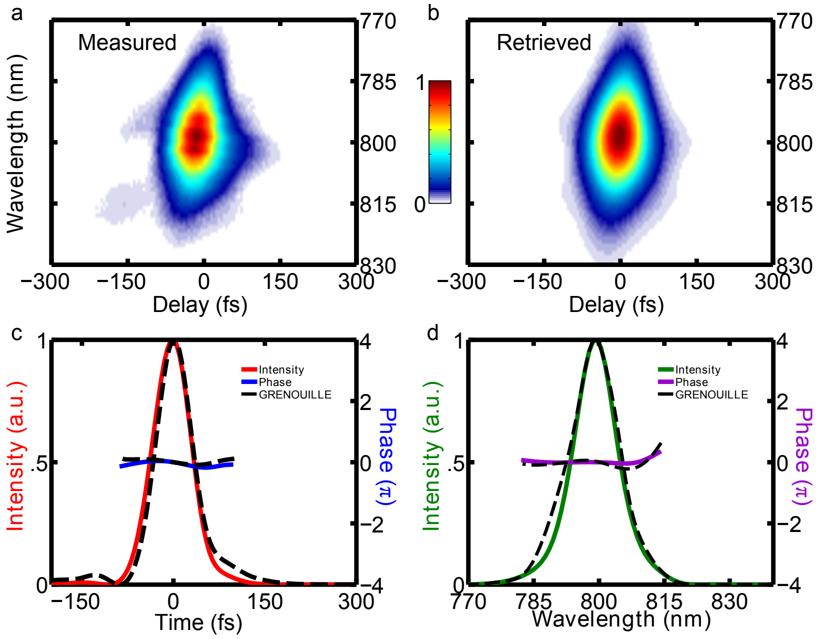

Figure 3.4: (a) The measured trace 1 for a simple pulse. (b) Retrieved trace 1 with a FROG error of 0.3%. (c) Retrieved pulse intensity and phase in time compared with an independent GRENOUILLE measurement. (d) The measured spectrum and the spectral phase compared with GRENOUILLE.

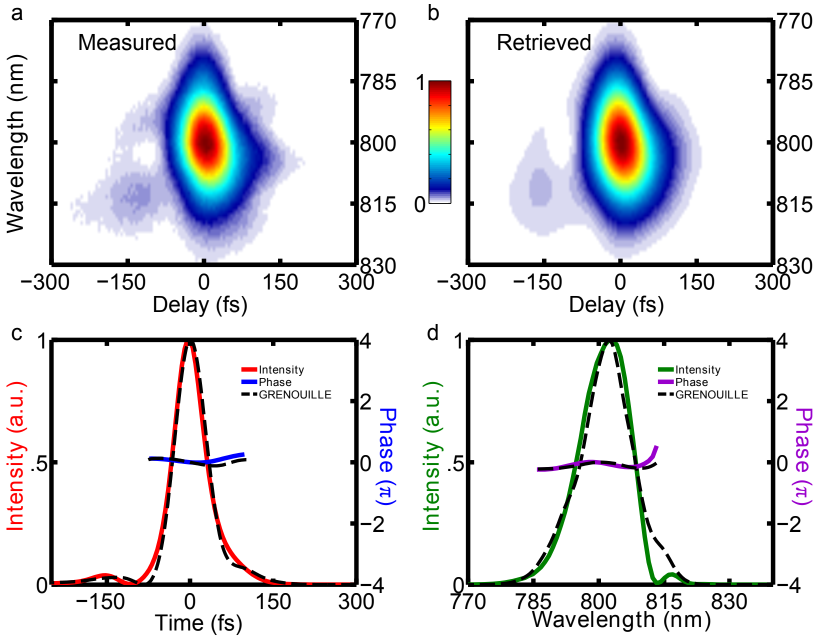

Figure 3.5: (a) The measured trace 2 for another simple pulse. (b) Retrieved trace 2 with a FROG error of 0.2%. (c) Retrieved pulse intensity and phase in time compared with an independent GRENOUILLE measurement. (d) The measured spectrum and the spectral phase compared with GRENOUILLE.

of the pulse train were found to be 157 fs and 318 fs by DB PG FROG. They were very close to the values of 155 fs and 318 fs in the GRENOUILLE measurement, as shown in Figure 3.11.

In our last set of measurement, one of the pulses was a chirped pulse train generated by passing a pulse train generated from an etalon through a 2 cm long SF11 glass block. The other was a chirped double-pulse created by passing a double-pulse generated from a Michelson interferometer through a 4 cm long SF11 glass block. Both of the pulses had a TBP of ∼4 and exhibited characteristics of chirped-pulse beating. The resulting DB PG FROG measurements of these two pulses are shown in figures 3.12 and 3.12. The G-errors of both arms were about 0.8%. Distortion in the temporal domain is observed in both arms, a clear indication of chirped-pulse beating, as expected. Independent measurements of the spectrum made with a spectrometer for both arms are plotted as black dashed lines. The spectral peak locations match very well between the DB PG FROG and spectrometer measurements. The good agreement between the spectra and our knowledge of the pulse characteristics based on its generation apparatus confirm that our retrieved pulses are correct.

3.6 Results: Different center wavelength

One advantage of implementing DB FROG in PG geometry is its unlimited phase-matching bandwidth as discussed in Chapter 1.2.3. This can be demonstrated by measuring two unknown pulses at two different center wavelengths, for example, 400 nm and 800 nm. The experimental apparatus, shown in Figure 3.14, was only slightly modified from the original one (Figure 3.1) to perform this measurement. An extra set of focusing and collimating lens was inserted in the 400 nm arm (shown in blue) to avoid chromatic aberration. The mirrors, lenses, and diffraction grating for the 400 nm arm were also replaced to improve the overall efficiency.

The first of data was a pair of simple pulses at 400 nm (blue) and 800 nm (red). The blue pulse was generated from SHG by the red pulse using a 1 mm thick BBO crystal (β-barium borate). The red pulse was not compressed to its shortest possible pulse width and was instead allowed to remain chirped. This is because we used pre-chirping of the red pulse to improve the SHG efficiency. The pulse energy for the blue arm was 105 μJ and that of red arm was 70 μJ. The measured and retrieved DB PG FROG traces are shown in figures 3.15 and 3.16. The G-errors were 0.32% and 0.30% for the blue and red pulses, respectively. Independent measurements made by GRENOUILLE, plotted in black dashed lines, show excellent agreement with the intensity and phase retrieved from DB PG FROG. The temporal FWHM of the 800 nm pulse were 73.2 fs and 73.5 fs, as measured by GRENOUILLE and DB PG FROG, respectively. The measured spectrum of the 400 nm pulse also agrees well with the spectral intensity retrieved by the DB PG FROG. Both pulses in this measurement have TBP of about 1.1.

Next, we generated a well-separated double-pulse at 800 nm using a Michelson interferometer and allowed the 400 nm pulse to remain simple. The DB PG FROG measurement is shown in figures 3.17 and 3.18. The G-errors were 0.83% for the blue pulse and 0.52% for the red one. Independent measurements of the spectrum made for both pulses are shown in black-dashed line. The fringes in the 800 nm pulse spectrum measured by a spectrometer and DB PG FROG overlap very well. The measured average fringe separation in the 800 nm pulse measured by the spectrometer and DB PG FROG were 3.82 nm and 3.91 nm respectively. Since the spectral fringes are created by a double-pulse, the pulse separation can be easily calculated from the fringes spacing with known center wavelength. Using the average fringe spacing measured by the spectrometer, the calculated pulse separation was 558 fs. The pulse separation retrieved by DB PG FROG was 547 fs, consistent with our calculation. The TBP of the well-separated double-pulse at 800 nm was about 6.2 and that of the simple pulse at 400 nm was about 1.1.

3.7 Discussion

Our results confirm the ability of DB PG FROG to fairly accurately measure complex and/or very-different-color pulses. While not all pulse details achieved perfect agreement with the independently measured quantities by the GRENOUILLE or the spectrometer, laser amplifier systems are unstable and experience shot-to-shot fluctuations and long-term drifts. Specifically, even though the fringe separation was consistent from shot to shot, the envelope of the spectrum tended to vary. Figure 3.19 shows four spectra measured within a short period of time. Fluctuations were observed, indicating slight instability of our laser amplifier system. Because simultaneous measurements of the same pulse by DB PG FROG and also by a spectrometer or GRENOUILLE are difficult, we did not attempt to do so. This could be responsible for the observed minor discrepancies, such as why the fringe separation in Figure 3.18 matches well, but some of the peaks have different intensity.

The imperfect spatial profile of the laser beam, a well-known issue to affect single-shot crossed-beam pulse measurements, may be an additional factor in the discrepancy. This is because GRENOUILLE uses a thick crystal (3.5mm in 8-50USB) as the nonlinear medium, which reduces the spatial profiles effect on FROG measurements [62]. On the other hand, due to the thin (250 μm) nonlinear medium in our DB PG FROG, it does not benefit as much from this effect. Thus, the spatial profile of the beam could also affect two measurements differently.

Another discrepancy between the measured and retrieved traces is that higher-frequency fringes were observed in the measured ones but not in the retrieved ones. One of measured traces with higher-frequency fringes is shown in Figure 3.20. The average fringe spacings were found to be 0.21 nm and 0.80 nm for the 400 nm arm and 800 nm arm respectively. The higher-frequency fringes are believed to be the result of multiple reflections from the 250 μm FS plate. The fringes generated at wavelength, λ, from a parallel plate with thickness, L, and refractive index $n(\lambda)$ can be calculated by:

$$\Delta\lambda = \left|\frac{\lambda^2}{2n(\lambda)L}\right| \tag{3.6}$$

Our calculation shows that the fringe spacings due to the FS plate were 0.20 nm at 400 nm and 0.83 nm at 800 nm. The results are consistent with the average fringe spacings measured from the traces. Despite the presence of the non-pulse-related (and hence unphysical) higher-frequency fringes, the retrieval algorithm is able to retrieve the pulse and essentially ignore them. Thus, the retrieved traces are free of the higher-frequency fringes, and the retrieved pulses do not suffer any ill effects from their presence.

The double-blind technique implemented with PG FROG inherits the advantages and disadvantages of standard PG FROG. For example, the nonlinear optical process of polarization gating is automatically phase-matched for all wavelengths, so pulses of even vastly different wavelengths can be used, and pulses with extremely large bandwidths and hence very complex temporal waveforms can be measured. Automatic phase-matching also occurs for all beam-crossing angles, including large ones. This allows large delay ranges in single-shot beam geometries, which map delay onto transverse position in the nonlinear medium and use crossed beams at large angles to achieve large delay ranges.

On the other hand, PG FROG requires high-quality polarizers with an extinction ratio of at least $\sim 10^5$. Calcite polarizers offer the required extinction ratio, but they are thick, so their use introduces non-negligible material dispersion and distorts the pulse, with the precise amount depending on the length of the pulse and its wavelength range. However, this is usually not a serious problem if the pulse is in the visible spectrum or near IR. Also, only the polarizer before the nonlinear medium matters, and its effect can be taken into account through simple post-processing after the measurement, in which the pulse is simply numerically back-propagated to obtain the input pulse. This is possible because the measurement yields the full intensity and phase verse time and frequency.

3.8 Conclusion

In this chapter we have demonstrated that DB PG FROG can be used to measure complex pulse pairs experimentally with TBP up to 6. It is also capable of measuring two unknown different-color pulses with center wavelengths of 400 nm and 800 nm. Numerical simulations suggest the retrieval algorithm is robust, reliable and able to retrieve complex pulse pairs with TBP up to 40. Experimental observations also show that the algorithm is capable of retrieving pulses accurately with the presence of unphysical distortions added to the traces. The unlimited bandwidth of DB PG FROG makes it extremely versatile in single-shot measurements for unknown pulse pairs.

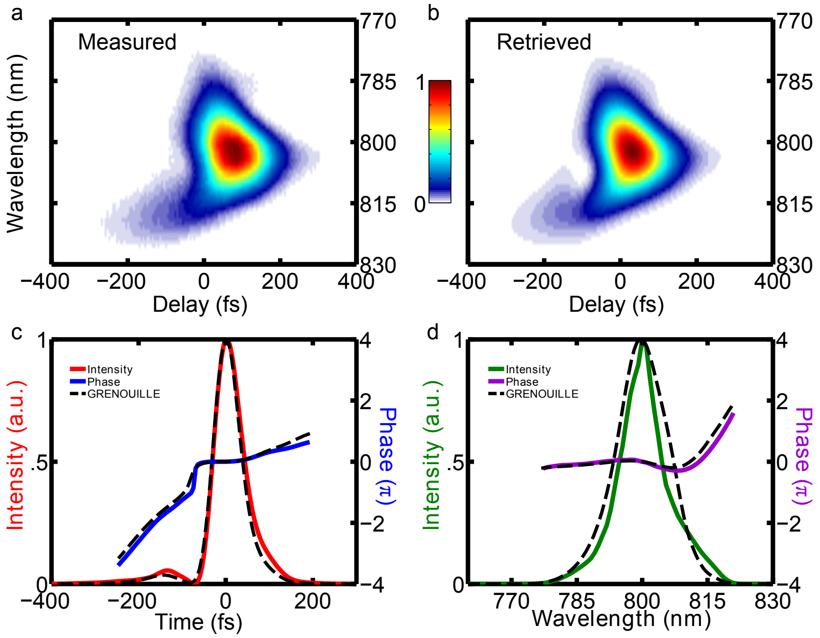

Figure 3.6: (a) The measured trace 1 for a simple pulse. (b) Retrieved trace 1 with a FROG error of 0.2%. (c) Retrieved pulse intensity and phase in time compared with an independent GRENOUILLE measurement. (d) The measured spectrum and the spectral phase compared with GRENOUILLE measurements.

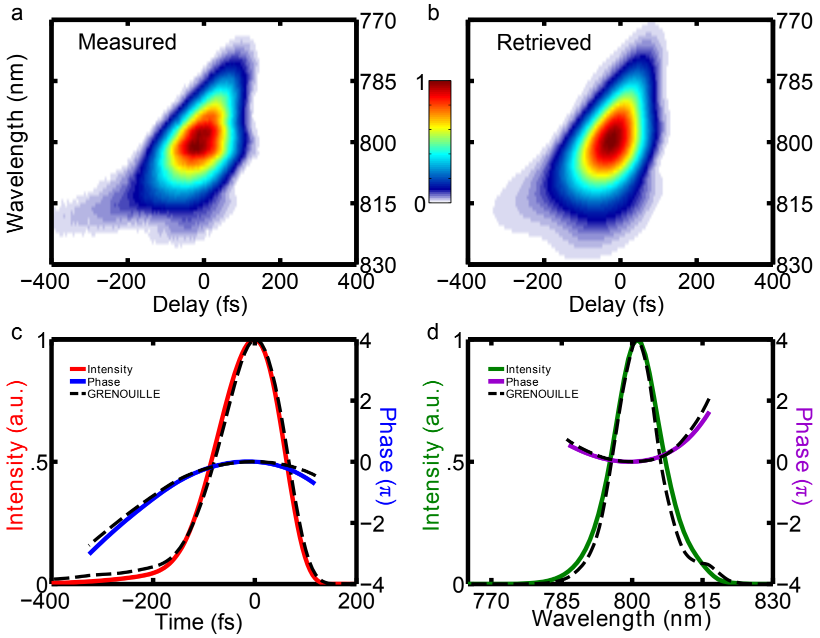

Figure 3.7: (a) The measured trace 2 for a simple pulse with more chirp. (b) Retrieved trace 2 with a FROG error of 0.3%. (c) Retrieved pulse intensity and phase in time compared with an independent GRENOUILLE measurement. (d) The measured spectrum and the spectral phase compared with GRENOUILLE measurements.

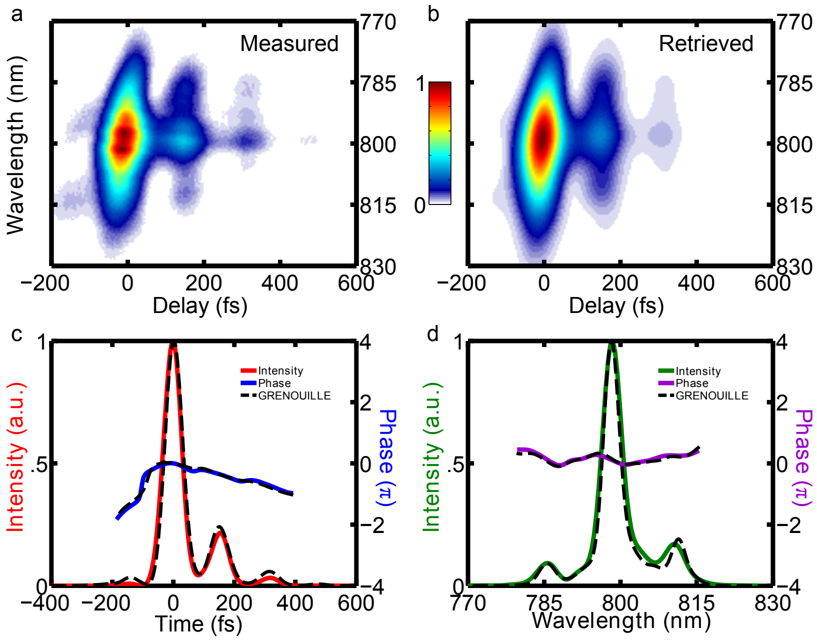

Figure 3.8: (a) The measured DB PG FROG trace 1 for the simple pulse. (b) Retrieved trace 1 with a FROG error of 0.2%. (c) Retrieved pulse intensity and phase in time compared with a GRENOUILLE measurement. (d) The measured spectrum and the spectral phase.

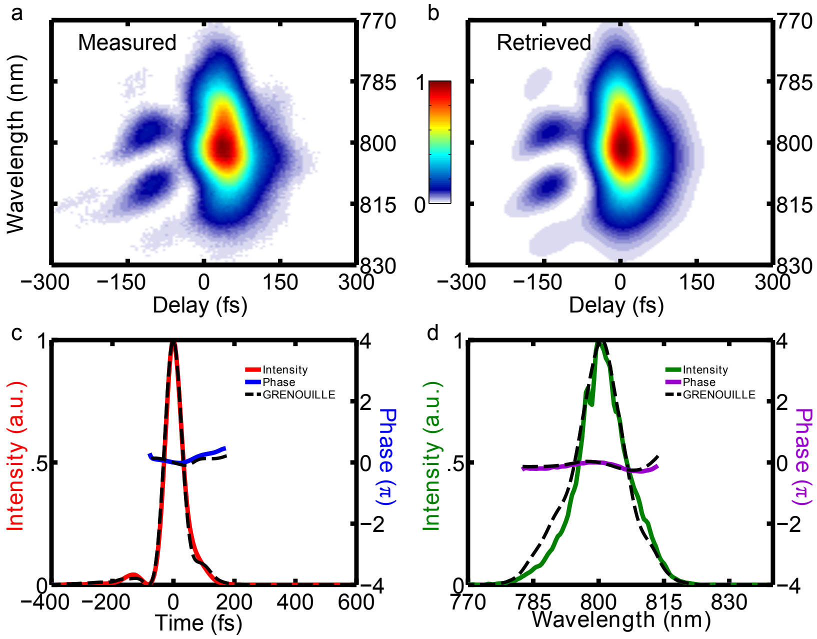

Figure 3.9: (a) The measured trace 2 for the pulse train from etalon. (b) Retrieved trace 2 with a FROG error of 0.3%. (c) Retrieved pulse intensity and phase in time: peak locations occur at 0 fs, 152 fs, and 319 fs in agreement with GRENOUILLE measurements. (d) The measured spectrum and the spectral phase compared with GRENOUILLE measurements.

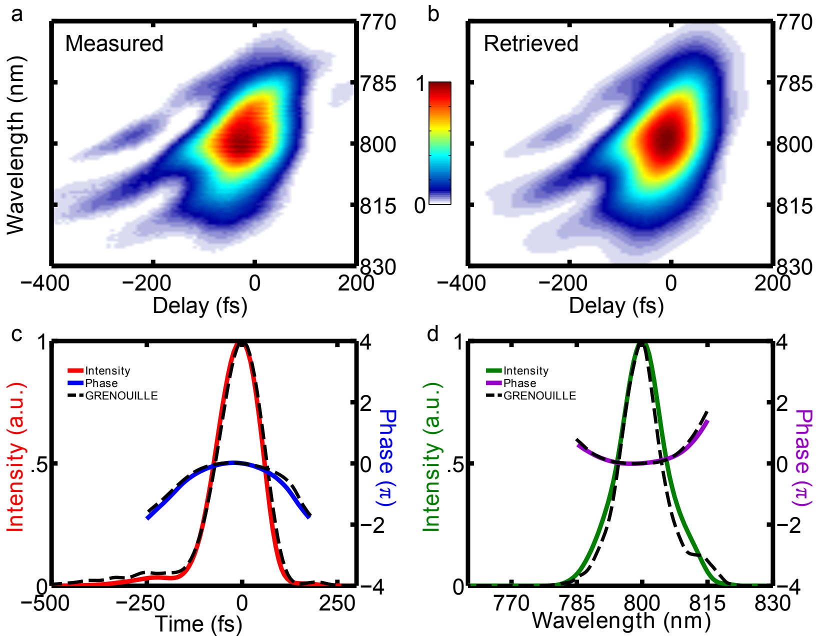

Figure 3.10: (a) The measured DB PG FROG trace 1 for the chirped pulse. (b) Retrieved trace 1 with a FROG error of 0.2%. (c) Retrieved pulse intensity and phase in time compared with a GRENOUILLE measurement. (d) The measured spectrum and the spectral phase.

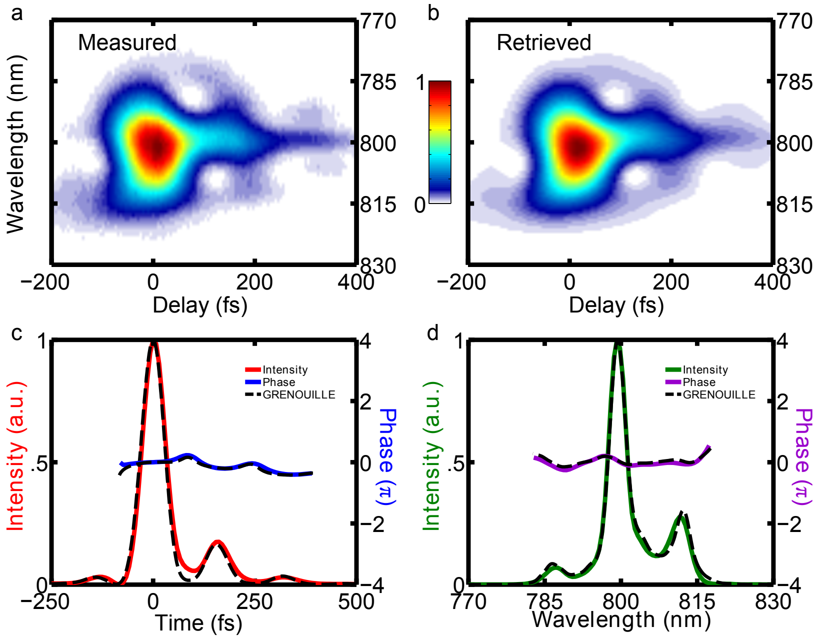

Figure 3.11: (a) The measured trace 2 for the pulse train from etalon. (b) Retrieved trace 2 with a FROG error of 0.4%. (c) Retrieved pulse intensity and phase in time: peak locations occur at 0 fs, 157 fs, and 318 fs in agreement with a GRENOUILLE measurements. (d) The measured spectrum and the spectral phase compared with GRENOUILLE measurements.

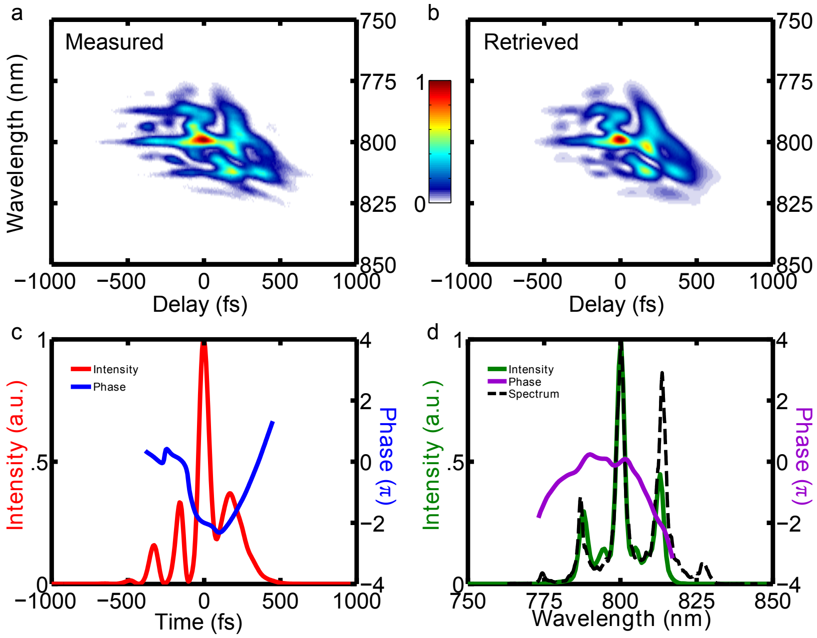

Figure 3.12: (a) The measured trace 1 for a chirped pulse train. (b) Retrieved trace 1 with a FROG error of 0.81%. (c) Retrieved pulse intensity and phase in temporal domain showing structures from chirped pulse beating. (d) The measured spectrum and the spectral phase compared with measurement made by a spectrometer.

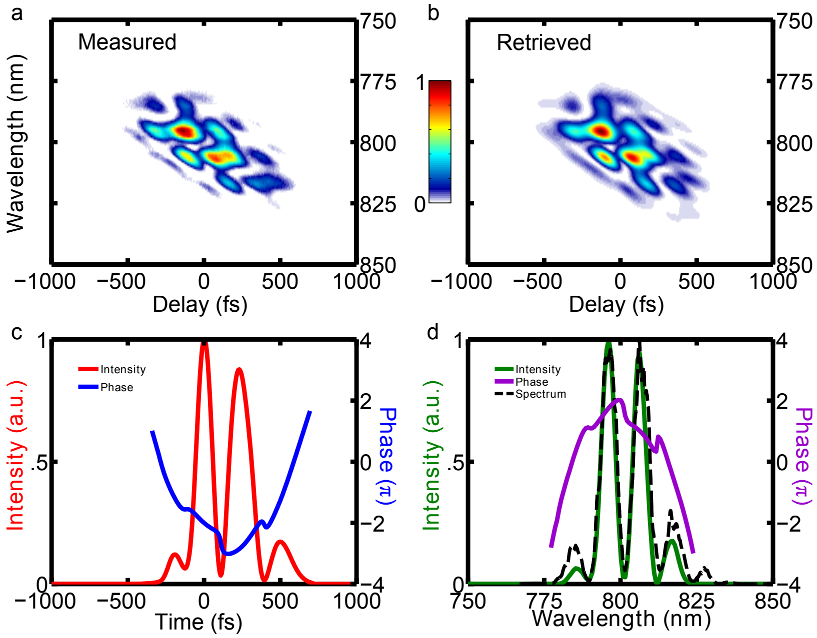

Figure 3.13: (a) The measured trace 2 for a chirped double-pulse. (b) Retrieved trace 2 with a FROG error of 0.74%. (c) Retrieved pulse intensity and phase in temporal domain showing structures from chirped pulse beating. (d) The measured spectrum and the spectral phase compared with measurement made by a spectrometer.

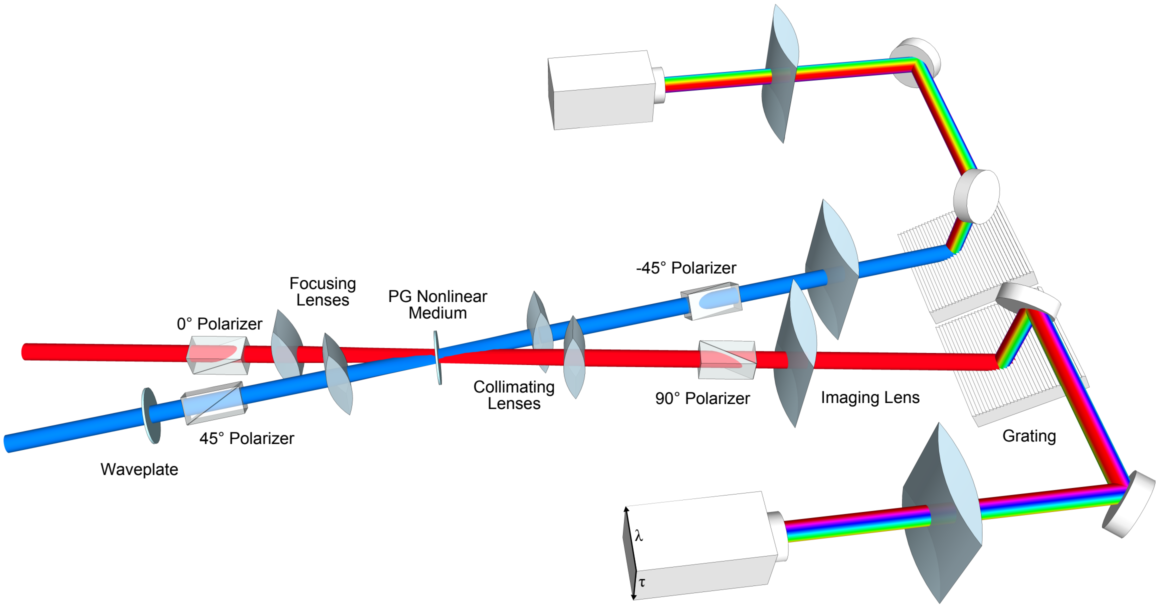

Figure 3.14: Experimental schematic for single-shot DB PG FROG for two colors pulses (400 nm and 800 nm). The experimental setup is similar to the same-color one. Individual pairs of focusing and collimating lenses are used to avoid chromatic aberration due to significant wavelength difference.

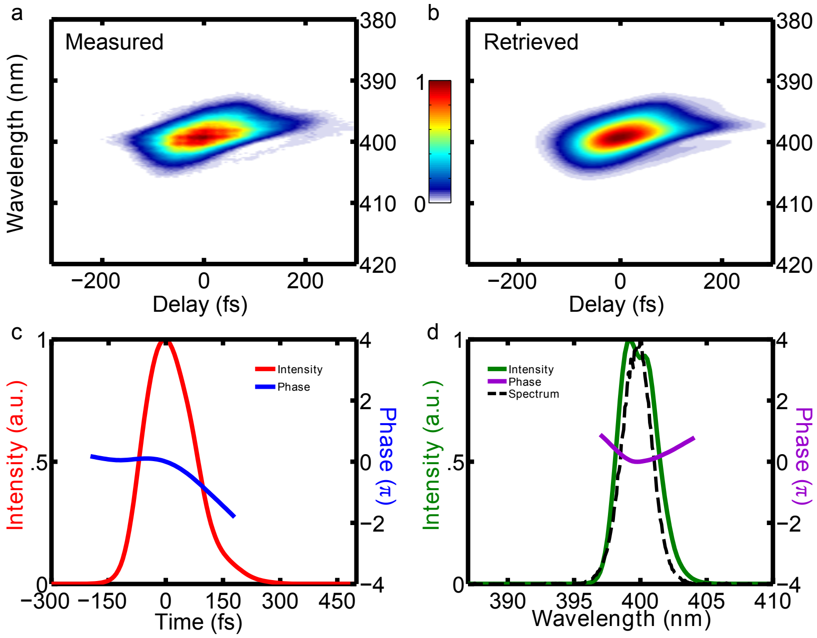

Figure 3.15: (a) The measured trace for a simple pulse at 400nm. (b) Retrieved trace with a FROG error of 0.32%. (c) Retrieved pulse intensity and phase in temporal domain showing structures from chirped pulse beating. (d) The measured spectrum and the spectral phase compared with measurement made by a spectrometer.

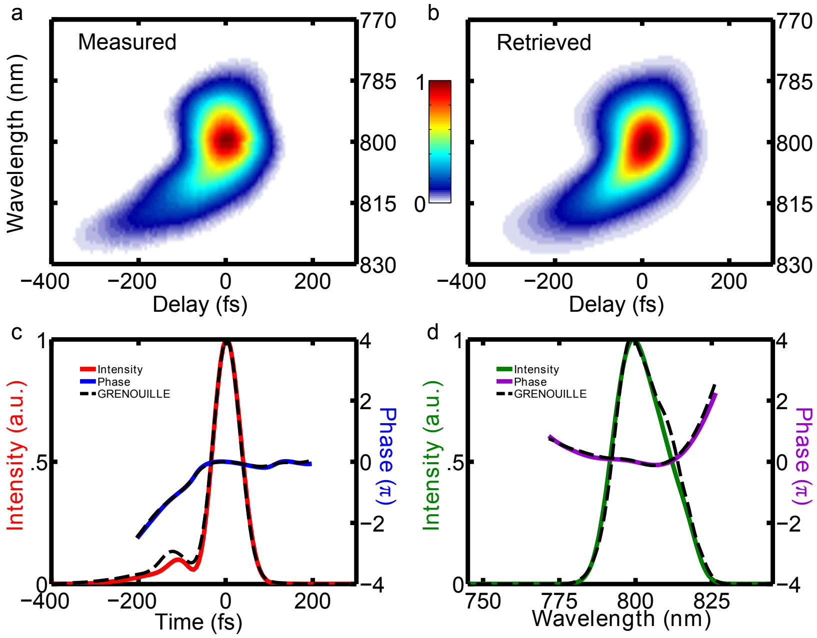

Figure 3.16: (a) The measured trace for a simple pulse at 800nm. (b) Retrieved trace with a FROG error of 0.30%. (c) Retrieved pulse intensity and phase in time compared with an independent GRENOUILLE measurement. (d) The measured spectrum and the spectral phase compared with those made using a GRENOUILLE.

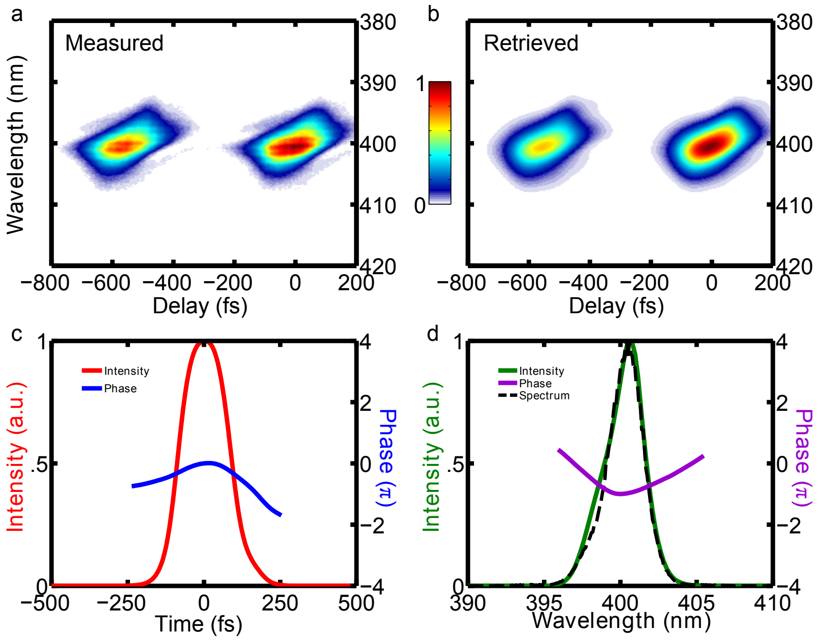

Figure 3.17: (a) The measured DB PG FROG trace for a simple pulse at 400nm. (b) Retrieved trace with a FROG error of 0.83%. (c) Retrieved pulse intensity and phase in temporal domain. (d) The measured spectrum and the spectral phase compared with a measurement made by a spectrometer.

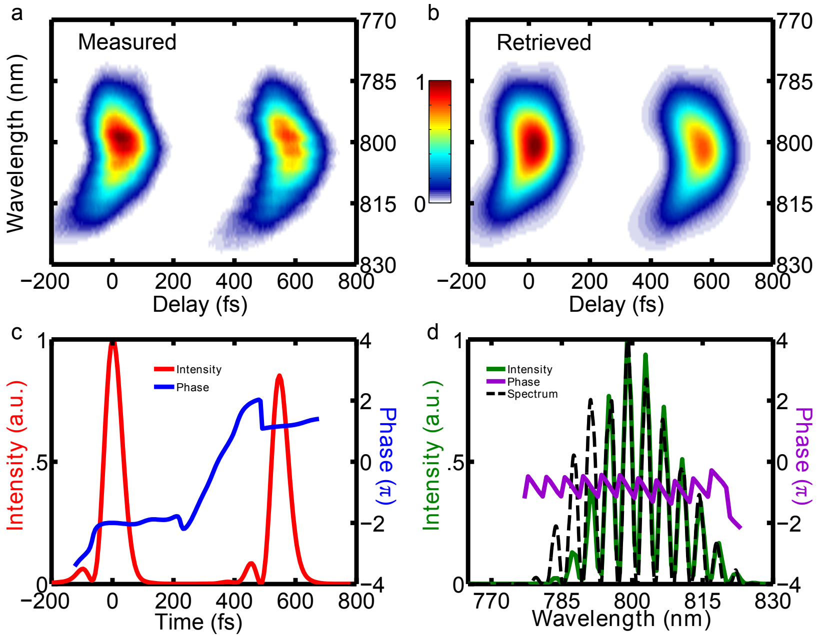

Figure 3.18: (a) The measured DB PG FROG trace for a well separated double-pulse at 800nm. (b) Retrieved trace with a FROG error of 0.52%. (c) Retrieved pulse intensity and phase in temporal domain. (d) The measured spectrum and the spectral phase compared with a measurement made by a spectrometer.

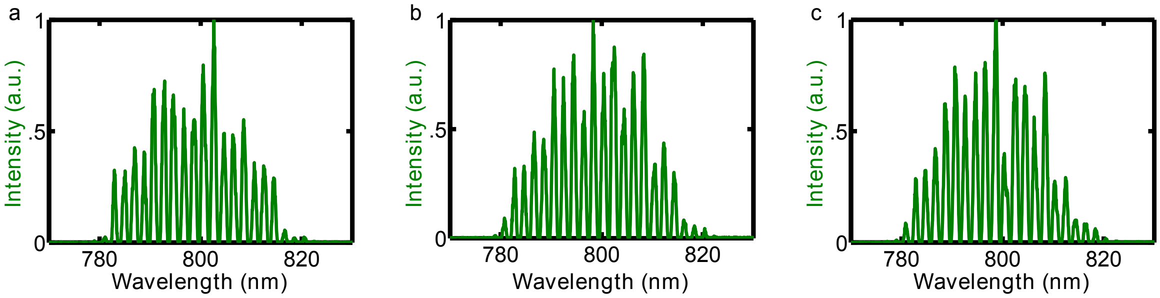

Figure 3.19: Three spectra of the regenerative amplifier outputs measured at different time. The spectra have same fringes separations but slightly different envelopes indicating fluctuations of the regenerative amplifier used in this work.

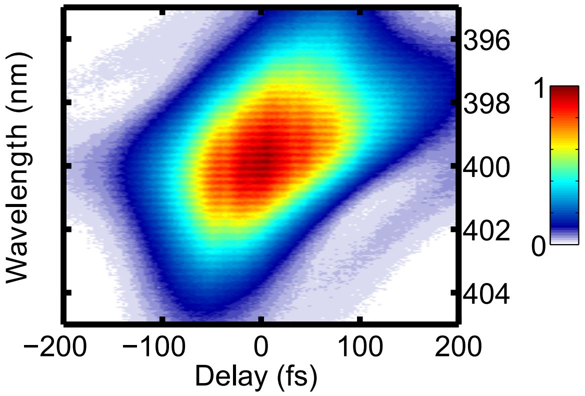

Figure 3.20: High frequency fringes recored in measured FROG trace due to multiple reflections inside the nonlinear medium.

CHAPTER IV

PG XFROG WITH PULSE-FRONT TILT

4.1 Motivation

Picosecond-long laser sources are widely used in scientific research, such as biological system imaging and control [63, 64], the study of laser induced effects and damage in materials [65–70], material processing [71–74], and ultrafast fluorescence spectroscopy [75]. They also find applications in industry because they are easier to work with than fs pulses, which broaden unacceptably in propagating through materials. For example, ophthalmological applications range from corneal ablation [76,77] to intraocular photo-disruption [78,79] to laser in situ keratomileusis (LASIK) [10]. Other health-care applications from hair and tattoo removal [80–83] to cancer treatments to dental drilling [84–86] use ps pulses. And they find use in material processing applications from glass cutting [87] to circuit-board etching [88] to micromachining [89–91]. The accuracy and efficiency of all of these applications depend heavily on the ability to measure the laser pulses. Thus a technique that can completely characterize many-ps-long pulses would be beneficial, not only to the scientific community, but also to the industrial and medical communities. While fs-long pulses are generally very accurately measured by the FROG family, much less attention has been devoted to the measurement of many-ps-long pulses. It is because they are actually more difficult to measure on a single-shot than fs pulses due to the much larger delay range and higher spectral resolution required to measure them.

The main approach for measuring many-ps-long pulses has long been multi-shot intensity autocorrelation using a scanning delay stage and optical nonlinearities such as SHG [92–94], two-photon photoconductivity [95,96], and two-photon fluorescence [97, 98] and high-order effects [99, 100]. Multi-shot interferometric autocorrelation [101, 102] using a scanning delay stage has also been demonstrated. Longer (few-hundred ps) pulses are routinely measured using fast detectors and ultrahigh-bandwidth oscilloscopes. These devices achieve single-shot operation, but they are extremely expensive and only yield the intensity, and not the phase. Modern pulse-measurement techniques like FROG can be naturally extended to measure many-ps-long pulses using a many-centimeter-long scanning delay line, but any such approach is also necessarily a multi-shot measurement, which is undesirable in many circumstances, especially when fluctuations exist in the laser system [43, 103].

Single-shot measurements of fs pulses are routinely achieved by crossing two pulses in the nonlinear medium at a large angle, which maps delay onto transverse position, yielding up to a few ps of relative delay. There is actually a well-known and simple method for performing single-shot measurements of many-ps-long pulses, and it involves the use of pulse-front tilt (PFT). Crossing two oppositely tilted pulses in the nonlinear medium can yield tens of ps of relative delay. In 1981, Wyatt and Marinero demonstrated the use of a diffraction grating to generate significant PFT for single-shot autocorrelation measurement with a temporal range of up to 80 ps [104]. More recently, Bowlan and Trebino extended the idea to even larger delays using an etalon to measure ns-long pulses with SHG FROG on a single shot [105]. However, these ideas have not been yet applied to the complete intensity-and-phase measurement of many-ps-long pulses, especially complex ones.

In this chapter, we demonstrate the use of PG XFROG with PFT introduced to the reference pulse. This extends the temporal delay range of the device by more than one order of magnitudes compared with devices without PFT. Double-pulses with temporal separation from 4 ps to 24 ps are measured using this device. The total temporal range is 28 ps [106].

4.2 Temporal range and geometrical smearing in single-shot geometry

Single-shot FROG measurements of fs-long pulses are routinely accomplished by crossing two beams at an angle of a few degrees inside the nonlinear medium. The nonlinear medium is then imaged onto a camera, which maps the temporal delay between the two beams to transverse position of the camera. Increasing the crossing angle increases the temporal range of the device. However, this is not possible for measuring pulses longer than a few ps: to achieve a delay range of 30 ps, an internal crossing angle of 58° , corresponding to an external crossing angle of about 89° (assuming fused silica is the nonlinear medium) is required.

4.2.1 Using pulse-front tilt to increase temporal range

Introducing PFT into the reference pulse of the PG XFROG setup can increase the temporal range while keeping the crossing angle small. Similar to equation 1.4, the temporal range of such setup can be derived by considering the schematics shown in Figure 4.1 (the case without PFT is shown again for comparison). The temporal range in each case can be calculated by,

$$\Delta T = \frac{d}{c}\tan\theta \tag{4.1}$$

$$\Delta T_{PFT} = \frac{d}{c}\left|\tan\left(\alpha-\theta\right)\right| \tag{4.2}$$

where ΔT and ΔT_{PFT} represent the temporal range without and with PFT respectively, d is the beam diameter, α is the PFT angle, and θ is the crossing angle inside the nonlinear medium. For easy comparison, θ and d in both (a) and (b) are set to be the same. It is clear that under the same experimental configuration, the introduction of large PFT into the reference pulse significantly increase the temporal range of the device. Unlike normal single-shot geometry, the large delay range is not achieved by a large crossing angle, but by the largely tilted pulse-front. This allows PG XFROG using PFT in the reference pulse to extend its temporal range to tens of picoseconds while keeping a small crossing angle.

4.2.2 Geometrical smearing

When measuring complex pulses of any length, it is important to consider geometrical smearings in the system. The first kind is the transverse geometrical smearing, in which a range of delays always occurs simultaneously due to the beam crossing angle. It smears out fine temporal details in measurements using standard beam geometries in which the delay is varied using a scanning delay stage. But it is inherently not a problem in single-shot beam geometries because this effect is what actually allows the measurement to be done in a single-shot.

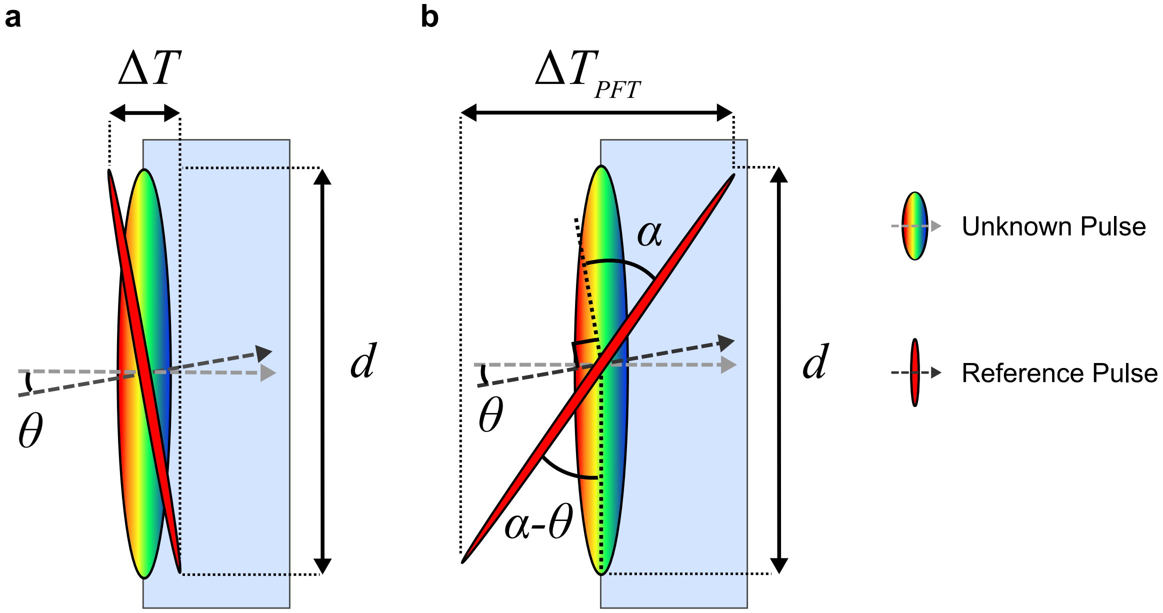

Figure 4.1: Schematics for temporal range calculation in FROG devices of single-shot geometry (a) without PFT and (b) with PFT. The unknown pulse is shown in rainbow and the reference pulse in red with arrows indicating their propagating direction. The PFT angle is α. The crossing angle θ and beam diameter d are the same in both cases. The light blue rectangle represents the nonlinear medium.

Unfortunately, another kind of geometrical smearing can still wash out details in the trace due to variations in the delay along the signal beam direction [28]. This is called longitudinal geometrical smearing which is identically zero in SHG-based FROG and autocorrelators because the constant delay line in SHG precisely matches the signal-beam propagation direction. In the PG geometry, however, like all other non-SHG non-collinear geometries which the signal-beam does not co-propagate with the constant delay line, longitudinal smearing is nonzero. The smearing depends, not only on the crossing angle, but also on the thickness of the nonlinear medium. Consider the case in Figure 4.2 (with PFT in the reference pulse), in which the center of the beam corresponds to the zero time delay at the entrance face of the nonlinear medium. As the two beams propagate at different directions, the center of the beam varies its delay. By the time the beams exit the nonlinear medium, the center of the beam will contain information from a range of delays. This range of delay, $deltat_{PFT}$, is the longitudinal smearing of the system. The longitudinal smearing of the system with PFT in the reference pulse can be calculated by,

$$\delta t_{PFT} = \frac{L}{c}\left(1 - \frac{\cos\alpha}{\cos\left(\alpha - \theta\right)}\right) \tag{4.3}$$

where L is the thickness of nonlinear medium, c is the speed of light, α is the PFT

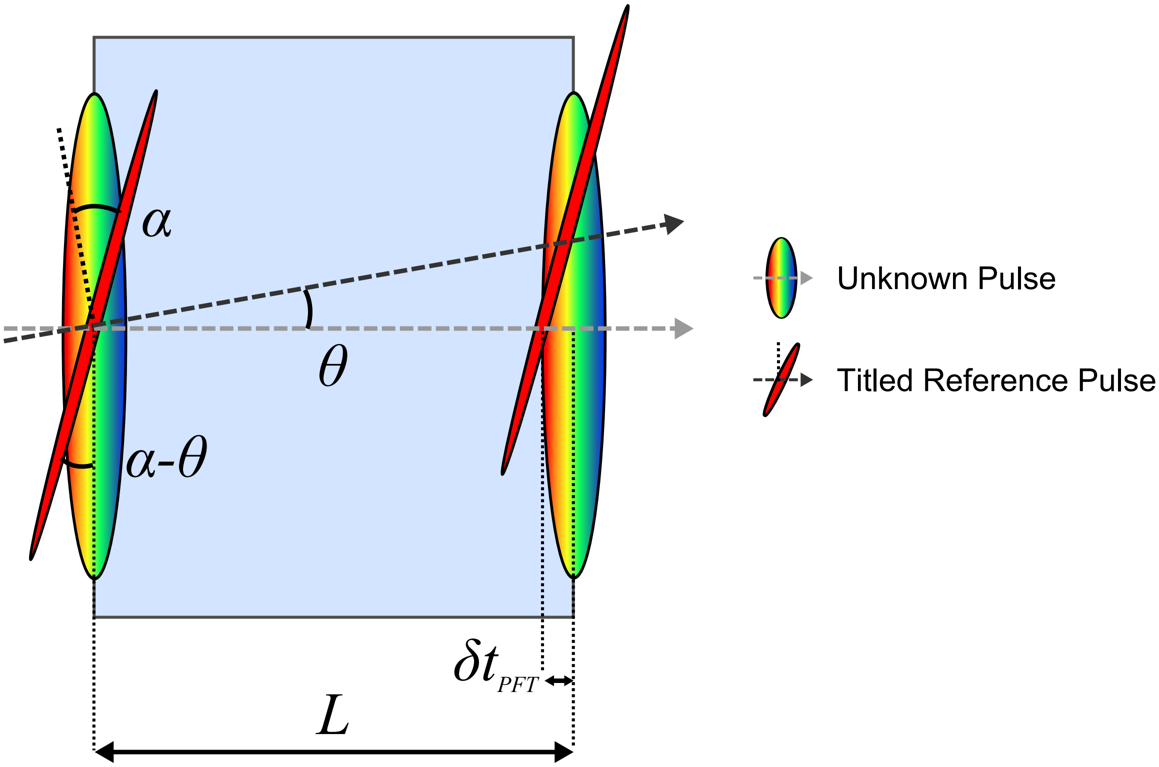

Figure 4.2: Illustration of longitudinal smearing in single-shot XFROG. A general case with arbitrary internal crossing angle, θ, and pulse-front tilt angle, α. The rectangle with thickness, L, represents the nonlinear medium. The unknown and reference pulses are shown in rainbow color and red respectively with the arrow showing the propagating direction. The nonlinear signal propagates along the same direction as the unknown pulse. In the center of the signal beam at the front of the crystal, the reference pulse gates the green part of the unknown pulse. At the back of the crystal, the reference pulse gates the red part of the unknown pulse. Thus, each transverse position in the crystal contains signal created by a range of delays, rather than a single delay. This range of delays is the longitudinal smearing, δt_{PFT}.

angle, and θ is the internal crossing angle. The longitudinal smearing of a system without PFT can be obtained by setting $\alpha = 0$.

Ideally, one spatial position of the signal pulse corresponds to only one time delay without longitudinal smearing. The temporal resolution of the device under this ideal situation is limited by the pixel size of the camera. However, in a typical PG XFROG device without PFT, by a large crossing angle of 58° inside a 250 μm thick nonlinear medium yields longitudinal smearing of 450 fs which is equivalent to 1.5% of the 30 ps temporal range. Although this might be acceptable for some cases, the longitudinal smearing scales linearly with the thickness of the nonlinear medium as shown in equation 4.3 which makes the use of thick (a few mm) nonlinear medium to increase the sensitivity of the system not practical. The use of PFT helps reducing the longitudinal smearing in the system. A 50 ps temporal range is achieved by introducing PFT into the reference pulse with PFT angle $\alpha = 73°$ and crossing the reference and unknown pulses at 11°. The longitudinal smearing in this configuration is 315 fs or 0.63% of the temporal range. The amount of longitudinal smearing is greatly reduced by the introduction of PFT into reference of the PG XFROG setup.

4.3 Generation of pulse-front tilt

Pulse-front tilt can be generated by any angular dispersive elements, such as prism, diffraction grating, or etalon [104, 105]. Figure 4.3 illustrates how PFT is generated by a diffraction grating. By simple path-length consideration which the input pulse reach the bottom of the grating first and the top last, a tilted pulse-front is created. However, other spatio-temporal distortions generally exist after the pulse propagates in free spaces with angular dispersion. These unwanted distortions except for the PFT are removed by imaging the grating surface onto the target image plane. Since the amount of PFT is proportional to the angular dispersion experienced by the pulse, the PFT of the system can be simply control by using a more angularly dispersive element, for example, a grating with higher line density. A rigorous proof of this non-intuitive idea of PFT generation is given in Appendix A using the Kostenbauder matrix formulation.

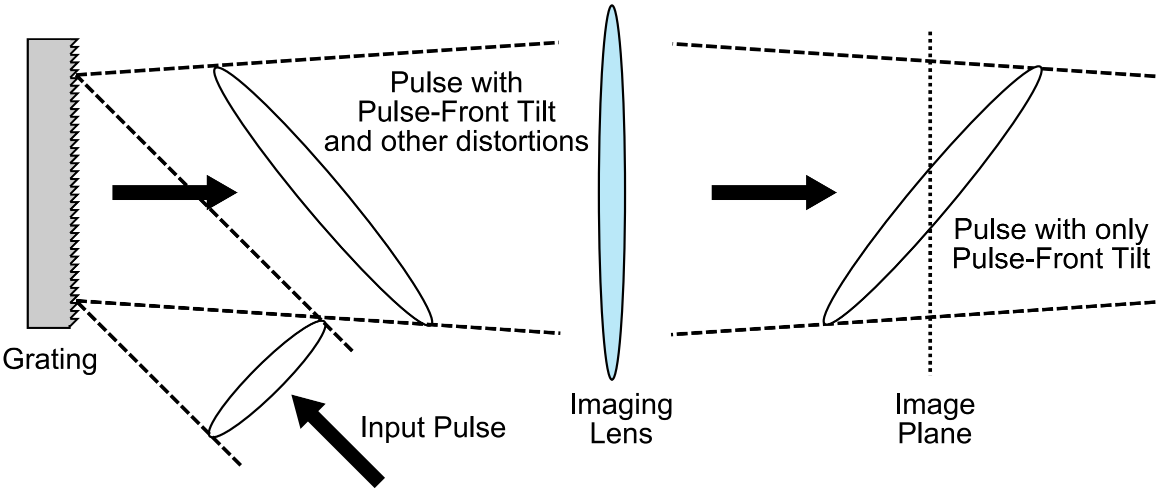

Figure 4.3: Generation of pulse-front tilt using grating and an imaging system. The angle of incident between the input pulse (without PFT) and the diffraction grating is chosen such that the first-order diffraction from the grating propagates along the normal of the grating surface. The diffracted pulse has PFT along with other spatio-temporal distortions. The surface of the grating is imaged by an imaging system to remove the spatio-temporal distortions and leaves the pulse with only PFT at the image plane.

4.4 PG XFROG with PFT experimental setup

The experimental schematic of PG XFROG with PFT in reference pulse is shown in Figure 4.4. The laser pulse from the regenerative amplifier with diameter of 8 mm was split into two replicas using an 80/20 beam splitter. The higher power pulse served

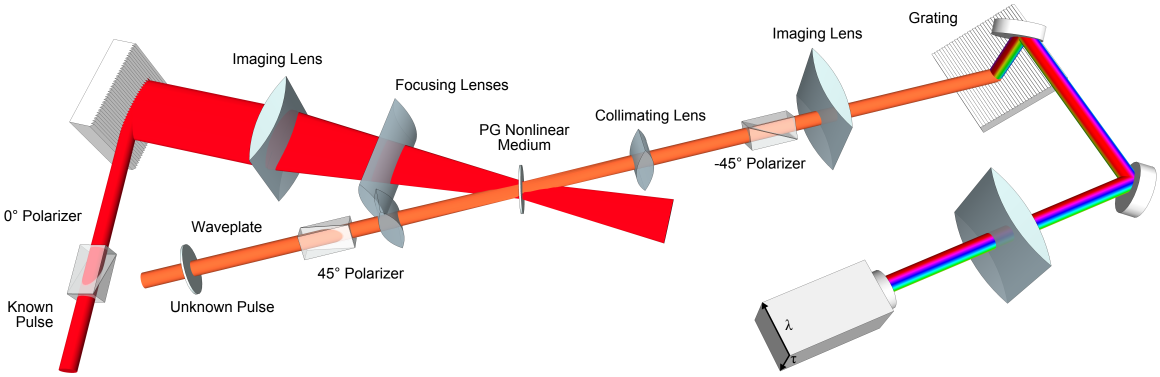

Figure 4.4: Experimental schematic for PG XFROG with PFT in reference arm. The PFT in the reference arm is generated by a diffraction grating (1200 line/mm) using an imaging system with magnification of 0.4. The PG nonlinear medium is a 250 μm thick fused silica parallel plate. The PFT angle is 73° and the external crossing angle of 11° which generate a temporal range of ∼50 ps and longitudinal smearing of 315 fs. However, due to intensity drop-off of the beam, the usable temporal range is about 30 ps. The spectrometer consists of 600 line/mm grating and a 150 mm cylindrical lens .

as the reference pulse and the low power one served as the unknown pulse. A fused silica parallel plate with thickness, L, of 250 μm was used as the nonlinear medium for PG geometry. The reference pulse, shown in red, first passed through a polarizer at 0° to increase the polarization purity before reaching a 1200 line/mm diffraction grating. This pulse impinged on the grating at a grazing incidence angle so that the first-order diffraction was diffracted along the normal of the grating surface. This is useful for the imaging condition from the grating surface to the nonlinear medium to be satisfied, as the depth of field is about 5 mm. The zeroth-order diffraction from the grating was sent to a GRENOUILLE for characterization (not shown in the schematic). Imaging of the grating was achieved using 200 mm cylindrical lens placed 700 mm away from the grating surface; it imaged the grating surface with a magnification of 0.4 onto the nonlinear medium. A 150 mm focusing lens was used to focus the beam in the vertical dimension.

The unknown pulse (lower power replica), shown in orange, passed through a waveplate, which rotated the polarization by 45°, and then a pair of crossed-polarizers at ±45°. A pair of lenses, each with a focal length of 100 mm, were used for focusing and collimating in the vertical dimension. Like a standard PG XFROG setup, the two beams crossed at an angle in the nonlinear medium to generate the signal pulse, and the nonlinear medium was imaged onto the camera to map delay to transverse position. The resultant signal from the nonlinear interaction was spectrally resolved by a spectrometer consisting of a 600 line/mm grating and a cylindrical lens with 150 mm focal length. The measured XFROG trace was retrieved using the standard XFROG algorithm.

The PFT angle α in this experimental setup was 73° and the external crossing angle, θ, was 11° . The calculated temporal range and longitudinal smearing of our experimental setup were ∼50 ps and 315 fs, respectively. However, due to the intensity drop-off at the edge of the beam, the temporal range that yielded highly accurate measurement was about 28 ps. The temporal resolution of the system was limited by the longitudinal smearing of 315 fs. This implies that any temporal structure shorter than 300 fs is washed out due to the lack of temporal resolution in the measured trace. The experimental apparatus was set up for single-shot measurement, but in the case of weak signals, one can increase the exposure time of the camera to integrate over multiple shots and perform multi-shot, but "single-camera-frame" measurements.

4.5 Result

The first set of data is a double-pulse generated by a Michelson interferometer with separation of ∼4.7 ps and chirped by 14 cm of SF11. Before tilting the pulse-front, the reference pulse was measured by a GRENOUILLE indicating a temporal FWHM of 70 fs. The energies of the reference pulse and the unknown pulse were 720 μJ and 45 μJ respectively. Due to the beam splitting and chirping, the signal pulse was too weak for true single-shot measurement, so the measured XFROG trace averaged over 5 shots on a single-camera-frame. A single-shot measurement could be performed with increased energy in the either the reference pulse or the unknown pulse.

The measured and retrieved XFROG traces (2048×2048 array), with G-error of 1.37%, are shown in Figure 4.5a and b. The temporal and spectral intensity and phase are shown in c and d. The retrieved double-pulse separation was 4770 fs with FWHM of 1700 fs. To verify our measurement, we blocked one of arm of the Michelson and measured the unknown pulse before it passed through 14 cm of SF11 by using a GRENOUILLE. The retrieved unknown pulse from GRENOUILLE was numerically propagated through 14 cm of SF11 yielding a FWHM of 1716 fs, in excellent agreement with the result from ps PG XFROG. The spectrum of the double-pulse, shown in black, was measured by a spectrometer. The double-pulse separation was calculated to be 4736 fs using the spectral fringe spacing, which agrees well with our retrieval. The retrieved pulse had a TBP of ∼89. The discrepancies between the retrieved and the calculated pulse separation and FWHM are about 1%.

Another double-pulse separated by 24 ps with TBP of ∼263 was retrieved with

G-error of 1.73%. The measured and retrieved traces are shown in Figure 4.6. The retrieved separation and FWHM were 24,400 fs and 1,780 fs respectively. The calculated FWHM is 1,772 fs in good agreement with the retrieval. The spectrometer lacked the spectral resolution to resolve the fine spectral fringes (see the black line shown in the spectral measurement of Figure 4.6). Thus, instead of using the spectral fringes, the separation was calculated from the position of the variable arm of the Michelson interferometer. The calculated separation was 24,469 fs, within 1% of the retrieved value.

4.6 Discussion

The G-error in our retrieval is relatively high for XFROG traces with array size of 2048. There are several factors that contribute to the high G-error. First, some of the polarizer leakage added to the measured trace coherently as a background. The leakage is a combination of imperfections in the polarizers and depolarization after the beam passed through the focusing and collimating lenses. This leakage background was about 8% of the peak signal strength. Since the background added partially coherently, it cannot be completely removed from the signal. Second, the signal near the wings of the trace was weak, and it falls to the background noise level, which was removed by the background subtraction (confirmed by the unusually low-noise and nearly-zero trace background). The XFROG retrieval algorithm is capable of recognizing these non-physical flaws in the measured trace and fills in the missing details to produce the retrieved trace associated with the correct pulse [107]. However, the resulting G-error will be relatively high due to the mismatch between

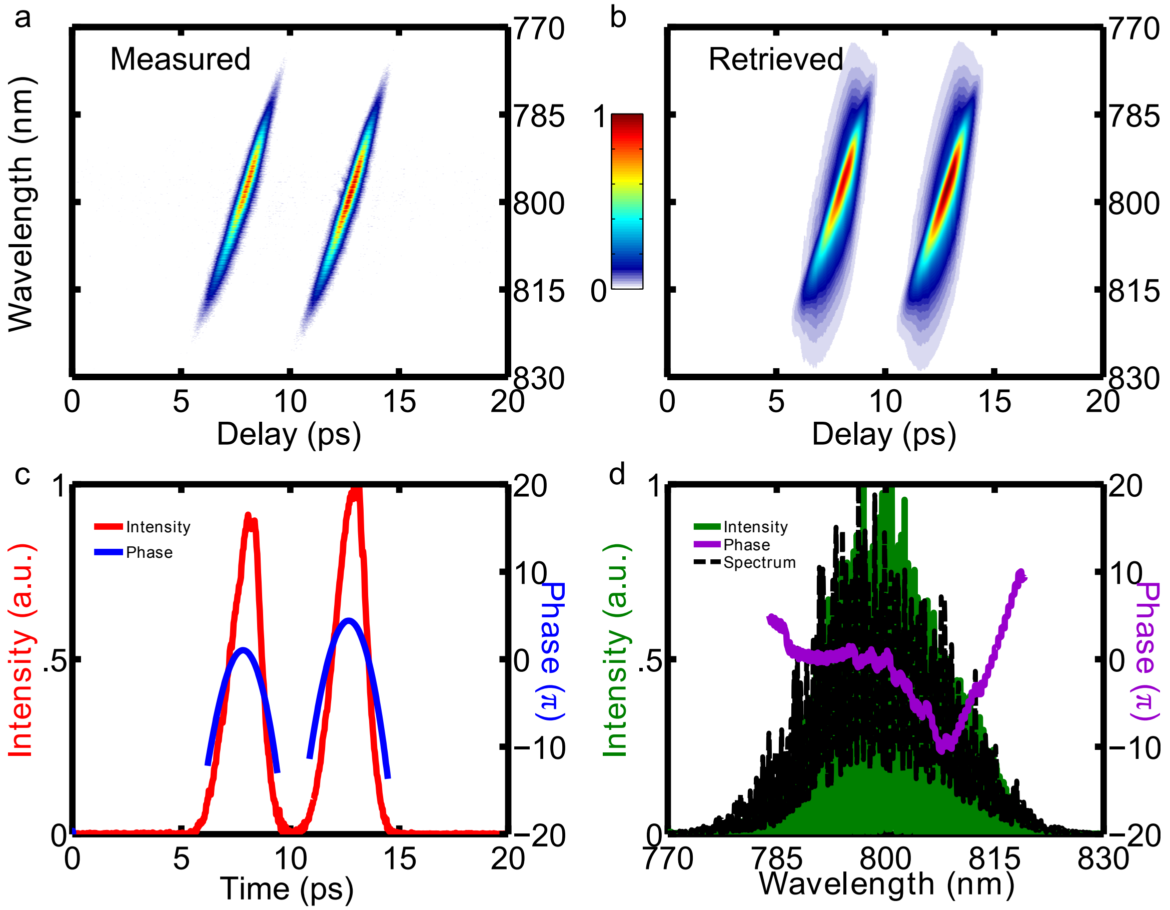

Figure 4.5: Measured (a) and retrieved (b) XFROG traces of a double-pulse with pulse separation of ∼4.7 ps with G-error of 1.37%. The retrieved temporal (c) and spectral (d) intensity and phase. The black solid line represents the spectrum measured by a spectrometer. The retrieved pulse separation was 4770 fs and the FWHM was 1700 fs.

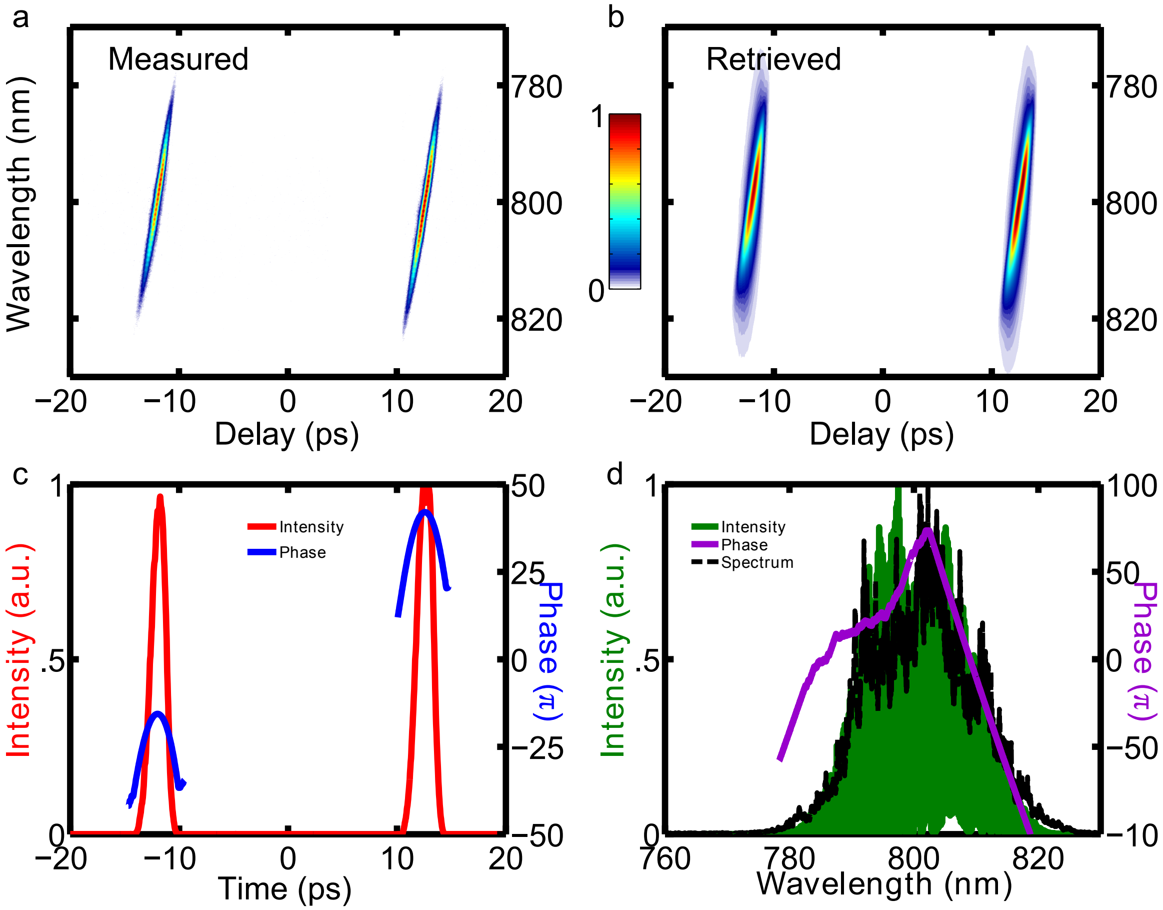

Figure 4.6: Measured (a) and retrieved (b) XFROG traces of a double-pulse with pulse separation of ∼24 ps with G-error of 1.73%. The retrieved temporal (c) and spectral (d) intensity and phase. The black solid line represents the spectrum measured by a spectrometer. The retrieved pulse separation was 24400 fs and the FWHM was 1780 fs.

the measured and retrieved traces. Finally, the measurements were made by averaging five shots from a regenerative amplifier, and the measurement could be affected by instability of this laser as discussed in Chapter 2.

There is also a discrepancy between the measured and retrieved spectra. The retrieved spectrum actually has higher spectral resolution than the experimental apparatus. In fact, the retrieval algorithm takes advantage of the redundancy in the N×N FROG trace to reproduce the detailed features of the pulse that are not measured by the apparatus [107]. Even though the grating-lens spectrometer in PG XFROG with PFT lacks the spectral resolution to measure the fine spectral fringes, the retrieval algorithm is capable of reproducing the correct spectral fringes. Indeed, the spectral fringes are too fine to be shown in the plots, and it becomes a solid green area.

The nonlinear medium used in this work was fused silica, which does not have a particularly high third-order nonlinear susceptibility. To improve the signal-to-noise ratio, one can increase the thickness of the medium (this will, however, increase the longitudinal smearing) or replace the nonlinear medium with another material with higher third-order nonlinearity, such as BK7. The signal-to-noise ratio would be improved and resulted in a reduced G-error. This could also allow a single-shot measurement which would eliminate any effects due to instability.

The advantage of using PFT to increase the temporal range of the system is that the amount of the PFT can be adjusted easily which controls the temporal range. For instance, a grating with higher line density will produce more tilt in the pulse-front and hence more temporal range at the same crossing angle. This idea can be scaled up to perform single-shot measurement of few-hundred-ps-long pulses. Combining the long temporal range achieved by introducing PFT into the reference pulse and the unlimited phase-matching bandwidth of PG geometry (discussed in Chapter 3), this setup can be used to measure complex pulses with large spectral bandwidths (more than 100 nm) and/or long temporal durations (a few ps), such as supercontinuum. The measurements of supercontinuum generated from fibers are discussed in the next chapter.

4.7 Conclusion

In this chapter, we have demonstrated the use of PFT in the reference pulse of PG XFROG to increase the temporal range of the device by more than one order of magnitude, from ∼1 ps to 28 ps, with temporal resolution of 315 fs. Pulses with very high TBP (up to 263) are measured on a single-frame by averaging over five shots due to limited energy from our regenerative amplifier. Since it is a multi-shot measurement, the result may suffer from coherent artifact. A true single-shot measurement of these pulses can be achieved by either increasing the energy of the reference or unknown pulse or increase the thickness of the nonlinear medium. The experimental configuration can be easily modified for a different temporal range by changing the grating line density. The robust XFROG retrieval algorithm is able to retrieve missing details of the pulse due to both low spectral resolution and low signal-to-noise ratio. This device is an excellent candidate to perform single-shot intensity and phase measurement of many-ps-long pulses.

CHAPTER V

SINGLE-SHOT SUPERCONTINUUM MEASUREMENT

5.1 Motivation

Supercontinuum (SC) generation is a remarkable nonlinear-optical process by which a spectrally narrow band laser pulse efficiently evolves into an extremely broadband pulse. Since its first demonstration in 1970 in bulk glass [11], many other media have been used to generate SC [12, 15, 16, 108]. Photonic crystal fiber (PCF) yields a spatially coherent SC beam [50] making SC practical for a wide range of novel applications, from stimulated emission depletion microscopy and optical coherence tomography to optical frequency metrology to carrier-envelope phase stabilization [109–112].

Interestingly, SC pulses are extremely complex and trains of them are inherently extremely unstable [113–119]. As a result, it has never been possible to completely characterize the intensity and phase of an individual SC pulse on a single-shot. Currently, single-shot techniques measure only the spectrum [118–121]. Measurements averaged over many pulses are possible (5 shots in its best-known implementation and millions in a typical implementation), but yield only a typical SC pulse at best [38,39,107,122–126]. At worst, multi-shot measurements of unstable pulse trains are susceptible to coherent artifact effects that may mislead the unwary into believing that their pulses are less complicated than they really are [43, 103]. An accurate, complete measurement of the intensity and phase of SC must be single-shot, and this remains an unsolved problem.

This problem recently acquired increased urgency when it was noted (and confirmed) that SC can give rise to optical rogue waves that are mathematically equivalent to oceanic rogue waves that sink dozens of ships every year [127]. Indeed, numerical simulations and experimental observations of their single-shot spectra have confirmed that SC generation in PCF follows the same L-shaped statistics as oceanic waves, allowing statistically rare rogue events to occur much more often than would be implied by simple Gaussian statistics [127,128]. Consequently, improved understanding of optical rogue waves could lead to insight into and eventually to the prediction and suppression their oceanic counterparts [129,130].

While the measurement of an oceanic rogue wave is straightforward, its intentional generation is difficult and probably ill-advised (unless on a very small scale). On the other hand, the generation of an optical rogue wave is simple, routine, and safe, but its single-shot intensity-and-phase measurement has not been possible. Thus, experimental studies of optical rogue waves have been limited to study of its spectrum, which yield only limited insight into their nature. Therefore, single-shot intensity-and-phase measurement of an optical rogue wave is important.

In this chapter, we demonstrate the use of XFROG with titled reference pulse to measurement the intensity and phase of SC on a single-shot. Similar to setup described in Chapter 4, we incorporate significant PFT in the reference pulse to achieve the large necessary temporal range. In addition, we overcome the temporal-resolution limitation in such measurements by showing that the correct combination of beam crossing angle and reference-pulse tilt cancels out the longitudinal smearing. This also allows us to use a thick nonlinear medium, considerably increasing sensitivity and allowing single-shot measurement. Using this device, we completely measure for the first time an individual SC pulse.

5.2 Supercontinuum generation and optical rogue wave

Supercontinuum generation has been studied for more than 40 years since its first demonstration. Over the years, possibility of SC generation using different material, such as glasses, liquids, gases and different kinds of waveguide has been investigated. The development of PCF in the late 1990s brought a huge break-through in SC generation by using PCF as the generation medium [50]. PCF has enhanced modal confinement and nonlinearity compared with index-guide fiber, more importantly, its ability to tailor-make the dispersion relation and the zero-dispersion wavelength (ZDW) allows optimization for SC generation with laser source that is easily accessible. ZDW is an important parameter in SC generation which governs nonlinear interactions that generate new wavelengths. SC generations by standard laser systems such as Ti:sapphire laser (800 nm) and telecommunication laser (1550 nm) are made possible by choosing the ZDW of the fiber close the center wavelength of the laser [38, 121]. After 10 years of research, PCF is now a commercial off-the-shelf product which offers a great variety of the ZDW.

Numerous researches were performed to investigate the coherence, generation mechanism and relation between the seed pulse and output of SC generation, however, these details are out of the scope of this work, so please refer to the excellent review works done by Dudley *et al.* and Alfano for more information of SC generation and its numerical simulation [13,108]. In numerical simulations, SC generation in PCF is usually modeled by the generalized nonlinear Schrödinger equation (GNLSE) which, coincidentally, is also the modeling equation for oceanic waves [13,131]. Solli *et al.* proposed and demonstrated the connection between the oceanic rogue wave and optical rogue wave in 2007 [127]. The observation of optical rogue wave in the original work was performed by wavelength-to-time stretching technique which introduced a large amount of GDD into the pulse by using dispersive fiber and measured the time signal by a fast detector and scope. This allowed a single-shot spectral measurement of individual SC which confirmed the SC generated from PCF followed the L-shape statistics. This measurement technique is useful to measure the statistical behavior of SC, but the phase information of individual SC is missing and thus cannot be used to investigate the exact behavior of the optical rogue wave. A complete measurement of optical rogue wave on a single-shot could possibly lead to a better understanding of its oceanic counterpart.

5.3 Challenges in supercontinuum measurement

Typical SC generated from PCF is a few ps long and has more than 100 nm of spectral bandwidth, yielding a difficult-to-measure time-bandwidth product of ∼100 or more. In other words, SC pulses are extremely complex, with fine structure in both the temporal and the spectral domains. Worse, due to the small cores of PCF, the SC pulse has energy of at most ∼10 nJ.

In order to deal with the low energy of the SC pulse, previously measurement employed the XFROG technique in which a higher-energy, known reference pulse gates the SC, rather than the SC gating itself. It would be helpful to also use a long nonlinear medium to increase interaction length and therefore signal strength. However, phase-matching bandwidth constraints typically prevent this. For example, due to energy concerns, previous measurements used sum-frequency generation (SFG, a second-order nonlinear optical process) as the gating mechanism which typically generates more energy in the signal pulse than other higher-order processes. Unfortunately, SFG has a limited phase-matching bandwidth which requires a very thin (tens of microns) nonlinear medium to measure broadband pulses. Even with the thin medium, it was not enough to cover the entire bandwidth of the SC, and thus the medium was angle-dithered over many shots to match the whole bandwidth [38, 39, 107, 122, 125]. This trade-off between phase-matching bandwidth and signal strength makes measuring SC very difficult, especially on a single shot. Another attempt used a transient-grating (TG) geometry in XFROG for a single-shot measurement [123]. This setup measured the SC generated from bulk glass by averaging over 5-shots to increase the signal-to-noise ratio, but, like other attempts, had a phase-matching constraint which cannot be easily generalized for extreme broadband SC. In addition, the sensitivity of the setup was limited at μJ level which is two orders of magnitude higher than SC generated from PCF.

In this work, we consider SCs extreme spectral width first and so chose to use a PG geometry, which has essentially infinite phase-matching bandwidth and so nicely solves the spectral-width problem immediately. Unfortunately, PG geometry is a significantly weaker third-order nonlinear process and so seems to be a counter-intuitive choice in view of the weak pulse energy of SC. This means that getting adequate signal energy will be highly dependent on the length of nonlinear medium that we can use. The length of the medium is not limited by bandwidth concerns for PG geometry, but, in general, it will be limited by temporal resolution concerns. This raises another problematic trade-off that exists between temporal range and temporal resolution. A typical FROG or XFROG device achieves single-shot measurement by crossing the reference pulse and the unknown pulse inside the nonlinear medium at an angle, θ, as discussed in Chapter 1.2.4. This maps delay onto transverse spatial position in the nonlinear medium and also at the camera onto which the nonlinear medium is imaged. The temporal range of the device scales with the crossing angle, and delay ranges of up to a few ps are achievable in this manner, but delays of several pulse lengths are necessary for complete measurement. Worse, the temporal resolution is limited by the amount of longitudinal geometric smearing, as discussed in Chapter 4. As a result, both the temporal range and resolution of typical measurement devices are insufficient for SC measurement.

A way to increase the temporal range of FROG device is to introduce PFT to the pulse(s), as discussed in Chapter 4.2. We also adapt this approach here for PG XFROG and add PFT to the reference pulse. The temporal range, with and without PFT are given by equation 4.1 and 4.2. This solves the temporal-range problem, but longitudinal geometrical smearing still limits the temporal resolution. It scales with nonlinear-medium thickness and has not been possible to eliminate and thus limit the thickness of the nonlinear medium used in previous research [123]. The longitudinal smearing in the system with PFT δt_{PFT} is given by, equation 4.3:

$$\delta t_{PFT} = \frac{L}{c}\left(1 - \frac{\cos\alpha}{\cos(\alpha - \theta)}\right)$$

where L is the thickness of the nonlinear medium, α is the pulse-front tilt angle, θ is the internal crossing angle, and c is the speed of light. On a closer look at the equation, we find two conditions that can eliminate the longitudinal smearing. The first one is $\theta = 0$, which is obvious because the reference and unknown pulses are co-propagating, and thus there will be no drifting in the spatial positions as they propagate. However, this condition is not practical in the experiment as the co-propagating pulses cannot be separated after their interaction inside the nonlinear medium. The second one is $\theta = 2\alpha$, this condition is counter-intuitive as in normal single-shot geometry, the large crossing angle is the reason behind the undesired longitudinal smearing. An illustration depicts this condition is shown in Figure 5.1. The reference pulse gates only the center (green) part of the unknown pulse as the two pulses propagate through the nonlinear medium. This confirms that the condition $\theta = 2\alpha$ removes the longitudinal smearing completely. In addition to achieving high temporal resolution, elimination of the longitudinal smearing in the device allows the use of a much thicker nonlinear medium, which increases the interaction length, and thus increases the sensitivity of the device. This allows our experimental setup to measure extremely weak SC at ∼10 nJ level on a single-shot.

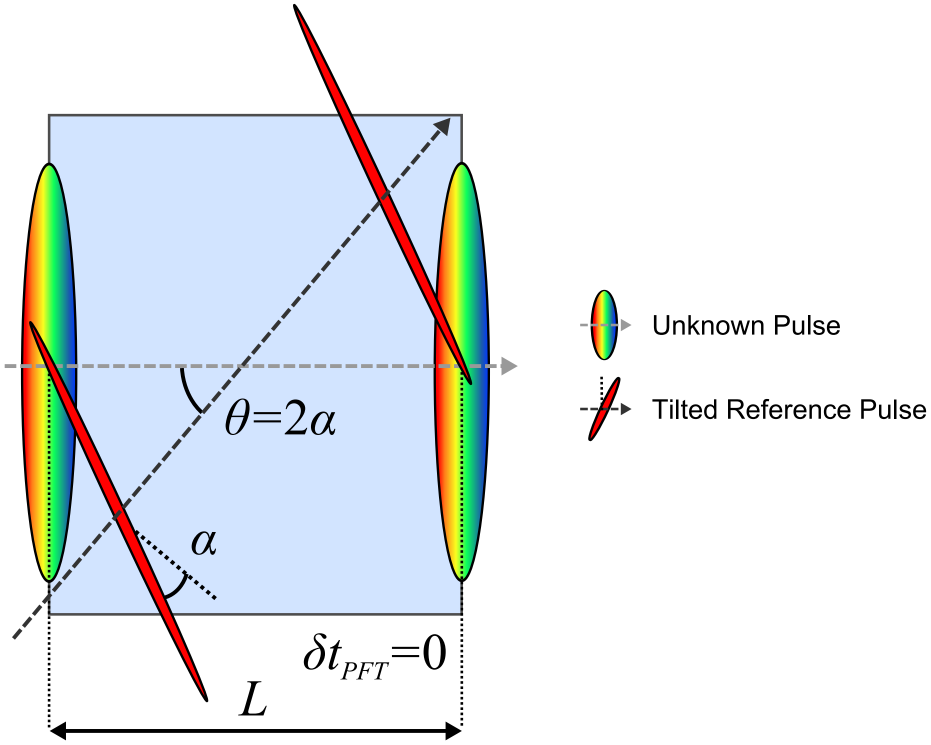

Figure 5.1: Illustration of canceling longitudinal smearing in single-shot XFROG by choosing a correct relation between the PFT and internal crossing angle. The ideal choice of internal crossing angle, $\theta = 2\alpha$, removes the longitudinal smearing completely while maintaining a large delay range. The reference pulse overlaps with the same part of the unknown pulse throughout the nonlinear medium. The tilt angle α here remains the same as in Figure 4.2.

5.4 Experimental setup

The experimental schematic is depicted in Figure 5.2. The laser source used in this work is the regenerative amplifier. The amplifier output pulse was split into two replicas by a 20/80 beam splitter. The lower energy pulse, which served as the seed pulse for the SC, was spectrally filtered by a band-pass filter centered at 785 nm with FWHM of 6.5 nm. It was spatially filtered by lens-pinhole-lens setup for better spatial coherence (not shown in Figure 5.2). It was then chirped by SF11 glass before being focused into a PCF by a 5X microscope objective (Newport) to generate SC. The seed pulse energy was attenuated by ND filters and its polarization

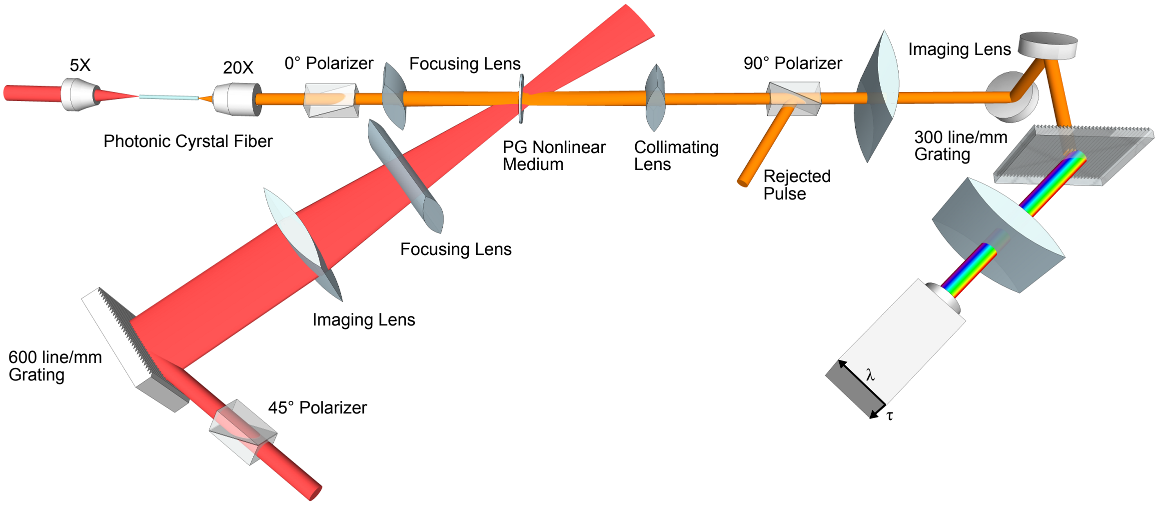

Figure 5.2: Experimental schematic of PG XFROG with PFT in the reference pulse for supercontinuum measurement. The red and orange represent the reference pulse and the supercontinuum respectively. The PG nonlinear medium (5 mm thick BK7 parallel plate) is imaged onto the camera in the vertical direction - mapping time delay to spatial position. The spectrometer consists of a 300 line/mm transmission grating and a 75 mm cylindrical lens that generate the spectrum of the signal in the horizontal direction. The PFT angle α and the external crossing angle are $\sim 15°$ and $43°$ respectively. This is chosen such that the internal crossing angle θ satisfies the relation $\theta = 2\alpha$ to cancel out the longitudinal smearing.

was controlled by a half-wave plate. The output SC was collimated by a 20X (or 5X, depending on the fiber) microscope objective. The input energy, bandwidth, chirp and polarization of the seed pulse controlled the average output bandwidth and temporal profile of the SC. The spatial profile of the SC was measured by a camera to confirm its uniformity. A fiber-coupled spectrometer was used to confirm the absence of spatial chirp in the SC. The output SC was not polarized, but dependence between the seed pulse polarization and the output bandwidth of SC was observed.

The higher energy pulse from the beam splitter was sent to a 600 line/mm diffraction grating to generate PFT and served as the reference pulse. The surface of the diffraction grating was imaged onto the nonlinear medium by a 200 mm cylindrical lens placed 400 mm away from the grating surface. The resulting reference pulse had a pulse-front tilt angle, α, of ∼15° . The nonlinear medium was a 5 mm thick BK7 parallel plate. A flip-mirror was placed before the diffraction grating (not shown in Figure 5.2) to direct the reference pulse to a GRENOUILLE for a measurement of its intensity and phase.

The SC and reference pulse passed through a 0° and 45° polarizer respectively before crossing inside the nonlinear medium. The SC was focused onto the nonlinear medium by a 100 mm cylindrical lens and the reference pulse was focused by a 300 mm cylindrical lens. The SC and the reference pulse crossed externally at 43° to satisfy the required internal crossing angle condition, $\theta = 2\alpha$. Like a regular PG XFROG, when overlapped spatially and temporally, optically induced birefringence caused by the intense reference pulse rotated the polarization of the SC. This rotated portion of SC became the signal of PG XFROG. The rotated SC pulse passed through the cross-polarizer at 90° while the unrotated portion was rejected and recycled for the same-shot spectrum (not shown in the schematic, see discussion for more details). The nonlinear medium was imaged onto a grating-lens-camera spectrometer by a 300 mm cylindrical lens placed 600 mm away from the nonlinear medium.

The XFROG trace was generated on a single-shot with the vertical direction serving as the time-delay axis and the horizontal direction as the spectral axis. A 300 line/mm transmission grating and a 75 mm cylindrical lens were used to construct the spectrometer. The spectrum of the rejected pulse from the 90° polarizer was measured by the same grating-lens spectrometer. The spectrum of the rejected pulse and signal XFROG trace were recorded by the camera in the same frame on the same shot. The experimental apparatus had a temporal range of ~8 ps and spectral range of ~360 nm. Fourier filtering and standard background subtraction were performed before retrieving the intensity and phase by the standard XFROG algorithm.

5.5 Result

In this work, SC generated from two different types of fibers were investigated, they were PCF and single mode fiber (SMF). The PCF is NL-2.8-850 (Thorlabs) which has a ZDW at 850 nm. The SMF is F-SA (Newport) which is design for single-mode operation at 488 nm. In both cases, the SC were measured by the same apparatus as discussed in the previous section. Due to different core diameters of the fibers, a 5X objective was used in the SMF case (instead of 20X for PCF) to collimate the output SC. Unlike SC generation in bulk material which involves complex spatial and temporal effect to generate the broad spectrum, typical optical fiber generated SC exhibits single spatial mode [123]. The spatial profile of the SC output measured by camera is shown in Figure 5.3. Figure 5.3a was recorded by placing the camera in the beam path and Figure 5.3b was captured by taking a picture of the SC on a piece of paper. Both of them show good spatial coherence. In addition, no spatial chirp was found by sampling the spectrum of the SC at different spatial locations using a fiber-coupled spectrometer.

5.5.1 Supercontinuum generated from photonic crystal fiber

Two different SC were generated by the PCF under different experimental conditions using the PCF. The first SC was generated by a 23.0 mm long fiber with a seed pulse which was chirped by 12 cm of SF11 glass and had pulse energy of 190 nJ. The

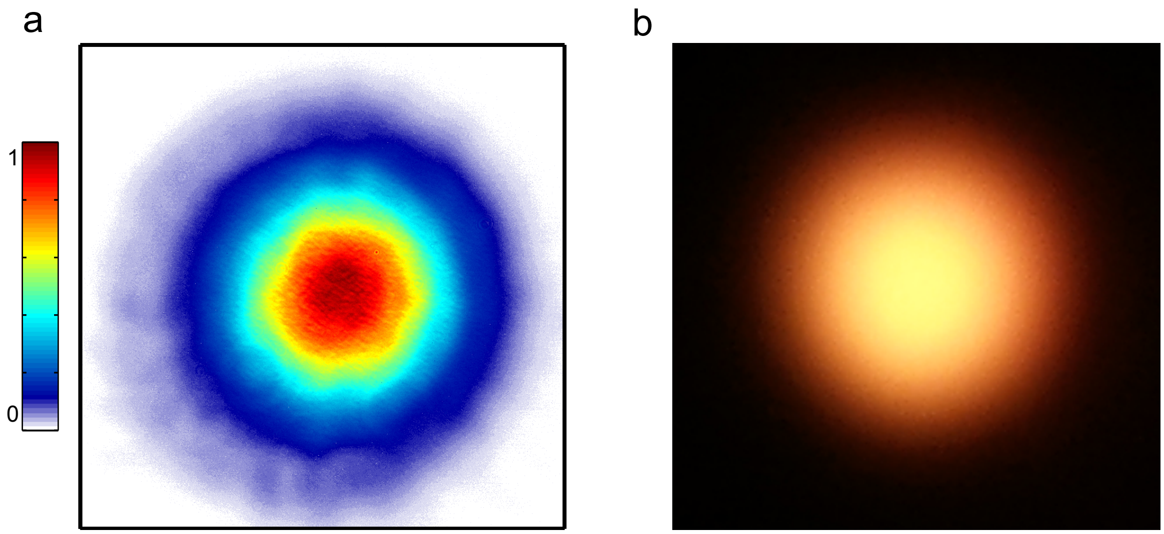

Figure 5.3: Spatial profile of SC generated from NL-850-2.8 PCF. (a) Recorded directly by sending the beam to the camera. (b) Recorded by taking a picture of the spatial profile on a piece of white paper. The Gaussian shape spatial profile confirms the SC output is single-mode.

resultant SC had 15.5 nJ immediately after the 20X collimating objective and 7.3 nJ was delivered to the nonlinear medium. The measured and retrieved FROG traces (2048×2048 array), with G-error of 0.85%, are shown in Figure 5.4a and b. The retrieved temporal and spectral intensity and phase are shown in c and d. The majority of the measured features are reproduced in the retrieved trace, while the noisy background is ignored by the XFROG retrieval algorithm. The retrieved spectrum (green solid line) ranged from 715 nm to 850 nm, showing an excellent agreement with the same-shot spectrum (black dashed line). The same-shot spectrum was an independently measured spectrum from the same SC as measured by our apparatus. The retrieved spectral peak locations also match well with the measured ones. The duration of the pulse is ∼2 ps. with TBP ∼65. This is, to the best of our knowledge, the first single-shot intensity and phase measurement of SC generated from PCF.

The second SC was generated by a 32.2 mm long fiber with a seed pulse which was

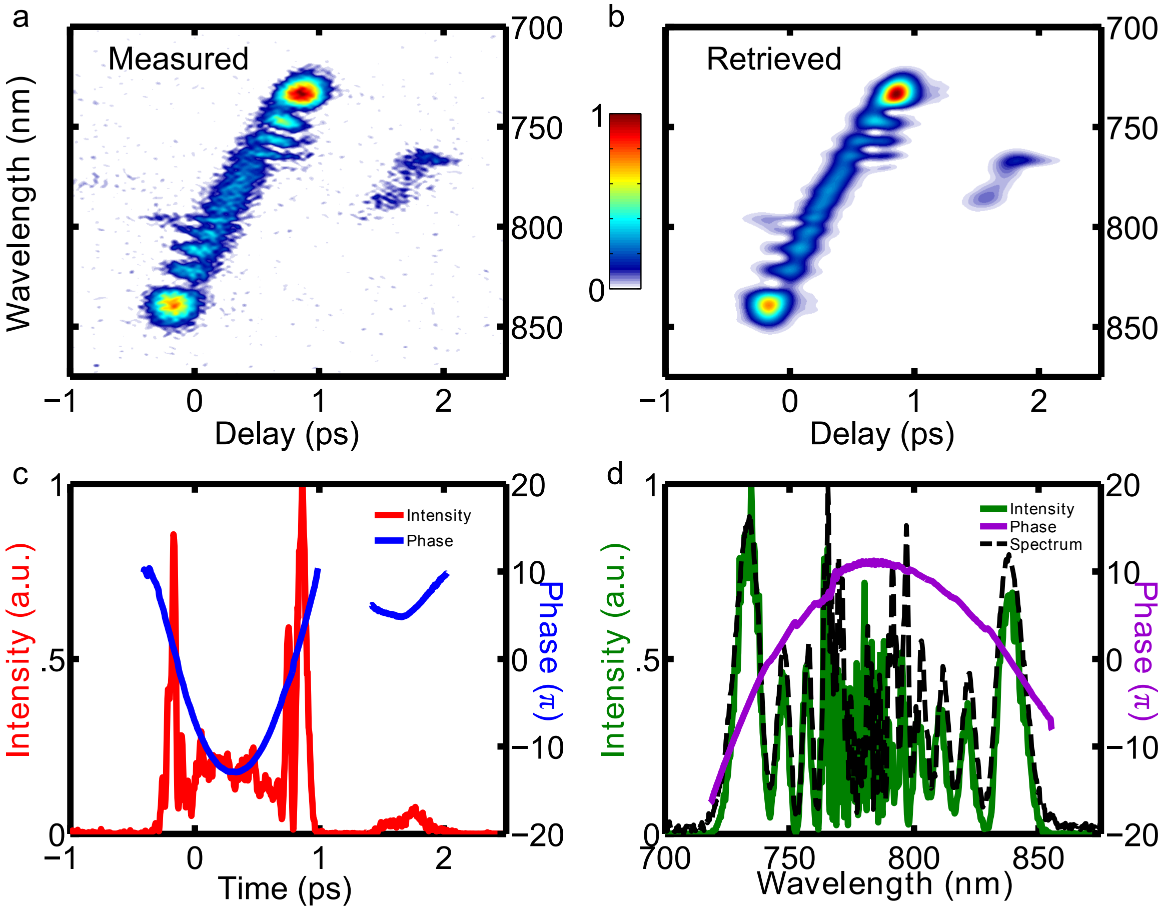

Figure 5.4: Single-shot PG XFROG measurement of supercontinuum generated from 23.0 mm long NL-2.8-850 PCF. (a) Measured FROG trace (2048×2048 array) after background subtraction. (b) Retrieved FROG trace with G-error of 0.85%. (c) Temporal intensity (red) and phase (blue) of the retrieved supercontinuum. (d) Spectral intensity (green) and phase (violet) of the retrieved supercontinuum with the same-shot spectrum (black).

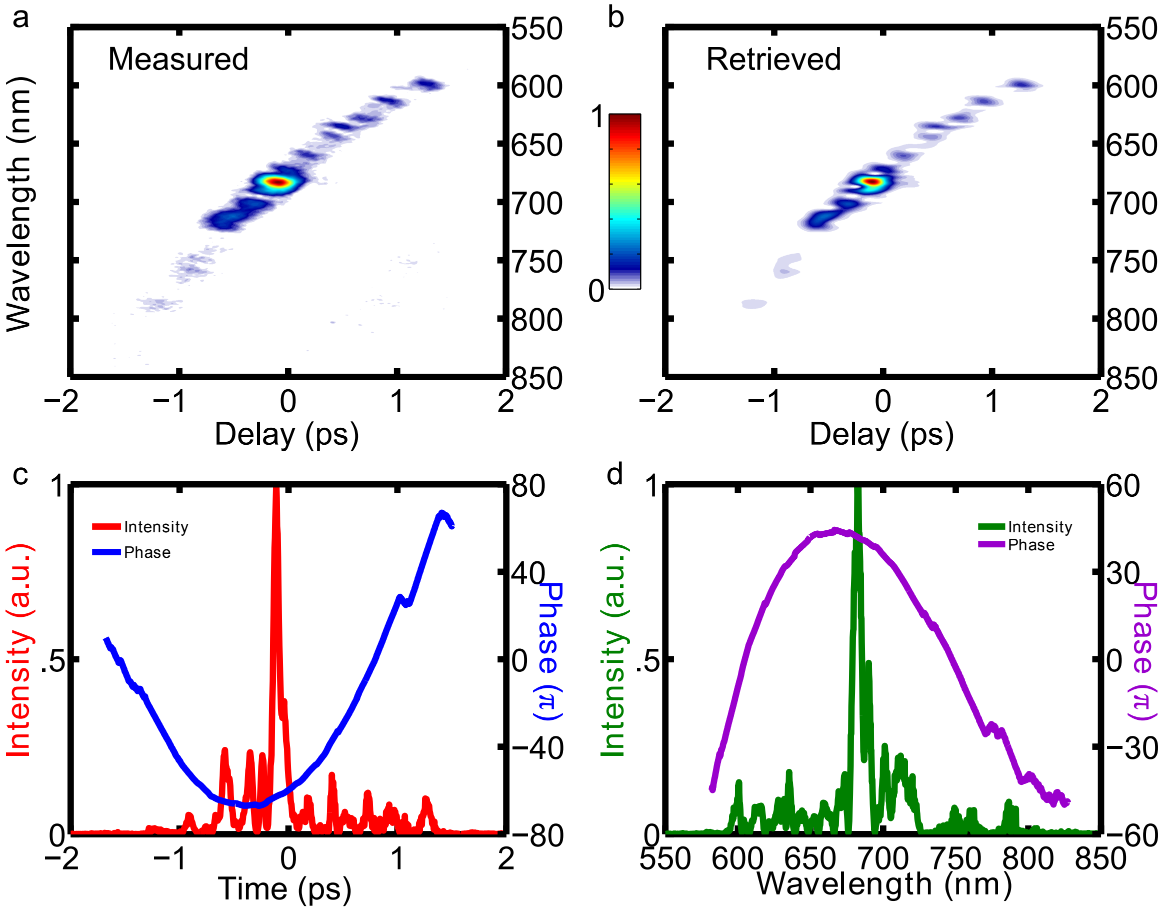

Figure 5.5: Single-shot PG XFROG measurement of supercontinuum generated from 32.2 mm long NL-2.8-850 PCF. (a) Measured FROG trace (2048×2048 array) after background subtraction. (b) Retrieved FROG trace with G-error of 0.57%. (c) Temporal intensity (red) and phase (blue) of the retrieved supercontinuum. (d) Spectral intensity (green) and phase (violet) of the retrieved supercontinuum.

chirped by 8 cm of SF11 glass and had pulse energy of 200 nJ. The output SC had longer temporal duration, broader spectral bandwidth and less pulse energy compared with the first set of SC. The pulse energy was 13.0 nJ after the objective and 6.5 nJ was delivered to the nonlinear medium. The measured and retrieved FROG traces (2048×2048 array), with G-error of 0.57%, are shown in Figure 5.5a and b. The retrieved temporal and spectral intensity and phase are shown in c and d. A more aggressive background subtraction was used to clean up the measured FROG trace because of the lower energy in the SC. The retrieved pulse has a TBP of ~96 with duration of ~2.5 ps and spectrum ranging from 590 nm to 800 nm. The broader spectrum is not surprising as the seed is less chirped and hence has a higher peak intensity which, in general, generates SC with a larger bandwidth. The temporal and spectral phase from Figure 5.5c and d show more quadratic phase in the output, which is expected because the bandwidth is larger and the fiber is longer. The same-shot spectrum was not measured as the previous measurement demonstrated the validity of this measurement technique.

5.5.2 Supercontinuum generated from single mode fiber

The SMF used in this work was F-SA which had a length of 43.3 mm. The seed pulse had energy of 180 nJ and was chirped by 8 cm of SF11 glass. The output SC had 68 nJ immediately after the 5X objective and 34 nJ was delivered to the nonlinear medium. The spatial profile of the SC is shown in Figure 5.6. The Gaussian shape profile confirmed that no higher-order modes were excited. The measured and retrieved FROG traces (2048×2048 array), with G-error of 0.67%, are shown in Figure 5.7a

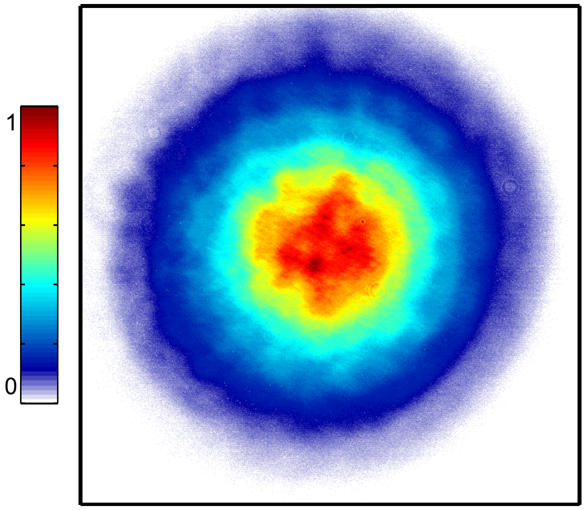

Figure 5.6: Spatial profile of SC generated from F-SA SMF. The Gaussian shape profile confirms that no higher-order modes are excited in the fiber.

and b. The retrieved temporal and spectral intensity and phase are shown in c and d. The output SC spectrum ranged from 670 nm to 850 nm which is well above cut-off wavelength guaranteeing single mode operation. The retrieved pulse has a TBP of ~51 with duration of ~2.5 ps and spectrum ranging from 670 nm to 850 nm.

5.6 Discussion

It is important to confirm that our retrieved pulse is correct, but, there is no alternative technique available to confirm it. The best that can be done is to compare the spectrum measured by our device with the one measured by using a standard spectrometer. However, SC generation is an inherently unstable process and suffers from severe shot-to-shot fluctuations, especially in its spectrum. A spectrum measured from a different pulse will be different and thus cannot be used as a direct comparison with the XFROG measurement. As a result, the only spectrum that can be used to confirm the measurement has to come from the exact same SC pulse

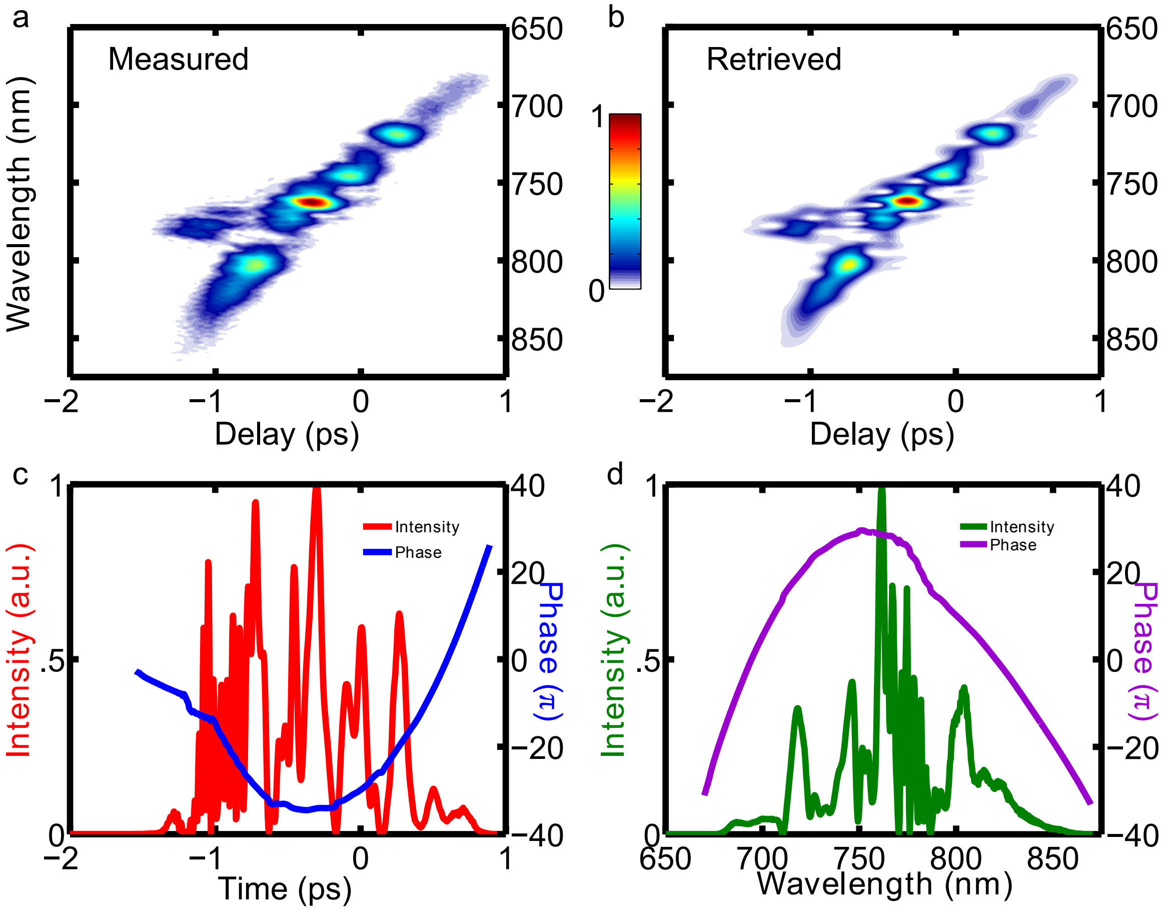

Figure 5.7: Single-shot PG XFROG measurement of supercontinuum generated from 43.3 mm long F-SA SMF. (a) Measured FROG trace (2048×2048 array) after background subtraction. (b) Retrieved FROG trace with G-error of 0.57%. (c) Temporal intensity (red) and phase (blue) of the retrieved supercontinuum. (d) Spectral intensity (green) and phase (violet) of the retrieved supercontinuum.

as that measured by the XFROG. Since the SC pulse is extremely weak, sending a sufficient amount of the SC pulse to a spectrometer before the nonlinear medium would greatly reduce the signal strength. Likewise, splitting part of the beam to a spectrometer after the nonlinear medium is also undesirable. Fortunately, in the PG geometry, the signal pulse is generated when the reference pulse slightly rotates the polarization of the SC pulse, which is then passed through a polarization analyzer that rejects the original unrotated polarization of the SC pulse. Thus the spectrum of the analyzer-rejected portion of the SC can be independently measured and hence used to confirm the XFROG-measured spectrum on the same shot. This rejected pulse was directed to pass through the same grating-lens spectrometer as used for the PG XFROG setup to minimize calibration issues. However, as the beam path is slightly different from the signal path, an independent calibration was made for this same-shot spectrum.

When comparing the retrieved spectrum with the same-shot spectrum in Figure 5.4d, we see that the spectral peaks match well at the edges of the spectrum, but there are some small discrepancies in the central region. During the experiment, we found that a small pre-pulse was ejected from our regenerative amplifier tens of ps before the main pulse. Due to its much lower energy, the pre-pulse experienced only slight spectral broadening in the PCF and contributed to the spectrum from 760 nm to 800 nm, with a FWHM of 15nm. As FROG is a time-gated device, and the pre-pulse precedes the gating reference pulse by many ps, the pre-pulse does not affect the recorded FROG trace. A spectrometer, however, integrates over all the energy that impinges onto the sensor during its exposure time. Thus, the same-shot spectrum is affected by a pre-pulse while the FROG measurement is not. A correction to the spectrum was made by first capturing a FROG trace of the pre-pulse at the correct delay, determining its spectrum, and then subtracting its spectrum from the same-shot spectrum. This assumes incoherent addition of the pre-pulse spectrum and the SC spectrum, which is not precisely accurate. We believe that this accounts for the discrepancies in the central region of the spectrum.

Note that there is a small pulse separated with the main pulse by about 1 ps in Figure 5.4a. We attribute this small pulse to higher-order modes of the PCF. Typically higher-order modes have different group velocities compared with the fundamental mode, which result in walk-off from the main pulse. Even though a Gaussian-like spatial profile is observed by camera, the higher-order modes are weak compared with the fundamental mode and thus may fall below the detection threshold.

Both the XFROG traces generated from PCF and SMF have similar slopes, from bottom left to top right, which correspond to normal dispersions. No change of slope of the XFROG traces is observed which means the output spectra of the SC are contained inside the normal dispersion regime. The dispersions of the two fibers used in the experiment are shown in Figure 5.8. The ZDW of the PCF is located at 850 nm implying that normal dispersion should be observed for wavelength less than 850 nm. Only part of the dispersion curve of the SMF is provided by the manufacturer, ranged from 450 nm to 800 nm, but from the trend of the dispersion, the fiber should still have normal dispersion from 800 nm to 850 nm. The experimental observations are consistent with the dispersion properties of the fibers.

Output SC bandwidth dependence on seed pulse polarization was observed during

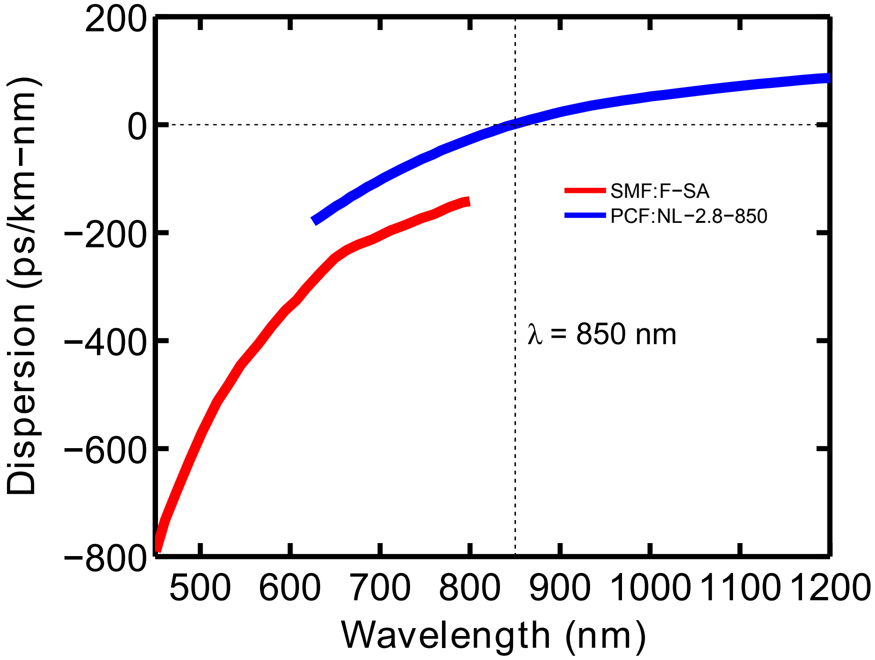

Figure 5.8: Dispersion relation of fibers provided by manufacturer. The single mode fiber is shown in red and the photonic crystal fiber is shown in blue. The intersection between the horizontal and vertical dash-line is the zero dispersion wavelength for the photonic crystal fiber, located at 850 nm.

the experiment. Figure 5.9 shows some typical measured XFROG traces with the different polarizations of the seed pulse. The polarization was rotated by a half-wave plate and each output was recorded at different polarization. The polarization dependence effect was reported and investigated by different groups of researchers [13,132,133]. It is attributed to the imperfection of the fiber during its manufacturing process which breaks the rotational symmetry and introduces birefringence to the fiber.

5.7 Future works

In order to capture optical rogue wave, the spectral and temporal range of the rogue event should be roughly known such that an appropriate change to the experimental apparatus can be made. In fact, the experimental setup presented in this work is easily

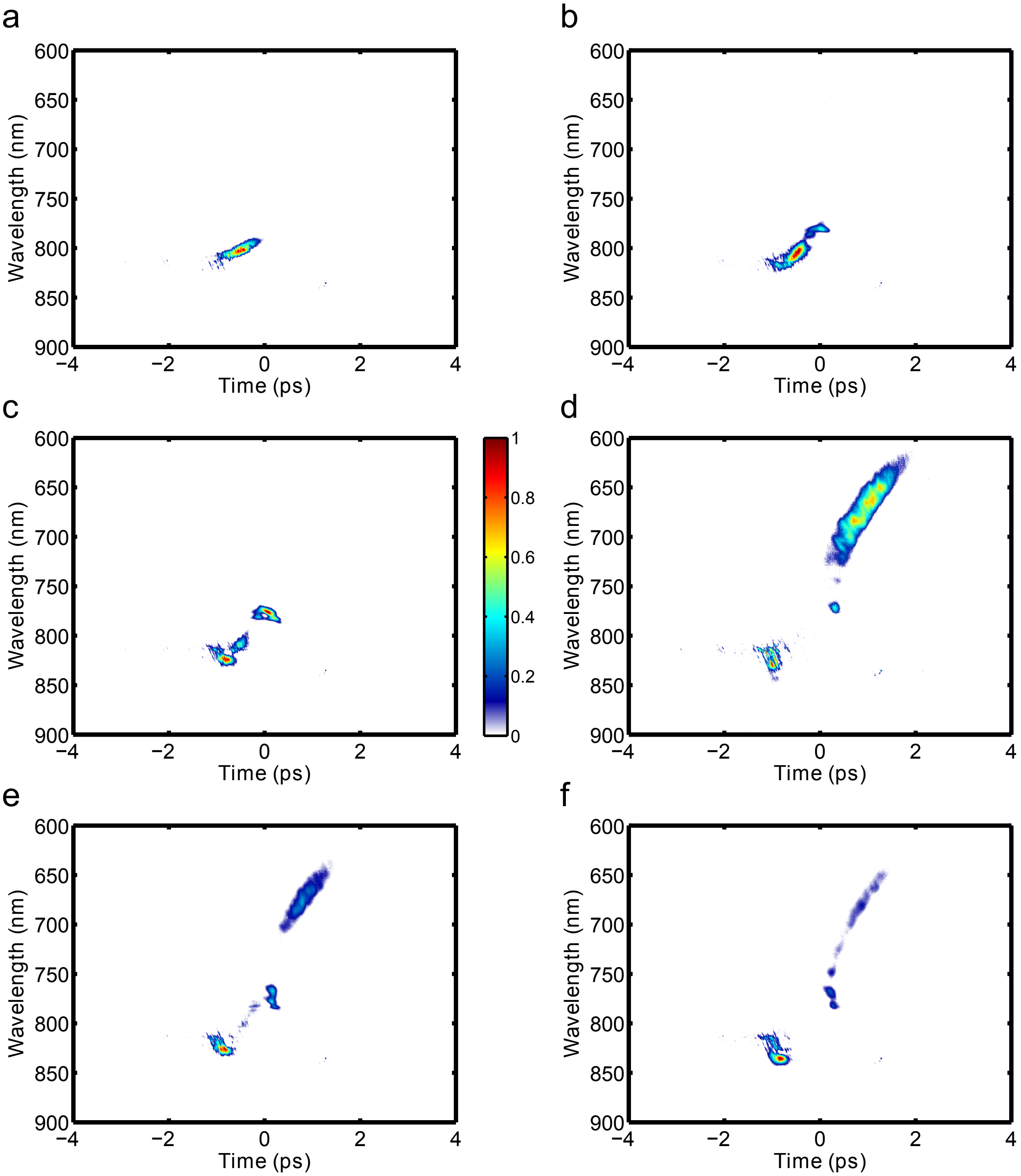

Figure 5.9: PG XFROG traces of SC with different seed polarizations. The polarization of the seed pulse in each case is controlled the rotation of a half-wave plate.

able to adapt to the requirements imposed by the already found optical rogue waves. For example, the optical rogue waves identified by Solli *et al.* require a temporal range of ∼6 ps and spectral bandwidth of ∼300 nm centered at 1064nm [127]. The

PG XFROG apparatus presented in this work can be used to measure such a optical rogue wave with minor modifications. First, all the mirrors should be replaced by NIR broadband dielectric mirrors. Second, a new diffraction grating blazed for 1064 nm should be used for better efficiency. Finally, cylindrical-parabolic mirrors should be used to avoid GDD introduced by the lenses. The nonlinear medium can be kept as BK7 because it is transparent for the visible and NIR spectrum. Also, the PFT in the reference pulse and the crossing angle can remain unchanged. However, in the original work of optical rogue wave, the pulse energy of the SC was at the 10 pJ level. The current experimental setup has sensitivity of nJ level meaning that the pulse energy of the optical rogue wave has to be increased to nJ before the measurement is possible.

The output SC from the fibers used in our work were not polarized which made PG geometry not as efficient as it should be, because almost half of the SC pulse energy was rejected at the first polarizer in the setup. The system can be optimized by using polarization maintaining fibers as the SC generating fibers. This allows a polarized SC output which lower the sensitivity threshold of the system by rough half. The polarized SC output from polarization maintaining PCF could play a significant role in SC and optical rogue wave measurements as all of the SC pulse energy will be useful in the measurements leading to better signal-to-noise ratio. With the rapid advancements in PCF design and manufacturing, the generation of polarized nJ optical rogue wave should be realizable in near future. Our experimental setup would be the best candidate to perform a complete intensity and phase measurement of optical rogue wave.

5.8 Conclusion

To summarize, we have proposed and demonstrated the use of PFT in the reference arm of PG XFROG to measure intensity and phase of SC generated from PCF and SMF on a single-shot. Unlimited phase-matching bandwidth of PG geometry solves the limited phase-matching bandwidth issues which previously required angle-dithering (and hence, multi-shots) to perform the measurement. PFT in the reference pulse increases the temporal range of the single-shot PG XFROG. More importantly, controlling the internal crossing angle between the tilted reference pulse and the SC inside the nonlinear medium eliminates the longitudinal smearing completely and allows the use of a nonlinear medium an order of magnitude thicker to achieve nJ sensitivity in our device. This is, to the best of our knowledge, the first single-shot intensity and phase measurement of SC. The experimental apparatus can be easily modified to measure optical rogue wave provided its pulse energy reaches nJ level.

APPENDIX A

KOSTENBAUDER FORMULISM

This chapter gives a brief introduction to Kostenbauder formulation which is used to model pulses propagate through different optical elements. A general Kostenbauder matrix (K-matrix) can represent all essential optical elements, such as lenses, gratings, mirrors and free space propagations. It is based on the ray-matrix or ABCD-matrix formulation which takes the pulse properties, including bandwidth and dispersion, into account. Like ABCD-matrix, the K-matrix for a series of optical elements is given by the matrix product of the individual K-matrices in the same order in which the elements are encountered by the pulse.

In addition to the two coordinates that used to model the ray vector in ABCD matrix, x and θ, the K-matrix formulation, use a ray-pulse vector that has four coordinates: x, θ, t, and f, representing position, slope, time and frequency respectively. The coordinates are measured on the reference planes erected perpendicular to the reference axis at arbitrary locations, usually just before and after the optical devices as shown in Figure A.1. Unlike the reference axis is in standard ABCD-matrix approach is taken to be optical axis of the optical system, the reference axis in K-matrix formulation is defined as the path taken by a narrow-band, transform limited pulse at the center frequency. The position and slope of any ray-pulse is measured with respect to the reference axis on the reference planes. The reference pulse sets the

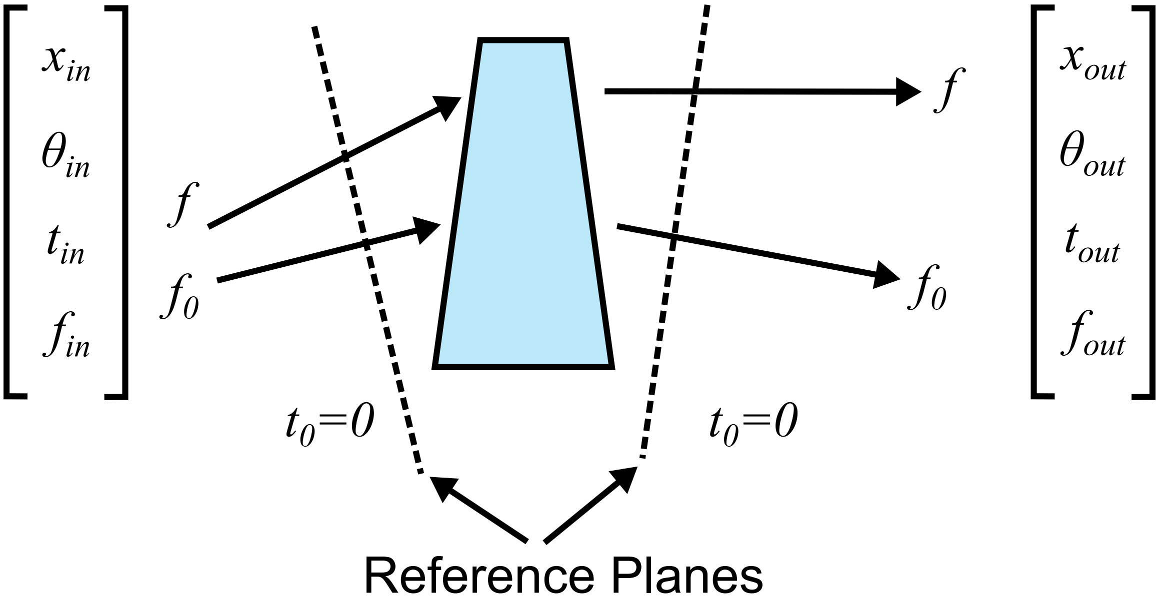

Figure A.1: Geometric construction of the coordinates of a ray-pulse vector in Kostenbauder formulation. The variables x, θ, t, and f are the deviations from the reference pulse values of x_0, θ_0, t_0, and f_0

clock to zero when it passes through the reference planes, and the time coordinate of any other ray-pulse is defined relative to the clock. Therefore, the time coordinate of the ray-pulse under consideration is its delay with respect to the pulse pulse. Similar definition is made for the frequency coordinate which the frequency is measured relative to the center frequency.

A K-matrix relates the input ray-pulse vector to its output by equation A.1.

$$\begin{bmatrix} x_{out} \\ \theta_{out} \\ t_{out} \\ f_{out} \end{bmatrix} = \begin{bmatrix} \frac{\partial x_{out}}{\partial x_{in}} & \frac{\partial x_{out}}{\partial \theta_{in}} & 0 & \frac{\partial x_{out}}{\partial f_{in}} \\ \frac{\partial \theta_{out}}{\partial x_{in}} & \frac{\partial \theta_{out}}{\partial \theta_{in}} & 0 & \frac{\partial \theta_{out}}{\partial f_{in}} \\ \frac{\partial t_{out}}{\partial x_{in}} & \frac{\partial t_{out}}{\partial \theta_{in}} & 1 & \frac{\partial t_{out}}{\partial f_{in}} \\ 0 & 0 & 0 & 1 \end{bmatrix} \begin{bmatrix} x_{in} \\ \theta_{in} \\ t_{in} \\ f_{in} \end{bmatrix} \tag{A.1}$$

It is often expressed in the form like ABCD-matrix as shown in equation A.2:

$$K = \begin{bmatrix} A & B & 0 & E \\ C & D & 0 & F \\ G & H & 1 & I \\ 0 & 0 & 0 & 1 \end{bmatrix} \tag{A.2}$$

where A, B, C, and D are the same as in the ABCD-matrix. E, F, G, H, and I represent the spatial chirp, angular dispersion, pulse-front tilt, time verse angle and group delay dispersion respectively. Here, we show that the pulse will only have pulse-front tilt but not other spatio-temporal distortions at the image plane of the grating. First we define the K-matrix for a reflection grating, $K_{grating}$,

$$K_{grating} = \begin{bmatrix} -\frac{\sin\psi_d}{\sin\psi_i} & 0 & 0 & 0 \\ 0 & -\frac{\sin\psi_i}{\sin\psi_d} & 0 & \frac{c(\cos\psi_d - \cos\psi_i)}{\lambda_0 \sin\psi_d} \\ \frac{\cos\psi_i - \cos\psi_d}{c\sin\psi_i} & 0 & 1 & 0 \\ 0 & 0 & 0 & 1 \end{bmatrix} \tag{A.3}$$

where ψ_i is the angle of incidence of between input pulse from the grating surface (not from the normal of the grating), ψ_d is the angle of the diffracted pulse, λ_0 is the center wavelength, and c is the speed of light. Similarly, the K-matrices for lens with focal length, f, and free space propagation for a distance, L, can be derived:

$$K_{lens} = \begin{bmatrix} 1 & 0 & 0 & 0 \\ -\frac{1}{f} & 1 & 0 & 0 \\ 0 & 0 & 1 & 0 \\ 0 & 0 & 0 & 1 \end{bmatrix} \tag{A.4}$$

and

$$K_L = \begin{bmatrix} 1 & L & 0 & 0 \\ 0 & 1 & 0 & 0 \\ 0 & 0 & 1 & 0 \\ 0 & 0 & 0 & 1 \end{bmatrix} \tag{A.5}$$

The following K-matrix product model a pulse diffracted from a diffraction grating and an imaging lens image the surface of the grating to a image plane:

$$K = K_{L_1} K_{lens} K_{L_2} K_{grating} \tag{A.6}$$

Of course, the imaging condition where $\frac{1}{f} = \frac{1}{L_1} + \frac{1}{L_2}$ has to be satisfied. For simplicity, we choose $L_1 = L_2 = 2f$ which is the 1-to-1 imaging condition. The resultant K-matrix is,

$$K = \begin{bmatrix} \frac{\sin\psi_d}{\sin\psi_i} & 0 & 0 & 0 \\ \frac{\sin\psi_d}{f\sin\psi_i} & \frac{\sin\psi_i}{\sin\psi_d} & 0 & -\frac{c(\cos\psi_d - \cos\psi_i)}{\lambda_0 \sin\psi_d} \\ -\frac{\cos\psi_d - \cos\psi_i}{c\sin\psi_i} & 0 & 1 & 0 \\ 0 & 0 & 0 & 1 \end{bmatrix}. \tag{A.7}$$

Note that term G, which represents the PFT of the optical system, of the resulting K-matrix is proportional to the angular dispersion of the grating (term F of K-matrix A.3). Thus, to increase the PFT in the optical system, one can use a more angular dispersive element. In the case of grating, it means increasing the line density of the grating. One more simplification can be applied by choosing $\psi_d = 90°$. This is almost always the case for PFT generation as the first-order diffraction is chosen to be propagated along the normal of the grating surface to avoid issues from finite depth of field of the imaging system. The final matrix product of equation A.6 is,

$$K = \begin{bmatrix} \frac{1}{\sin\psi_i} & 0 & 0 & 0 \\ \frac{1}{f\sin\psi_i} & \sin\psi_i & 0 & \frac{c\cos\psi_i}{\lambda_0} \\ \frac{\cos\psi_i}{c\sin\psi_i} & 0 & 1 & 0 \\ 0 & 0 & 0 & 1 \end{bmatrix}. \tag{A.8}$$

The resultant K-matrix shows that E, H and I are identically zero which means the pulse has no spatial chirp, time verse angle, and group delay dispersion. The non-zero angular dispersion implies that different wavelength components in the pulse are going into different directions. This is not surprising because the removal of spatio-temporal distortions only happened at the image plane. Once the pulse leaves the image plane, different the wavelengths will propagate along different directions and all the distortions will appear again in the pulse. At the image plane, it is proved by K-matrix that only pulse-front tilt exists.

REFERENCES

[1] T. Suzuki, "Femtosecond time-resolved photoelectron imaging," *Annual Review of Physical Chemistry* **57**, 555 (2006).

[2] S. Y. Liu, Y. Ogi, T. Fuji, K. Nishizawa, T. Horio, T. Mizuno, H. Kohguchi, M. Nagasono, T. Togashi, K. Tono, M. Yabashi, Y. Senba, H. Ohashi, H. Kimura, T. Ishikawa, and T. Suzuki, "Time-resolved photoelectron imaging using a femtosecond UV laser and a VUV free-electron laser," *Physical Review A* **81**, 031403 (2010).

[3] A. H. Zewail, "Femtochemistry: Atomic-Scale Dynamics of the Chemical Bond Using Ultrafast Lasers (Nobel Lecture)," *Angewandte Chemie International Edition* **39**, 2586 (2000).

[4] B. N. Chichkov, C. Momma, S. Nolte, F. Alvensleben, and A. Tunnermann, "Femtosecond, picosecond and nanosecond laser ablation of solids," *Applied Physics A* **63**, 109 (1996).

[5] J. Cheng, C.-s. Liu, S. Shang, D. Liu, W. Perrie, G. Dearden, and K. Watkins, "A review of ultrafast laser materials micromachining," *Optics and Laser Technology* **46**, 88 (2013).

[6] G. D. Valle, R. Osellame, and P. Laporta, "Micromachining of photonic devices by femtosecond laser pulses," *Journal of Optics A: Pure and Applied Optics* **11**, 013001 (2009).

[7] N. G. Horton, K. Wang, D. Kobat, C. G. Clark, F. W. Wise, C. B. Schaffer, and C. Xu, "In vivo three-photon microscopy of subcortical structures within an intact mouse brain," *Nat Photon* **7**, 205 (2013).

[8] W. Denk, J. Strickler, and W. Webb, "Two-photon laser scanning fluorescence microscopy," *Science* **248**, 73 (1990).

[9] R. Kawakami, K. Sawada, A. Sato, T. Hibi, Y. Kozawa, S. Sato, H. Yokoyama, and T. Nemoto, "Visualizing hippocampal neurons with in vivo two-photon microscopy using a 1030 nm picosecond pulse laser," *Scientific reports* **3**, 1014 (2013).

[10] R. R. Krueger, T. Juhasz, A. Gualano, and V. Marchi, "The picosecond laser for nonmechanical laser in situ keratomileusis," *Journal of refractive surgery (Thorofare, N.J. : 1995)* **14**, 467 (1998).

[11] R. R. Alfano and S. L. Shapiro, "Emission in the Region 4000 to 7000 A Via Four-Photon Coupling in Glass," *Physical Review Letters* **24**, 584 (1970).

[12] A. Brodeur and S. L. Chin, "Ultrafast white-light continuum generation and self-focusing in transparent condensed media," *J. Opt. Soc. Am. B* **16**, 637 (1999).

[13] J. M. Dudley, G. Genty, and S. Coen, "Supercontinuum generation in photonic crystal fiber," *Reviews of Modern Physics* **78**, 1135 (2006).

[14] J. Bethge, A. Husakou, F. Mitschke, F. Noack, U. Griebner, G. Steinmeyer, and J. Herrmann, "Two-octave supercontinuum generation in a water-filled photonic crystal fiber," *Optics Express* **18**, 6230 (2010).

[15] O. M. Efimov, K. Gabel, S. V. Garnov, L. B. Glebov, S. Grantham, M. Richardson, and M. J. Soileau, "Color-center generation in silicate glasses exposed to infrared femtosecond pulses," *J. Opt. Soc. Am. B* **15**, 193 (1998).

[16] V. Francois, F. A. Ilkov, and S. L. Chin, "Supercontinuum generation in CO 2 gas accompanied by optical breakdown," *Journal of Physics B: Atomic, Molecular and Optical Physics* **25**, 2709 (1992).

[17] E. Goulielmakis, M. Schultze, M. Hofstetter, V. S. Yakovlev, J. Gagnon, M. Uiberacker, A. L. Aquila, E. M. Gullikson, D. T. Attwood, R. Kienberger, F. Krausz, and U. Kleineberg, "Single-Cycle Nonlinear Optics," *Science* **320**, 1614 (2008).

[18] K. Zhao, Q. Zhang, M. Chini, Y. Wu, X. Wang, and Z. Chang, "Tailoring a 67 attosecond pulse through advantageous phase-mismatch," *Opt. Lett.* **37**, 3891 (2012).

[19] F. J. McClung and R. W. Hellwarth, "Giant Optical Pulsations from Ruby," *Journal of Applied Physics* **33**, 828 (1962).

[20] J. J. Zayhowski, "Q-switched operation of microchip lasers," *Optics Letters* **16**, 575 (1991).

[21] N. Sarukura, Y. Ishida, H. Nakano, and Y. Yamamoto, "cw passive mode locking of a Ti:sapphire laser," *Applied Physics Letters* **56**, 814 (1990).

[22] R. Ell, U. Morgner, F. X. KAArtner, J. G. Fujimoto, E. P. Ippen, V. Scheuer, G. Angelow, T. Tschudi, M. J. Lederer, A. Boiko, and B. Luther-Davies, "Generation of 5-fs pulses and octave-spanning spectra directly from a Ti:sapphire laser," *Optics Letters* **26**, 373 (2001).

[23] J. Herrmann, "Theory of Kerr-lens mode locking: role of self-focusing and radially varying gain," *Journal of the Optical Society of America B* **11**, 498 (1994).

[24] J. C. Diels, E. Van Stryland, and G. Benedict, "Generation and measurement of 200 femtosecond optical pulses," *Optics Communications* **25**, 93 (1978).

[25] F. Salin, P. Georges, G. Roger, and A. Brun, "Single-shot measurement of a 52-fs pulse," *Applied Optics* **26**, 4528 (1987).

[26] M. Pessot, D. J. Harter, J. Squier, and G. Mourou, "Chirped-pulse amplification of 100-fsec pulses," *Optics Letters* **14**, 797 (1989).

[27] C. Jung-Ho and A. M. Weiner, "Ambiguity of ultrashort pulse shapes retrieved from the intensity autocorrelation and the power spectrum," *Selected Topics in Quantum Electronics, IEEE Journal of* **7**, 656 (2001).

[28] R. Trebino, *Frequency-Resolved Optical Gating: The Measurement of Ultrashort Laser Pulses* (Springer, New York, USA, 2002).

[29] P. O'Shea, M. Kimmel, X. Gu, and R. Trebino, "Highly simplified device for ultrashort-pulse measurement," *Optics Letters* **26**, 932 (2001).

[30] P. O'Shea, S. Akturk, M. Kimmel, and R. Trebino, "Practical issues in ultrashort-pulse measurements with GRENOUILLE," *Applied Physics B* **79**, 683 (2004).

[31] L. Xu, E. Zeek, and R. Trebino, "Simulations of frequency-resolved optical gating for measuring very complex pulses," *Journal of the Optical Society of America B* **25**, A70 (2008).

[32] J.-y. Zhang, A. Shreenath, M. Kimmel, E. Zeek, R. Trebino, and S. Link, "Measurement of the intensity and phase of attojoule femtosecond light pulses using Optical-Parametric-Amplification Cross-Correlation Frequency-Resolved Optical Gating," *Optics Express* **11**, 601 (2003).

[33] T. Fuji and T. Suzuki, "Generation of sub-two-cycle mid-infrared pulses by four-wave mixing through filamentation in air," *Optics Letters* **32**, 3330 (2007).

[34] J. A. Gruetzmacher and N. F. Scherer, "Few-cycle mid-infrared pulse generation, characterization, and coherent propagation in optically dense media," *Review of Scientific Instruments* **73**, 2227 (2002).

[35] J. Liu, Y. Feng, H. Li, P. Lu, H. Pan, J. Wu, and H. Zeng, "Supercontinuum pulse measurement by molecular alignment based cross-correlation frequency resolved optical gating," *Opt. Express* **19**, 40 (2011).

[36] E. P. Power, A. M. March, F. Catoire, E. Sistrunk, K. Krushelnick, P. Agostini, and L. F. DiMauro, "XFROG phase measurement of threshold harmonics in a Keldysh-scaled system," *Nat Photon* **4**, 352 (2010).

[37] T. Sekikawa, T. Kanai, and S. Watanabe, "Frequency-Resolved Optical Gating of Femtosecond Pulses in the Extreme Ultraviolet," *Physical Review Letters* **91**, 103902 (2003).

[38] J. Dudley, X. Gu, L. Xu, M. Kimmel, E. Zeek, P. O'Shea, R. Trebino, S. Coen, and R. Windeler, "Cross-correlation frequency resolved optical gating analysis of broadband continuum generation in photonic crystal fiber: simulations and experiments," *Opt. Express* **10**, 1215 (2002).

[39] Q. Cao, X. Gu, E. Zeek, M. Kimmel, R. Trebino, J. Dudley, and R. S. Windeler, "Measurement of the intensity and phase of supercontinuum from an 8-mm-long microstructure fiber," *Applied Physics B* **77**, 239 (2003).

[40] C. Iaconis and I. A. Walmsley, "Spectral phase interferometry for direct electric-field reconstruction of ultrashort optical pulses," *Optics Letters* **23**, 792 (1998).

[41] R. A. Fisher and J. J. A. Fleck, "ON THE PHASE CHARACTERISTICS AND COMPRESSION OF PICOSECOND PULSES," *Applied Physics Letters* **15**, 287 (1969).

[42] E. W. Van Stryland, "The effect of pulse to pulse variation on ultrashort pulsewidth measurements," *Optics Communications* **31**, 93 (1979).

[43] J. Ratner, G. Steinmeyer, T. C. Wong, R. Bartels, and R. Trebino, "Coherent artifact in modern pulse measurements," *Opt. Lett.* **37**, 2874 (2012).

[44] F. Quere, J. Itatani, G. L. Yudin, and P. B. Corkum, "Attosecond Spectral Shearing Interferometry," *Physical Review Letters* **90**, 073902 (2003).

[45] M. Takeda, H. Ina, and S. Kobayashi, "Fourier-transform method of fringe-pattern analysis for computer-based topography and interferometry," *Journal of the Optical Society of America* **72**, 156 (1982).

[46] B. Kohler, V. V. Yakovlev, J. Che, J. L. Krause, M. Messina, K. R. Wilson, N. Schwentner, R. M. Whitnell, and Y. Yan, "Quantum Control of Wave Packet Evolution with Tailored Femtosecond Pulses," *Physical Review Letters* **74**, 3360 (1995).

[47] A. H. Zewail, "Femtochemistry: Atomic-Scale Dynamics of the Chemical Bond," *The Journal of Physical Chemistry A* **104**, 5660 (2000).

[48] M. Fushitani, "Applications of pump-probe spectroscopy," *Annual Reports Section "C" (Physical Chemistry)* **104**, 272 (2008).

[49] D. Polli, D. Brida, S. Mukamel, G. Lanzani, and G. Cerullo, "Effective temporal resolution in pump-probe spectroscopy with strongly chirped pulses," *Physical Review A* **82**, 053809 (2010).

[50] J. K. Ranka, R. S. Windeler, and A. J. Stentz, "Visible continuum generation in air-silica microstructure optical fibers with anomalous dispersion at 800 nm," *Opt. Lett.* **25**, 25 (2000).

[51] K. W. DeLong, R. Trebino, and W. E. White, “Simultaneous recovery of two ultrashort laser pulses from a single spectrogram,” *Journal of the Optical Society of America B* **12**, 2463 (1995).

[52] D. J. Kane, G. Rodriguez, A. J. Taylor, and T. S. Clement, “Simultaneous measurement of two ultrashort laser pulses from a single spectrogram in a single shot,” *Journal of the Optical Society of America B* **14**, 935 (1997).

[53] J. J. Field, C. G. Durfee, and J. A. Squier, “Blind frequency-resolved optical-gating pulse characterization for quantitative differential multiphoton microscopy,” *Optics Letters* **35**, 3369 (2010).

[54] A. Hause, H. Hartwig, B. Seifert, H. Stolz, M. Bohm, and F. Mitschke, “Phase structure of soliton molecules,” *Physical Review A* **75**, 063836 (2007).

[55] S. Birger and S. Heinrich, “A method for unique phase retrieval of ultrafast optical fields,” *Measurement Science and Technology* **20**, 015303 (2009).

[56] B. Seifert, H. Stolz, and M. Tasche, “Nontrivial ambiguities for blind frequency-resolved optical gating and the problem of uniqueness,” *Journal of the Optical Society of America B* **21**, 1089 (2004).

[57] T. C. Wong, J. Ratner, V. Chauhan, J. Cohen, P. M. Vaughan, L. Xu, A. Consoli, and R. Trebino, “Simultaneously measuring two ultrashort laser pulses on a single-shot using double-blind frequency-resolved optical gating,” *J. Opt. Soc. Am. B* **29**, 1237 (2012).

[58] T. C. Wong, J. Ratner, and R. Trebino, “Simultaneous measurement of two different-color ultrashort pulses on a single shot,” *J. Opt. Soc. Am. B* **29**, 1889 (2012).

[59] T. Wong and R. Trebino, “Recent Developments in Experimental Techniques for Measuring Two Pulses Simultaneously,” *Applied Sciences* **3**, 299 (2013).

[60] Y. Mairesse and F. Quere, “Frequency-resolved optical gating for complete reconstruction of attosecond bursts,” *Physical Review A* **71**, 011401 (2005).

[61] K. T. Kim, D. H. Ko, J. Park, V. Tosa, and C. H. Nam, “Complete temporal reconstruction of attosecond high-harmonic pulse trains,” *New Journal of Physics* **12**, 083019 (2010).

[62] D. Lee, Z. Wang, X. Gu, and R. Trebino, “Effect-and removal-of an ultrashort pulse’s spatial profile on the single-shot measurement of its temporal profile,” *Journal of the Optical Society of America B* **25**, A93 (2008).

[63] G. Huettmann, B. Radt, J. Serbin, and R. Birngruber, “Inactivation of proteins by irradiation of gold nanoparticles with nano- and picosecond laser pulses,” *SPIE 5142* , 88 (2003).

[64] R. Kawakami, K. Sawada, A. Sato, T. Hibi, Y. Kozawa, S. Sato, H. Yokoyama, and T. Nemoto, "Visualizing hippocampal neurons with in vivo two-photon microscopy using a 1030 nm picosecond pulse laser," *Scientific reports* **3**, 1014 (2013).

[65] P. L. Liu, R. Yen, N. Bloembergen, and R. T. Hodgson, "Picosecond laser-induced melting and resolidification morphology on Si," *Applied Physics Letters* **34**, 864 (1979).

[66] B. Zysset, J. G. Fujimoto, C. A. Puliafito, R. Birngruber, and T. F. Deutsch, "Picosecond optical breakdown: Tissue effects and reduction of collateral damage," *Lasers in Surgery and Medicine* **9**, 193 (1989).

[67] J. Noack and A. Vogel, "Laser-induced plasma formation in water at nanosecond to femtosecond time scales: calculation of thresholds, absorption coefficients, and energy density," *Quantum Electronics, IEEE Journal of* **35**, 1156 (1999).

[68] B. Zysset, J. G. Fujimoto, and T. F. Deutsch, "Time-resolved measurements of picosecond optical breakdown," *Applied Physics B* **48**, 139 (1989).

[69] B. C. Stuart, M. D. Feit, A. M. Rubenchik, B. W. Shore, and M. D. Perry, "Laser-Induced Damage in Dielectrics with Nanosecond to Subpicosecond Pulses," *Physical Review Letters* **74**, 2248 (1995).

[70] B.-M. Kim, A. M. Komashko, A. M. Rubenchik, M. D. Feit, S. Reidt, L. B. D. Silva, and J. Eichler, "Interferometric analysis of ultrashort pulse laser-induced pressure waves in water," *Journal of Applied Physics* **94**, 709 (2003).

[71] R. Intartaglia, G. Das, K. Bagga, A. Gopalakrishnan, A. Genovese, M. Povia, E. Di Fabrizio, R. Cingolani, A. Diaspro, and F. Brandi, "Laser synthesis of ligand-free bimetallic nanoparticles for plasmonic applications," *Physical chemistry chemical physics : PCCP* **15**, 3075 (2013).

[72] T. Jiang, J. Koch, C. Unger, E. Fadeeva, A. Koroleva, Q. Zhao, and B. Chichkov, "Ultrashort picosecond laser processing of micro-molds for fabricating plastic parts with superhydrophobic surfaces," *Applied Physics A* **108**, 863 (2012).

[73] M. Malinauskas, P. Danilevicius, and S. Juodkazis, "Three-dimensional micro-/nano-structuring via direct write polymerization with picosecond laser pulses," *Opt. Express* **19**, 5602 (2011).

[74] R. Moser, M. Kunzer, C. Gosler, R. Schmidt, K. Kohler, W. Pletschen, U. T. Schwarz, and J. Wagner, "Laser processing of GaN-based LEDs with ultraviolet picosecond laser pulses," *Proc. SPIE 8433, Laser Sources and Applications* , 84330Q (2012).

[75] Y. Pu, W. Wang, R. B. Dorshow, B. B. Das, and R. R. Alfano, "Review of ultrafast fluorescence polarization spectroscopy [Invited]," *Appl. Opt.* **52**, 917 (2013).

[76] X.-H. Hu and T. Juhasz, "Study of corneal ablation with picosecond laser pulses at 211 nm and 263 nm," *Lasers in Surgery and Medicine* **18**, 373 (1996).

[77] D. Stern, R. W. Schoenlein, C. A. Puliafito, E. T. Dobi, R. Birngruber, and J. G. Fujimoto, "Corneal ablation by nanosecond, picosecond, and femtosecond lasers at 532 and 625 nm," *Archives of ophthalmology* **107**, 587 (1989).

[78] J. M. Krauss and C. A. Puliafito, "Lasers in ophthalmology," *Lasers in Surgery and Medicine* **17**, 102 (1995).

[79] A. Vogel, S. Busch, K. Jungnickel, and R. Birngruber, "Mechanisms of intraocular photodisruption with picosecond and nanosecond laser pulses," *Lasers in Surgery and Medicine* **15**, 32 (1994).

[80] E. F. Bernstein, "Laser Tattoo Removal," *Seminars in Plastic Surgery* **21**, 175 (2007).

[81] G. Pfirrmann, S. Karsai, S. Roos, S. Hammes, and C. Raulin, "Tattoo removal V state of the art," *JDDG: Journal der Deutschen Dermatologischen Gesellschaft* **5**, 889 (2007).

[82] N. Saedi, A. Metelitsa, K. Petrell, K. A. Arndt, and J. S. Dover, "Treatment of tattoos with a picosecond alexandrite laser: A prospective trial," *Archives of Dermatology* **148**, 1360 (2012).

[83] N. I. Tankovich, A. M. Hunter, and K. Y. Tang, "Hair removal device and method," *US Patent 6,267,771* (2001).

[84] M. S. Bello-Silva, M. Wehner, C. P. Eduardo, F. Lampert, R. Poprawe, M. Hermans, and M. Esteves-Oliveira, "Precise ablation of dental hard tissues with ultra-short pulsed lasers. Preliminary exploratory investigation on adequate laser parameters," *Lasers in Medical Science* **28**, 171 (2013).

[85] M. Niemz, "Cavity Preparation with the Nd:YLF Picosecond Laser," *Journal of Dental Research* **74**, 1194 (1995).

[86] A. A. Serafetinides, M. G. Khabbaz, M. I. Makropoulou, and A. K. Kar, "Picosecond Laser Ablation of Dentine in Endodontics," *Lasers in Medical Science* **14**, 168 (1999).

[87] M. B. Strigin and A. N. Chudinov, "Cutting of glass by picosecond laser radiation," *Optics Communications* **106**, 223 (1994).

[88] D. Shin, J. Lee, H. Sohn, J. Noh, and B. Paik, "A FPCB cutting process using a pico-second laser," *JLMN* **5**, 48 (2010).

[89] B. N. Chichkov, C. Momma, S. Nolte, F. Alvensleben, and A. Tunnermann, “Femtosecond, picosecond and nanosecond laser ablation of solids,” *Applied Physics A* **63**, 109 (1996).

[90] N. N. Nedialkov, S. E. Imamova, and P. A. Atanasov, “Ablation of metals by ultrashort laser pulses,” *Journal of Physics D: Applied Physics* **37**, 638 (2004).

[91] J. Cheng, C.-s. Liu, S. Shang, D. Liu, W. Perrie, G. Dearden, and K. Watkins, “A review of ultrafast laser materials micromachining,” *Optics and Laser Technology* **46**, 88 (2013).

[92] J. A. Armstrong, “Measurement of picosecond laser pulse widths,” *Applied Physics Letters* **10**, 16 (1967).

[93] H. P. Weber and H. G. Danielmeyer, “Multimode Effects in Intensity Correlation Measurements,” *Physical Review A* **2**, 2074 (1970).

[94] E. Ippen, C. Shank, and A. Dienes, “Passive mode locking of the cw dye laser,” *Applied Physics Letters* **21**, 348 (1972).

[95] C. Lee and S. Jayaraman, “Measurement of ultrashort optical pulses by two-photon photoconductivity techniques,” *Opto-electronics* **6**, 115 (1974).

[96] Y. Takagi, T. Kobayashi, K. Yoshihara, and S. Imamura, “Multiple- and single-shot autocorrelator based on two-photon conductivity in semiconductors,” *Opt. Lett.* **17**, 658 (1992).

[97] J. A. Giordmaine, P. M. Rentzepis, S. L. Shapiro, and K. W. Wecht, “Two-photon excitation of fluorescence by picosecnd light pulses,” *Applied Physics Letters* **11**, 216 (1967).

[98] P. Sperber and A. Penzkofer, “Pulse-shape determination of intracavity compressed picosecond pulses by two-photon fluorescence analysis,” *Optical and Quantum Electronics* **18**, 145 (1986).

[99] H. P. Weber and R. Dandliker, “Method for measurement the shape asymmetry of picosecond light pulses,” *Physics Letters A* **28**, 77 (1968).

[100] S. Luan, M. H. R. Hutchinson, R. A. Smith, and F. Zhou, “High dynamic range third-order correlation measurement of picosecond laser pulse shapes,” *Measurement Science and Technology* **4**, 1426 (1993).

[101] P. Yeh, “Autocorrelation of ultrashort optical pulses using polarization interferometry,” *Opt. Lett.* **8**, 330 (1983).

[102] T. Mindl, P. Hefferle, S. Schneider, and F. Dorr, “Characterisation of a train of subpicosecond laser pulses by fringe resolved autocorrelation measurements,” *Applied Physics B* **31**, 201 (1983).

[103] M. Rhodes, G. Steinmeyer, J. Ratner, and R. Trebino, “Pulse-shape instabilities and their measurement,” *Laser and Photonics Reviews* , doi: 10.1002/lpor.201200102 (2013).

[104] R. Wyatt and E. E. Marinero, “Versatile single-shot background-free pulse duration measurement technique, for pulses of subnanosecond to picosecond duration,” *Applied physics* **25**, 297 (1981).

[105] P. Bowlan and R. Trebino, “Complete single-shot measurement of arbitrary nanosecond laser pulses in time,” *Opt. Expr.* **19**, 1367 (2011).

[106] T. C. Wong and R. Trebino, “Single-frame measurement of complex laser pulses tens of picoseconds long using pulse-front tilt in cross-correlation frequency-resolved optical gating,” *Journal of the Optical Society of America B* **30**, 2781 (2013).

[107] X. Gu, L. Xu, M. Kimmel, E. Zeek, P. O’Shea, A. P. Shreenath, R. Trebino, and R. S. Windeler, “Frequency-resolved optical gating and single-shot spectral measurements reveal fine structure in microstructure-fiber continuum,” *Opt. Lett.* **27**, 1174 (2002).

[108] R. R. Alfano, *The Supercontinuum Laser Source: Fundamentals with Updated References* (Springer, 2006).

[109] D. Wildanger, E. Rittweger, L. Kastrup, and S. W. Hell, “STED microscopy with a supercontinuum laser source,” *Opt. Express* **16**, 9614 (2008).

[110] G. Humbert, W. Wadsworth, S. Leon-Saval, J. Knight, T. Birks, P. St. J. Russell, M. Lederer, D. Kopf, K. Wiesauer, E. Breuer, and D. Stifter, “Supercontinuum generation system for optical coherence tomography based on tapered photonic crystal fibre,” *Opt. Express* **14**, 1596 (2006).

[111] T. Udem, R. Holzwarth, and T. W. Hansch, “Optical frequency metrology,” *Nature* **416**, 233 (2002).

[112] D. J. Jones, S. A. Diddams, J. K. Ranka, A. Stentz, R. S. Windeler, J. L. Hall, and S. T. Cundiff, “Carrier-Envelope Phase Control of Femtosecond Mode-Locked Lasers and Direct Optical Frequency Synthesis,” *Science* **288**, 635 (2000).

[113] H. Kubota, K. R. Tamura, and M. Nakazawa, “Analyses of coherence-maintained ultrashort optical pulse trains and supercontinuum generation in the presence of soliton-amplified spontaneous-emission interaction,” *J. Opt. Soc. Am. B* **16**, 2223 (1999).

[114] A. L. Gaeta, “Nonlinear propagation and continuum generation in microstructured optical fibers,” *Opt. Lett.* **27**, 924 (2002).

[115] U. Moller, S. T. Sorensen, C. Jakobsen, J. Johansen, P. M. Moselund, C. L. Thomsen, and O. Bang, “Power dependence of supercontinuum noise in uniform and tapered PCFs,” *Opt. Express* **20**, 2851 (2012).

[116] S. T. Sorensen, C. Larsen, U. Moller, P. M. Moselund, C. L. Thomsen, and O. Bang, “Influence of pump power and modulation instability gain spectrum on seeded supercontinuum and rogue wave generation,” *J. Opt. Soc. Am. B* **29**, 2875 (2012).

[117] S. T. Sorensen, C. Larsen, U. Moller, P. M. Moselund, C. L. Thomsen, and O. Bang, “The role of phase coherence in seeded supercontinuum generation,” *Opt. Express* **20**, 22886 (2012).

[118] B. Wetzel, A. Stefani, L. Larger, P. A. Lacourt, J. M. Merolla, T. Sylvestre, A. Kudlinski, A. Mussot, G. Genty, F. Dias, and J. M. Dudley, “Real-time full bandwidth measurement of spectral noise in supercontinuum generation,” *Sci. Rep.* **2** (2012).

[119] T. Godin, B. Wetzel, T. Sylvestre, L. Larger, A. Kudlinski, A. Mussot, A. Ben Salem, M. Zghal, G. Genty, F. Dias, and J. M. Dudley, “Real time noise and wavelength correlations in octave-spanning supercontinuum generation,” *Optics Express* **21**, 18452 (2013).

[120] A. Bozolan, C. J. de Matos, C. M. B. Cordeiro, E. M. dos Santos, and J. Travers, “Supercontinuum generation in a water-core photonic crystal fiber,” *Optics Express* **16**, 9671 (2008).

[121] D. R. Solli, C. Ropers, and B. Jalali, “Measuring single-shot modulation instability and supercontinuum spectra at megahertz rates,” *Nonlinearity* **26**, R85 (2013).

[122] X. Gu, M. Kimmel, A. Shreenath, R. Trebino, J. Dudley, S. Coen, and R. Windeler, “Experimental studies of the coherence of microstructure-fiber supercontinuum,” *Opt. Express* **11**, 2697 (2003).

[123] D. Lee, P. Gabolde, and R. Trebino, “Toward single-shot measurement of a broadband ultrafast continuum,” *J. Opt. Soc. Am. B* **25**, A34 (2008).

[124] B. Tsermaa, B.-K. Yang, M.-W. Kim, and J.-S. Kim, “Characterization of Supercontinuum and Ultraviolet Pulses by Using XFROG,” *J. Opt. Soc. Korea* **13**, 158 (2009).

[125] J. Teipel, K. Franke, D. Turke, F. Warken, D. Meiser, M. Leuschner, and H. Giessen, “Characteristics of supercontinuum generationin tapered fibers using femtosecond laser pulses,” *Applied Physics B* **77**, 245 (2003).

[126] J.-Y. Zhang, C.-K. Lee, J. Y. Huang, and C.-Y. Pan, “Sub-femto-joule sensitive single-shot OPA-XFROG and its application in study of white-light supercontinuum generation,” *Opt. Expr.* **12**, 574 (2004).

[127] D. R. Solli, C. Ropers, P. Koonath, and B. Jalali, "Optical rogue waves," *Nature* **450**, 1054 (2007).

[128] J. M. Dudley, G. Genty, and B. J. Eggleton, "Harnessing and control of optical rogue waves in supercontinuum generation," *Opt. Express* **16**, 3644 (2008).

[129] N. Akhmediev, A. Ankiewicz, J. M. Soto-Crespo, and J. M. Dudley, "Rogue wave early warning through spectral measurements?," *Physics Letters A* **375**, 541 (2011).

[130] D. R. Solli, C. Ropers, and B. Jalali, "Active Control of Rogue Waves for Stimulated Supercontinuum Generation," *Physical Review Letters* **101**, 233902 (2008).

[131] A. R. Osborne, M. Onorato, and M. Serio, "The nonlinear dynamics of rogue waves and holes in deep-water gravity wave trains," *Physics Letters A* **275**, 386 (2000).

[132] M. J. Steel, T. P. White, C. Martijn de Sterke, R. C. McPhedran, and L. C. Botten, "Symmetry and degeneracy in microstructured optical fibers," *Optics Letters* **26**, 488 (2001).

[133] T. Ritari, T. Niemi, H. Ludvigsen, M. Wegmuller, N. Gisin, J. R. Folkenberg, and A. Petterson, "Polarization-mode dispersion of large mode-area photonic crystal fibers," *Optics Communications* **226**, 233 (2003).